Tiago Caeatano Madeira

Model Predicitive Control of a Doubly-fed Induction Generator, Connected to a Dc-grid, for Distributed Generation

February 2018

· U C ·

Universidade de Coimbra

University of Coimbra
Faculty of Sciences and Technology
Department of Electrical and Computer Engineering

Model Predictive Control of a Doubly-fed Induction Generator, Connected to a Dc-grid, for Distributed Generation

Tiago Caetano Madeira

A dissertation presented for the degree of
Master of Science in Electrical and Computer Engineering

Jury:
Prof. Doutor Rui Alexandre de Matos Araújo (President)
Prof. Doutor Sérgio Manuel Ângelo da Cruz (Supervisor)
Prof. Doutor Fernando José Teixeira Estêvão Ferreira (Vowel)

February 2018

Acknowledgements

First of all, i would like to thank my supervisor Dr. Sérgio Manuel Ângelo da Cruz for his invaluable guidance, patience and support given throughout this thesis. I would like to highlight that the development of this work could not be possible without his knowledge and expertise.

I also want to thank my laboratory colleagues, José Mendes, David Duarte, Hazem Hadla and Pedro Gonçalves for all the support, companionship and shared good moments that helped me to carry on during the course of this journey. A very special thanks is given to Pedro for all the hours he spent helping and for all the headaches i must have given him.

My appreciation goes as well, to my friends, real titans in life, for their support, friendship, listening skills, and proven fighting spirit throughout the years.

Lastly, i am deeply grateful to my parents for the love, patience and efforts made while raising me.

Abstract

This work presents a predictive control strategy applied to a doubly-fed induction generator (DFIG) connected to a dc microgrid, suitable for distributed generation purposes and microgrid environment. The topology of connecting the DFIG to the dc grid consists in the replacement of one voltage source inverter by a diode rectifier. However, the inclusion of the diode rectifier gives rise to a large torque ripple, characterized by a component oscillating at six times the stator frequency. This harmonic component has negative effects on the mechanical components of the drive system and as such, efforts are needed to eliminate those torque oscillations. Classical control strategies, based on field orientation try to address this issue by the inclusion of resonant controllers, or by decomposing and suppressing this harmonic component in multiple reference frames. However, those methods have inherent disadvantages, such as: great tuning effort, inferior dynamic response and difficulty to include restrictions in the system. Furthermore, the existence of multiple control loops dictates that separate bandwidth for them must be ensured, as the stability of the system is closely related to the bandwidth of the inner loop. The use of model predictive control (MPC) in the proposed control system system avoids all the difficulties associated with vector control and is able to practically fully eliminate the low-frequency torque oscillations. Attending that predictive control strategies are based in discrete models, their performance is heavily dependent on the model parameters accuracy and of a correct parameter estimation. On the other hand, the complexity of the discrete model must also be minimized, to make the algorithm feasible for practical use. As such, a comparison is also provided on the steady-state and dynamic performance of the system, when the forward Euler and Taylor series expansion discretization methods are used.

Keywords: dc microgrid, doubly-fed induction generator, model predictive control, discretization methods.

Resumo

Esta dissertação apresenta uma estratégia de controlo preditivo aplicada a um gerador de indução duplamente alimentado (DFIG) ligado a uma rede dc, adequada para geração distribuída e em ambiente de micro-rede. A topologia de ligação da DFIG à rede dc é obtida através da substituição de um dos inversores de fonte de tensão por um retificador a díodos. Contudo a inclusão do retificador a díodos origina uma ondulação no binário, caracterizada por uma componente que oscila a uma frequência seis vezes superior à frequência do estator. Esta componente harmónica tem efeitos negativos sobre os componentes mecânicos do sistema, e como tal, são necessários esforços para eliminar essas oscilações no binário. As estratégias de controlo clássicas, baseadas na orientação de campo, abordam esta questão através da inclusão de controladores ressonantes, ou através da decomposição e supressão desta componente harmónica em referenciais múltiplos. No entanto, estes métodos apresentam desvantagens inerentes, tais como: grande esforço de sintonização, resposta dinâmica inferior e dificuldade de incluir restrições no sistema. Além disso, a existência de múltiplas malhas de controlo dita o uso de uma separação elevada nas larguras de banda do sistema de controlo e que a estabilidade do sistema está fortemente dependente da largura de banda da malha interna. A utilização de controlo preditivo baseado em modelos (MPC) no sistema de controlo proposto, consegue evitar todas as dificuldades associadas ao controlo vetorial, e é capaz de praticamente eliminar as oscilações de baixa frequência presentes no binário. Atendendo que as estratégias de controlo preditivo são baseadas em modelos discretos, o seu desempenho é fortemente dependente da precisão dos parâmetros do modelo, assim como da correcta estimação destes parâmetros. Por outro lado, a complexidade do modelo discreto deve também ser minimizada, por forma a tornar o algoritmo viável para uso prático. Como tal, também é fornecida uma comparação do desempenho do sistema, quando as diferentes técnicas de discretização são usadas, designadamente o método de Euler e a expansão em série de Taylor.

Palavras-Chave: rede dc, gerador de indução duplamente alimentado, controlo preditivo baseado em modelos, métodos de discretização

Contents

List of Figures **iii**

List of Tables **x**

Terminology **xi**

1 Introduction **1**

1.1 Framework 1

1.2 Motivation and Objectives 3

2 DFIG-dc systems **5**

2.1 Introduction 5

2.2 State of the Art of Control Strategies for DFIG-dc Systems 8

2.2.1 Vector Control Strategies 8

2.2.2 Model Predictive Control 12

3 Predictive Torque and Rotor Flux Control **17**

3.1 Mathematical Model 17

3.2 Discretization Methods 19

3.2.1 Forward Euler 20

3.2.2 Taylor Series Expansion 22

3.3 Cost Function Design 23

3.4 Rotor Flux Level Optimization . . . 23
3.5 Overcurrent protection . . . 26

4 System Simulation **29**
4.1 Simulation Model . . . 29
4.2 Obtained Results . . . 30
4.2.1 Steady-State Operation . . . 30
4.2.2 Dynamic Operation . . . 35
4.2.2.1 Torque Ramp Response . . . 36
4.2.2.2 Torque Step Response . . . 36
4.2.2.3 Speed Ramp Response . . . 37
4.2.3 Sensitivity Analysis . . . 38

5 Experimental Validation **41**
5.1 Test Rig . . . 41
5.2 Experimental Results . . . 43
5.2.1 Steady-State Operation . . . 43
5.2.2 Dynamic Operation . . . 50
5.2.2.1 Torque Ramp Response . . . 51
5.2.2.2 Torque Step Response . . . 52
5.2.2.3 Speed Ramp Response . . . 53
5.2.3 Sensitivity Analysis . . . 54

6 Conclusions and Future Work **59**

Bibliography **61**

Appendix A Simulation Model **67**

Appendix B System Parameters **69**

Appendix C Experimental Setup **71**

A System Components 71

B dSPACE Model 73

List of Figures

2.1 DFIG-dc system with diode rectifier connected to the stator and voltage source inverter connected to the rotor [14] 6

2.2 Stand-alone DFIG-dc system with diode rectifier connected to the stator and voltage source inverter connected to the rotor. 8

2.3 Steady-State model of the DFIG-DC system: (a) phasor diagram for positive slip operation [29]; (b) equivalent Γ circuit of the DFIG in a synchronous reference frame [27]. 8

2.4 General field oriented control scheme [28] 9

2.5 PLL for stator frequency estimation [32] 10

2.6 Current loops with PI+Ressonant controller [20] 12

2.7 Operation of FCS-MPC with delay compensation. 15

2.8 Sensorless method for slip angle position estimation [14]. 16

3.1 Equivalent circuit of a DFIG in a rotor reference frame. 17

3.2 RSC model. 20

3.3 Steady-State phasor diagram for optimized rotor flux determination. 25

3.4 Overcurrent protection algorithm. 27

4.1 Simulation results for the steady-state operation of the DFIG at 1250 rpm: (a) electromagnetic and reference torque; (b) stator currents; (c) stator active and reactive power; (d) rotor and stator flux; (e) rotor currents; (f) dc-bus voltage. 30

4.2 Spectra of steady-state operation at 1250 rpm taken from : (a) electromagnetic torque; (b) stator current; (c) stator power. 31

4.3 Simulation results for the steady-state operation of the DFIG at 1750 rpm: (a) electromagnetic and reference torque; (b) stator currents; (c) stator active and reactive power; (d) rotor and stator flux; (e) rotor currents; (f) dc-bus voltage. 32

4.4 Spectra of steady-state operation at 1750 rpm taken from : (a) electromagnetic torque; (b) stator current; (c) stator power. 32

4.5 Simulation results for the steady-state operation of the DFIG at 1520 rpm (synchronous speed): (a) electromagnetic and reference torque; (b) stator currents; (c) stator active and reactive power; (d) rotor and stator flux; (e) rotor currents; (f) dc-bus voltage. 32

4.6 Spectra of steady-state operation at 1520 rpm taken from : (a) electromagnetic torque; (b) stator current; (c) stator power. 33

4.7 Simulation results for the steady-state operation of the DFIG at 1250 rpm and sampling times of 50, 75 and 100 μs: (a) electromagnetic and reference torque; (b) stator currents; (c) stator active and reactive power; (d) rotor and stator flux; (e) rotor currents; (f) dc-bus voltage. 34

4.8 Spectra of rotor voltage at 1250 rpm and at a sampling time of: (a) 50 μs; (b) 75 μs; (c) 100 μs. 35

4.9 Simulation results for the torque ramp response of the DFIG at 1520 rpm, : (a) electromagnetic and reference torque; (b) stator currents; (c) stator active and reactive power; (d) rotor and stator flux; (e) rotor current; (f) dc-bus voltage. 36

4.10 Simulation results for the torque step response of the DFIG at 1250 rpm, : (a) electromagnetic and reference torque; (b) stator currents; (c) stator active and reactive power; (d) rotor and stator flux; (e) rotor currents; (f) dc-bus voltage. 37

4.11 Simulation results for the speed ramp response of the DFIG: (a) electromagnetic and reference torque; (b) rotor speed; (c) stator active and reactive power; (d) rotor and stator flux; (e) rotor currents; (f) dc-bus voltage 37

4.12 Simulation results from the ±30 % rotor resistance variation in the control system: (a) electromagnetic and reference torque; (b) stator currents; (c) stator active and reactive power; (d) rotor and stator flux; (e) rotor current; (f) dc-bus voltage. 38

4.13 Simulation results from the ±30 % rotor leakage inductance variation in the control system: (a) electromagnetic and reference torque; (b) stator currents; (c) stator active and reactive power; (d) rotor and stator flux; (e) rotor current; (f) dc-bus voltage. 39

5.1 Drive components illustration. 43

5.2 Results for the steady-state operation of the DFIG at 1250 rpm: (a) electromagnetic and reference torque; (b) stator currents; (c) stator active and reactive power; (d) rotor and stator flux; (e) rotor currents; (f) dc-bus voltage. 44

5.3 Spectra for the steady-state operation at 1250 rpm taken from: (a) electromagnetic torque using FE; (b) stator current using FE; (c) stator active power using FE; (d) electromagnetic torque using TSE; (e) stator current using TSE; (c) stator active power using TSE. 45

5.4 Results for the steady-state operation of the DFIG at 1750 rpm : (a) electromagnetic and reference torque; (b) stator currents; (c) stator active and reactive power; (d) rotor and stator flux; (e) rotor currents; (f) dc-bus voltage. 45

5.5 Spectra for the steady-state operation at 1750 rpm taken from: (a) electromagnetic torque using FE; (b) stator current using FE; (c) stator active power using FE; (d) electromagnetic torque using TSE; (e) stator current using TSE; (c) stator active power using TSE. 46

5.6 Results for the steady-state operation of the DFIG at 1550 rpm: (a) electromagnetic and reference torque; (b) stator currents; (c) stator active and reactive power; (d) rotor and stator flux; (e) rotor currents; (f) dc-bus voltage. 46

5.7 Spectra for the steady-state operation at 1550 rpm taken from: (a) electromagnetic torque using FE; (b) stator current using FE; (c) stator active power using FE; (d) electromagnetic torque using TSE; (e) stator current using TSE; (c) stator active power using TSE 47

5.8 Results for the DFIG steady-state operation at 1250 rpm, using FE and sampling times of 50, 75 and 100 μs: (a) electromagnetic and reference torque; (b) stator currents; (c) stator active and reactive power; (d) rotor and stator flux; (e) rotor currents; (f) dc-bus voltage 48

5.9 Results for the DFIG steady-state operation at 1250 rpm, using TSE and sampling times of 50, 75 and 100 μs: (a) electromagnetic and reference torque; (b) stator currents; (c) stator active and reactive power; (d) rotor and stator flux; (e) rotor currents; (f) dc-bus voltage. 49

5.10 Spectra of rotor voltage at 1250 rpm using different discretization techniques and sampling times: (a) FE and T_s=50μs; (b) FE and T_s=75μs; (c) FE and T_s=100μs; (d) TSE and T_s=50μs; (e) TSE and T_s=75μs; (f) TSE and T_s=100μs. 49

5.11 Results for a torque ramp response at 1550 rpm using FE : (a) electromagnetic and reference torque; (b) stator currents; (c) stator active and reactive power; (d) rotor and stator flux; (e) rotor currents; (f) dc-bus voltage. 51

5.12 Results for a torque step response at 1550 rpm using TSE : (a) electromagnetic and reference torque; (b) stator currents; (c) stator active and reactive power; (d) rotor and stator flux; (e) rotor currents; (f) dc-bus voltage. 51

5.13 Results of torque step response at 1250 rpm using FE : (a) electromagnetic and reference torque; (b) stator currents; (c) stator active and reactive power; (d) rotor and stator flux; (e) rotor currents; (f) dc-bus voltage. 52

5.14 Results of torque step response at 1250 rpm using Taylor Expansion : (a) electromagnetic and reference torque; (b) stator currents; (c) stator active and reactive power; (d) rotor and stator flux; (e) rotor currents; (f) dc-bus voltage. 53

5.15 Results for a speed ramp response using FE: (a) electromagnetic and reference torque; (b) rotor speed; (c) stator active and reactive power; (d) rotor and stator flux; (e) rotor currents; (f) dc-bus voltage. 53

5.16 Results for a speed ramp response using TSE: (a) electromagnetic and reference torque; (b) rotor speed; (c) stator active and reactive power; (d) rotor and stator flux; (e) rotor currents; (f) dc-bus voltage. 54

5.17 Results for rotor resistance variation using FE: (a) electromagnetic and reference torque; (b) stator currents; (c) stator active and reactive power; (d) rotor and stator flux; (e) rotor currents; (f) dc-bus voltage. 55

5.18 Results for rotor resistance variation using TSE: (a) electromagnetic and reference torque; (b) stator currents; (c) stator active and reactive power; (d) rotor and stator flux; (e) rotor currents; (f) dc-bus voltage 55

5.19 Results for rotor leakage inductance variation using FE: (a) electromagnetic and reference torque; (b) stator currents; (c) stator active and reactive power; (d) rotor and stator flux; (e) rotor currents; (f) dc-bus voltage. 56

5.20 Results for rotor leakage inductance variation using TSE: (a) electromagnetic and reference torque; (b) stator currents; (c) stator active and reactive power; (d) rotor and stator flux; (e) rotor currents; (f) dc-bus voltage. 56

A1 Simulation model of the FCS-MPC control strategy applied to the DFIG-dc system 68

B.1 Magnetizing inductance estimation: a) magnetization curve; b) look-up Table generation 70

C.1 Experimental set-up of the DFIG-dc: (a) doubly-fed induction generator; (b) torque sensor; (c) squirrel-cage induction motor controlled by the VSD . . . 72

C.2 Rotor connected elements: (a) inverter bridge; (b) inductive filter 72

C.3 Stator connected elements: (a) diode bridge; (b) autotransformer 73

C.4 System's dc-link: (a) capacitor-bank; (b) resistive load 73

C.5 VSD used for primary machine control: (a) VSD; (b) VSD's remote controller 74

C.6 Measurement circuit 74

C.7 Control platform dSPACE 1103 75

C.8 Control panel: (a) ControlDesk panel; (b) Yokogawa WT3000 75

C.9 Controller model of the MPC control strategy applied to the DFIG 76

List of Tables

3.1 Switching states of the inverter 22

4.1 Total waveform distortion and prediction errors of the DFIG-dc system at the tested speeds and with a sampling time of 50 μs. 34

4.2 Total waveform distortion and prediction errors of the DFIG-dc system at 1250 rpm and with sampling rates of 50, 75 and 100 μs. 35

4.3 Numeric results for simulated sensitivity analysis of the FCS-MPC algorithm 40

5.1 Total waveform distortion and prediction errors of the steady-state operation of the DFIG, using both discretization techniques 47

5.2 Execution time at tested operating speeds using FE and TSE discretization methods 48

5.3 Total waveform distortion and prediction errors, at 1250 rpm, using the proposed discretization methods and sampling times of 50, 75 and 100 μs. . . . 50

5.4 Total waveform distortion and prediction errors for sensitivity analysis of the DFIG-dc system 57

B.1 DFIG and rotor filter parameters 69

Terminology

Acronyms

AC	Alternating Current
DC	Direct Current
DFIG	Doubly-Fed Induction Generator
ESR	Equivalent Series Resistance
FE	Forward Euler
FCS-MPC	Finite Control Set Model Predictive Control
FRSG	Field Regulated Synchronous Generator
GSC	Grid Side Converter
LVRT	Low Voltage Ride Through
MMF	Magnetomotive Force
MPC	Model Predictive Control
PI	Proportional Integral
PLL	Phase Locked-Loop
PWM	Pulse Width Modulation
RSC	Rotor Side Converter
TSE	Taylor Series Expansion
TWD	Total Waveform Distortion
VSD	Variable Speed Drive
VSI	Voltage Source Inverter
ZOH	Zero-Order Hold

List of Symbols

a	Transformation ratio	
$\underline{a}$	Complex operator	
$\mathbf{A}$	Continuous system matrix	
$\mathbf{A}_d$	Discrete system matrix	
$\mathbf{B}$	Continuous input matrix	
$\mathbf{B}_d$	Discrete input matrix	
$\mathbf{C}$	Output matrix	
$\underline{e}_s$	Stator electromotive force space vector	V
E_{i_r}	Rotor current prediction error	A
$E_{T_{em}}$	Electromagnetic torque prediction error	N.m
E_{ψ_r}	Rotor Flux prediction error	Wb
f_n	Nominal stator frequency	Hz
f_s	Stator frequency	Hz
f_s^*	Stator frequency reference value	Hz
$f_{s_{max}}$	Maximum stator frequency	Hz
g	Cost function	
$\mathbf{I}$	Identity matrix	
I_B	Base current	A
$i_{d,qr}$	dq components of rotor flux space vector	A
$i_{d,qr}[k]$	dq components of rotor flux space vector for instant $[k]$	A
$i_{d,qr}^p[k+1]$	Predicted dq components of rotor flux space vector for instant $[k+1]$	A
$i_{d,qr}^p[k+2]$	Predicted dq components of rotor flux space vector for instant $[k+2]$	A
$i_{d,qr}^p[k+h]$	Predicted dq components of rotor flux space vector for instant $[k+h]$	A
$i_{d,qs}$	dq components of stator flux space vector	A
$\underline{i}_m$	Magnetizing current space vector	A
$i_{m_{pu}}^*$	Reference magnetizing current in per-unit notation	pu
I_n	Nominal current	A
$i_{R_{pu}}^*$	Reference rotor current in Γ equivalent circuit and in per-unit notation	pu
$\underline{i}_R$	Rotor current space vector in Γ equivalent circuit	A
i_{qR}^*	Reference q-axis component of the rotor current in Γ equivalent circuit	A
$i_{qR_{pu}}$	q-axis component of the rotor current in Γ equivalent circuit	pu

	and in per-unit notation	
$i^*_{qR_{pu}}$	Reference q-axis component of the rotor current in Γ equivalent circuit and in per-unit notation	pu
$\left\|i_{R_{pu}}\right\|$	Rotor current in the Γ equivalent circuit and in per-unit notation	pu
I_r	Rotor current	A
$\left\|i_{r_{pu}}\right\|$	Rotor current in per-unit notation	pu
$\underline{i}_r$	Rotor current space vector	A
$\underline{i}_r[k]$	Rotor current space vector at instant $[k]$	A
$\left\|i_r\right\|_{max}$	Rotor current space vector maximum amplitude	A
$\underline{i}^p_r[k+1]$	Predicted rotor current space vector at instant $[k+1]$	A
$\underline{i}^p_r[k+2]$	Predicted rotor current space vector at instant $[k+2]$	A
$\underline{i}^p_r[k+h]$	Predicted rotor current space vector at instant $[k+h]$	A
I_s	Stator current	A
$i_{s_{pu}}$	Stator current in per-unit notation	A
$i_{\alpha\beta s}$	Stator currents in $\alpha\beta$ components	A
$\underline{i}_s$	Stator current space vector	A
$\underline{i}_s[k]$	Stator current space vector at instant $[k]$	A
K_i	Integral gain	
k_{pll}	PLL gain	
L_B	Base inductance	H
L_f	Rotor filter inductance	H
L_{kr}	Rotor leakage inductance in the Γ equivalent circuit	H
L'_{lr}	Rotor winding leakage inductance referred to the stator of the DFIG	H
L_{ls}	Stator winding leakage inductance	H
L_m	Magnetizing inductance	H
$L_{m_{pu}}$	Magnetizing inductance in per-unit notation	pu
L_r	Rotor winding self-inductance	H
L_s	Stator winding self-inductance	H
$L_{s_{pu}}$	Stator self-inductance in per-unit notation	H
n	Harmonic order	
n_r	Rotor speed	rpm

N	Prediction horizon	
N_s	Number of samples	
p	Pole pairs	
P_{inv0}	Full-rating inverter losses	W
$P_{inv0_{pu}}$	Full-rating inverter losses in per-unit notation	pu
P_m	Mechanical power	W
P_n	Nominal power	W
P_r	Three-phase rotor power	W
P_s	Three-phase stator power	W
R_f	Rotor filter equivalent series resistance	Ω
R_R	Rotor winding resistance in Γ equivalent circuit	Ω
$R_{R_{pu}}$	Rotor winding resistance in Γ equivalent circuit in per-unit notation	pu
$R_r^{'}$	Rotor winding resistance referred to the stator of the DFIG	Ω
$R_{r_{pu}}$	Rotor winding resistance in per-unit notation	pu
R_s	Stator winding resistance	Ω
$R_{s_{pu}}$	Stator winding resistance in per-unit notation	pu
s	Laplace Transform operator	
$S_{a,b,c}$	Inverter leg switching state	
$\underline{S}$	Inverter switching state vector	
$\underline{S}[k]$	Inverter switching state vector at instant $[k]$	
$\underline{S}[k+1]$	Inverter switching state vector prediction at instant $[k+1]$	
T_B	Electromagnetic torque base value	N.m
T_e^*	Uncorrected reference electromagnetic torque	N.m
T_{em}^*	Reference electromagnetic torque	N.m
$T_{em_{pu}}^*$	Reference electromagnetic torque in per-unit notation	pu
$\hat{T}_{em}[k]$	Estimated electromagnetic torque at instant $[k]$	N.m
$T_{em}^p[k+1]$	Predicted electromagnetic torque at instant $[k+1]$	N.m
$T_{em}^p[k+2]$	Predicted electromagnetic torque at instant $[k+2]$	N.m
$T_{em}^p[k+h]$	Predicted electromagnetic torque at instant $[k+h]$	N.m
T_{em_corr}	Electromagnetic torque correction term	N.m
T_{em6}	Amplitude of the 6th harmonic of the electromagnetic torque	N.m
T_f	Phased Locked Loop time constant	s

T_L	Load torque	N.m
T_n	Nominal torque	N.m
T_s	Sampling time	s
$TWD_{T_{em}}$	Electromagnetic torque total waveform distortion	
TWD_{ψ_r}	Rotor flux total waveform distortion	
$\mathbf{u}$	Input vector	
$\mathbf{u}[k]$	Input vector at instant $[k]$	
$\mathbf{u}[k+h-1]$	Input vector at instant $[k+h-1]$	
U_B	Base voltage	V
U_n	Nominal voltage	V
U_r	Rotor voltage	V
U_s	Stator voltage	V
u_{dc}	Dc-link voltage	V
$u_{dc}[k]$	Dc-link voltage at instant $[k]$	V
$u_{dc}[k+1]$	Dc-link voltage at instant $[k+1]$	V
$u_{d,qr}[k]$	dq components of rotor voltage space vector at instant $[k]$	V
$u_{d,qr}[k+1]$	dq components of rotor voltage space vector at instant $[k+1]$	V
$\underline{u}_r$	Rotor voltage space vector	V
$\underline{u}_r[k]$	Rotor voltage space vector at instant $[k]$	V
$\underline{u}_r[k+1]$	Rotor voltage space vector at instant $[k+1]$	V
$u_{d,qs}[k]$	dq components of stator voltage space vector at instant $[k]$	V
$u_{d,qs}[k+1]$	dq components of stator voltage space vector at instant $[k+1]$	V
$\underline{u}_s$	Stator voltage space vector	V
$\underline{u}_s[k]$	Stator voltage space vector at instant $[k]$	V
$\underline{u}_s[k+1]$	Stator voltage space vector at instant $[k+1]$	V
$u_{\alpha\beta s}$	Stator voltages in $\alpha\beta$ components	V
x_1	Fundamental component amplitude for quantity x	
x_{rms}	Root mean square value for quantity x	
$x[k]$	State variable at instant $[k]$	
$x[k]^*$	Reference value for state variable at instant $[k]$	
$\mathbf{x}$	State vector	
$\mathbf{x}[k]$	State vector at instant $[k]$	

$\mathbf{x}[k+h-1]$	State vector at instant $[k+h-1]$	
$\mathbf{x}[k+1]^p$	Predicted state vector at instant $[k+1]$	
$\mathbf{x}[k+h]^p$	Predicted state vector at instant $[k+h]$	
$x^p[k+1]$	Predicted state variable at instant $[k+1]$	
$x^p[k+2]$	Predicted state variable at instant $[k+2]$	
$x[k+2]$	State variable at instant $[k+2]$	
$\mathbf{y}$	System output vector	
z	Z-Transform operator	
η	Machine efficiency	
θ_e	Stator angular position	rad
$\hat{\theta}_e$	Estimated stator angular position	rad
$\theta_r[k]$	Rotor angular position at instant $[k]$	rad
$\theta_r[k-1]$	Rotor angular position at instant $[k-1]$	rad
θ_{sl}	Rotor slip angular position	rad
$\hat{\theta_{sl}}$	Estimated rotor slip angular position	rad
λ	Winding losses operational parameter	
λ_{ψ_r}	Weighting factor for flux regulation	
σ	Total leakage factor	
τ	Semiconductor conduction losses operational parameter	
$\psi_{d,qr}$	dq components of rotor flux space vector	Wb
$\hat{\psi}_{d,qr}[k]$	dq components of rotor flux space vector at instant $[k]$	Wb
$\psi^p_{d,qr}[k+1]$	Predicted dq components of rotor flux space vector at instant $[k+1]$	Wb
$\psi^p_{d,qr}[k+h]$	Predicted dq components of rotor flux space vector at instant $[k+h]$	Wb
$\left\lvert\underline{\psi}^*_r\right\rvert$	Reference rotor flux space vector amplitude	Wb
ψ_{rn}	Rotor flux nominal value	Wb
ψ_r^{*opt}	Optimized rotor flux reference value	Wb
$\psi_{r_{pu}}^{*opt}$	Optimized rotor flux reference value in per-unit notation	pu
$\underline{\psi}_r$	Rotor flux space vector	Wb
$\hat{\underline{\psi}}_r[k]$	Estimated rotor flux space vector at instant $[k]$	Wb
$\underline{\psi}^p_r[k+1]$	Predicted rotor flux space vector at instant $[k+1]$	Wb
$\underline{\psi}^p_r[k+2]$	Predicted rotor flux space vector at instant $[k+2]$	Wb
$\underline{\psi}^p_r[k+h]$	Predicted rotor flux space vector at instant $[k+h]$	Wb

$\psi_{d,qs}$	dq components of stator flux space vector	Wb
$\hat{\psi}_{d,qs}[k]$	Estimated dq components of stator flux space vector at instant $[k]$	Wb
ψ_{s_max}	Maximum stator flux value	Wb
ψ_{s_min}	Minimum stator flux value	Wb
$\psi_{s\_min}^{opt}$	Optimized value for minimum stator flux	Wb
$\psi_{s_{pu}}$	Stator flux value in per-unit notation	pu
ψ_{s}^{opt}	Optimized stator flux value	Wb
$\psi_{s_{pu}}^{opt}$	Optimized stator flux value in per-unit notation	pu
$\underline{\psi}_s$	Stator flux space vector	Wb
$\underline{\hat{\psi}}_s[k]$	Estimated stator flux space vector at instant $[k]$	Wb
Ω_r	Mechanical rotor angular speed	rad/s
ω_B	Base angular frequency	rad/s
ω_e	Stator angular frequency	rad/s
ω_n	Nominal angular frequency	rad/s
$\hat{\omega}_r$	Rotor angular frequency	rad/s
$\hat{\omega_r}[k]$	Estimated rotor angular frequency at instant $[k]$	rad/s
ω_{sl}	Slip angular frequency	rad/s
ω_{ff}	Phased Locked Loop centre frequency	rad/s
$\otimes$	Cross product	

Subscripts and Superscripts

Subscript

a, b, c	Natural reference frame
B	Base quantities
dc	dc quantities
pu	Per-unit quantities
s, r	Stator or rotor quantities
R	Rotor in the Γ equivalent circuit
α, β	Stationary reference frame

Superscript

$*$	Reference value
$\wedge$	Estimated value
$'$	Quantity referred to the stator of the DFIG
p	Predicted value
opt	Optimized quantity

Chapter 1

Introduction

1.1 Framework

Microgrids are defined as small-scale grids that incorporate distributed generation sources (such as wind turbines or photovoltaic panels, etc.), energy storage systems (batteries, ultra-capacitors, etc.) and loads. This concept has been developed to tackle the issue of increasing renewable-energy demand, its integration and control into an also developing smart-grid, in which the final user may be able to generate, store and manage part of the energy that it will consume [1, 2].

Nowadays, one of the most mature renewable-energy technology used for distributed generation is wind energy, accounting for approximately 20% of all renewable-energy production, and 5% of the world's electricity consumption [3]. In the process of converting the wind's kinetic energy into usable electricity, there are 4 machines that stand-out: the squirrel-cage induction generator, the doubly-fed induction generator (DFIG), the field-regulated synchronous generator (FRSG) and the permanent-magnet synchronous generator.

The DFIG, although presenting higher initial and maintenance costs than the simpler squirrel-cage induction generator, proves itself as a more attractive option than the latter, due to an extended speed of operation, full rotor voltage controllability, and increased efficiency of the energy conversion system [4]. The use of the DFIG also brings a de-rating for the used power converter to a fraction of the rated rotor power (30%) [3–6], when compared to the also widely used FRSG. Additionally, connecting the FRSG to the grid at a low speed of operation implies that the magnetic circuit of the machine has to oversized, in order

to cope with a constant electromotive force and growing flux, resulting in a more bulky generator [5,6]. This means that, when grid-connected, the DFIG is capable of proper stator frequency regulation, independent of rotor speed. The use of permanent magnet synchronous generators is also widespread, attesting to its higher power density and efficiency, simple design and lower maintenance costs. However, its high capital cost, need for fully-rated converter and possible demagnetization of permanent magnets can make it a less appealing option than the DFIG, who currently dominates the wind industry with a market share of 50% on all electric generators [3].

The most prevalent technology is still the DFIG connected to the ac mains [3, 7], but the growing trend of decentralized power generation unveiled the need to connect different types of generators working in a wide range of speeds, as well as a variety of energy storage systems and power converters. According to the authors of [8,9], employing a dc network can increase the system's efficiency, reduce the implementation costs and simplify all paralleling operations due to the absence of multiple ac-dc-ac conversion stages, as well as the need for lighter and smaller cables. The lack of reactive power and of frequency synchronization contribute to a more stable system and simpler control algorithm. Additionally, the non-existence of skin-depth and the possibility of underwater power transmission also assist for the dc network to be acknowledged as a viable option [2].

The development of more refined control schemes is a pressing issue for a system to achieve good steady-state and dynamic performance, increased efficiency and compliance with ever more demanding grid codes [10]. The simpler and more widely used field oriented control (FOC) brings several drawbacks such as inferior dynamic response, and the existence of a cascaded control structure, whose stability is heavily dependent on the inner control loop's performance [11]. Furthermore the tuning of these inner control loop parameters is a very time-consuming task. To overcome these drawbacks, several control strategies have been proposed, for which model predictive control (MPC) has been considered one of the most attractive. Briefly, the objective of MPC is the prediction of the future behaviour of the system, whose result is used by the controller to obtain the optimal possibility of actuation, according to a predefined optimization criterion [11]. It has the advantage of eliminating the need for any Proportional-Integral (PI) controller, but makes the algorithm very computational demanding and dependent on the accuracy of obtained discrete models [3]. The limitation of computational power of digital signal processors (DSPs) require the

designer to make a trade-off between the accuracy of the sampled-data model, and simplicity, so that the required predictions can properly describe the system's behaviour and satisfy the sampling time restriction.

1.2 Motivation and Objectives

Attending to the established use of the DFIG and all the advantages that make the dc grid a competitive alternative to the ac mains, there is a necessity to study this machine connected to this type of grid. Additionally the results obtained on the use of MPC on other electric drives, motivate this type of control method to be extended to the DFIG-dc system. Although various discretization techniques for non-linear systems exist, there is no straightforward comparison between them on the system's performance, be it in steady-state or dynamic regime. This motivates the study of different discretization techniques, and to assess if the use of more elaborate methods can compensate their increased computational burden. As such this dissertation's objectives are:

- Study the main characteristics of the DFIG connected to a dc grid;
- Test and implement a FCS-MPC-based control system capable of operating the DFIG-dc, first in a simulated environment (*MATLAB/Simulink*), and then in real-time, using a digital control platform;
- Obtain different models for the system, through the use of alternative discretization methods and compare the results obtained with each one.

Chapter 2

DFIG-dc systems

2.1 Introduction

The DFIG-dc system is basically a topology where both the rotor and stator terminals are connected to a common dc bus [5]. Fig. 2.1 illustrates this topology. The use of a diode rectifier to connect the stator of the DFIG to the dc-link is justified by its simplicity and cost-effectiveness. The rotor is fed by a de-rated voltage source inverter (VSI) converter because it allows the control of rotor currents in amplitude, phase and frequency by applying suitable voltage vectors [12]. However, if the stator and rotor windings present an unequal number of turns, a step-down transformer connected between the stator and diode rectifier must be used. This will ensure that the rotor side converter (RSC) input and grid side converter (GSC) output voltages are the same, allowing the shared use of the dc bus [12, 13].

Alternatively, two VSIs were proposed in [15] to connect the stator and rotor of the DFIG to the same dc-link, and by controlling the stator frequency to operate the system with a rotor slip of -1, the de-rating of the VSIs to half power is possible. The main disadvantages of this approach is that a coordinated control strategy for both converters is needed, which increases its complexity, besides not reducing the system cost [15, 16].

The inclusion of the uncontrolled diode bridge on the stator side implies that the stator of the DFIG cannot supply any magnetizing current, therefore all of it must be provided by the RSC. If the rotor is not able to provide the needed magnetizing flux, poor power factor on the stator side is expected [12]. As such, the rotor should be rated with a higher MMF than the

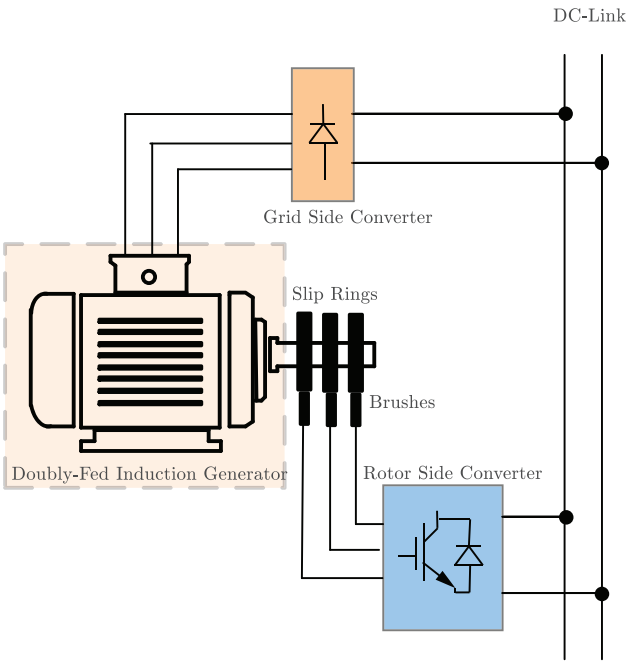

Fig. 2.1: DFIG-dc system with diode rectifier connected to the stator and voltage source inverter connected to the rotor [14]

.

stator [17, 18]. Furthermore, proper frequency regulation must be implemented, since it is not imposed by any ac grid, nor by the rotor speed. This condition guarantees that nominal power is reached with the rated stator flux. However, this system has the characteristic that it operates under an almost constant stator voltage (imposed by the diode bridge), which means that the machine operates with a constant product of stator flux amplitude by stator frequency. This relation makes stator frequency controllable indirectly through flux [19].

As described in [5, 13, 15–17, 20, 21] the simplicity and low-cost of the diode rectifier can be appealing, but a highly distorted stator voltage and flux linkage is expected due to the injection of stator current harmonics by the uncontrolled bridge. These harmonics will be of $6n \pm 1$ order. When the 5^{th} and 7^{th} harmonic components of the stator current interact with the fundamental component of the stator flux, a pulsating torque with six times the fundamental frequency appears [22]. Similarly, the interactions between the fundamental component of the stator flux and the 11^{th} or 13^{th} harmonic components of the stator current will produce a pulsating torque with twelve times the fundamental frequency. This torque ripple is responsible for reducing the life of the mechanical components of the system, *i.e.* bearings and drive-train [17]. Additionally, the presence of current harmonics can result in overheating or unequal heating of the DFIG's windings [22]. A major decrease in current

harmonics and torque ripple can be obtained by the employment of a 12-pulse rectifier instead of the full-wave uncontrolled bridge, but this configuration is only possible with two sets of stator windings [17]. Another alternative is the use of shunt or active power filters to compensate current harmonics, but the major setback of this approach is the necessity of an additional VSI [23]. Since these solutions imply increased implementation costs, several control algorithms were developed to improve torque reference tracking [17, 20, 21, 24].

The use of a dc system also contributes to make LVRT capability simpler and less expensive than in its ac counterpart [25]. If the grid experiences a voltage dip, high rotor voltages are induced by the dc components of the stator flux. To prevent the disconnection of rotor terminals, the VSI would have to be sized to at least a voltage equal to the maximum induced rotor voltage [26]. However, if the DFIG is connected to a dc network, then it is possible to implement LVRT using only the de-rated RSC [25]. LVRT capability is of relevance since most grid codes in Europe dictate that during the dip, the wind turbine must remain connected to the grid, and contribute to restore the voltage levels [10]. However since this subject is outside the scope of this work, it will not be further addressed.

In the system under study, we can find two variants: a DFIG-dc system connected to a dc grid and a DFIG-dc system in stand-alone operation. If connected to a dc-grid, the assumption that other elements in the grid are responsible for maintaining the dc-link voltage at a constant level make the main control objectives to be the flow of active power and frequency regulation [18]. However, while operating the stand-alone DFIG-dc system, the control objectives are both the regulation of load voltage and the fulfilment of load power requirements in transient and steady-state conditions [18]. The stand-alone operation of the DFIG also needs a battery (in series with a diode) at the beginning of operation. The battery will allow the VSI to energize the system and establish the stator flux. When the dc-link voltage level increases above the battery voltage, the diode stops conducting, and the battery is in open-circuit [27].

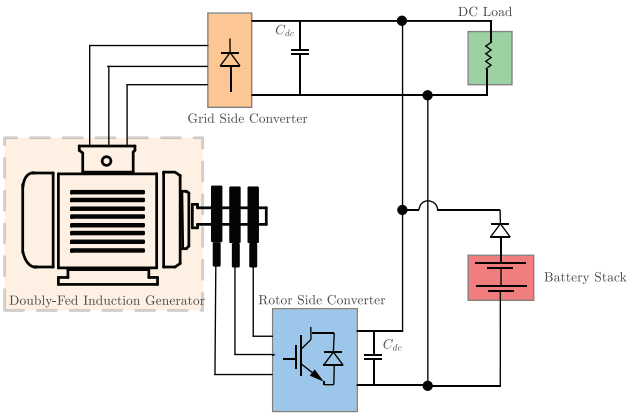

Fig. 2.2: Stand-alone DFIG-dc system with diode rectifier connected to the stator and voltage source inverter connected to the rotor.

2.2 State of the Art of Control Strategies for DFIG-dc Systems

2.2.1 Vector Control Strategies

Since the primary objectives of control are frequency regulation and control of the active power flow, these variables need to be decoupled, and the more conventional method to tackle this issue is with field oriented control (FOC) [28]. By aligning the reference frame with the stator flux $\underline{\psi}_s$(Fig. 2.3a) independent control of flux and torque is achieved, which in turn will regulate the stator frequency and the flow of active power, respectively.

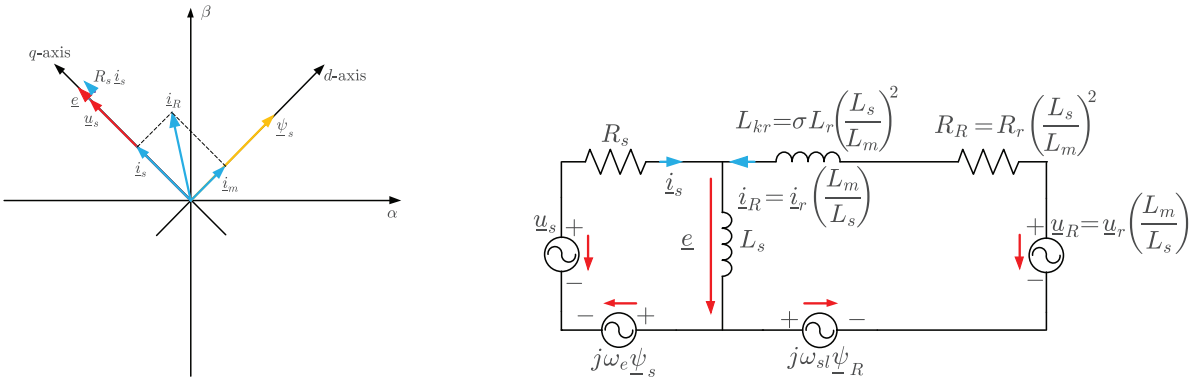

(a) **(b)**

Fig. 2.3: Steady-State model of the DFIG-DC system: (a) phasor diagram for positive slip operation [29]; (b) equivalent Γ circuit of the DFIG in a synchronous reference frame [27].

It's worth mentioning that although the reference frame can also be aligned with the

stator voltage $\underline{u}_s$, this method is considered inadequate for this system, due to the highly distorted voltages that result from the diode rectifier operation [16].

Figure 2.4 shows a general FOC scheme applied to the DFIG-dc system. In this system the d-axis rotor current i_{dr} is manipulated to regulate the stator frequency ω_e by adjusting the stator flux ψ_s. This option as a control variable for frequency comes from the constant dc-link voltage that imposes an also constant $\psi_s \times \omega_e$ product, making frequency controllable through flux [28]. The q-axis rotor current i_{qr} controls torque T_{em}, which means it also adjusts the flow of active power to the dc bus.

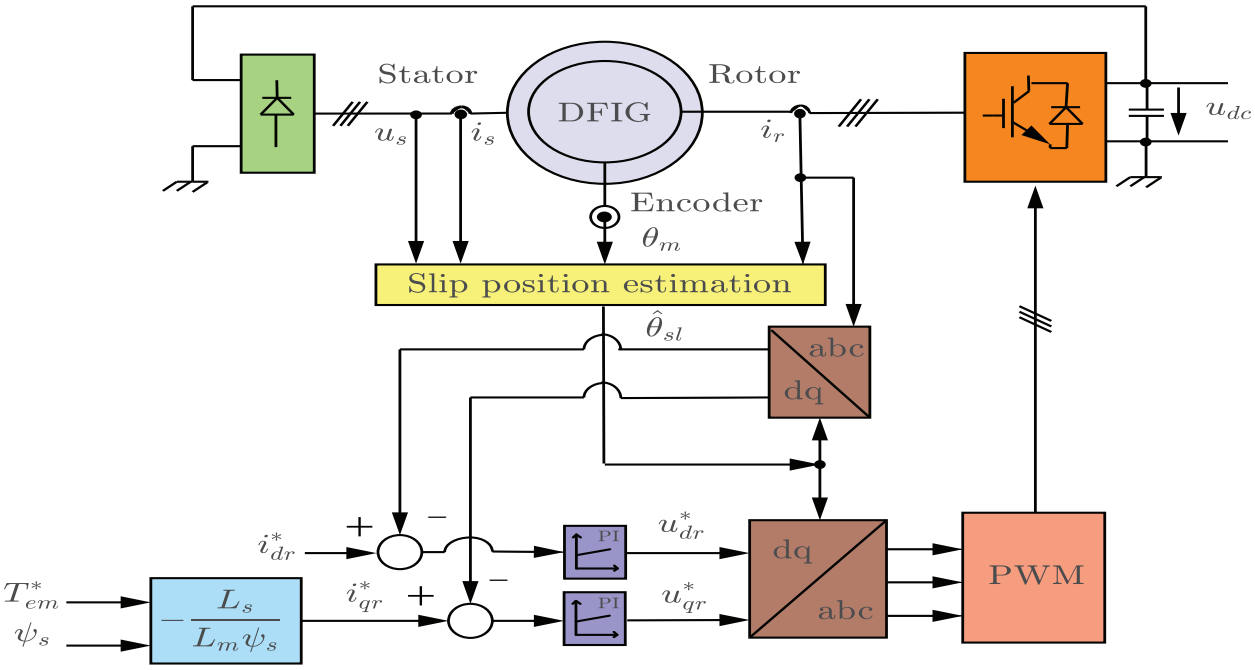

Fig. 2.4: General field oriented control scheme [28]

Field orientation requires the knowledge of slip frequency ω_{sl} for reference frame transformations. It is obtained by the derivative of the slip angle θ_{sl}, defined as the difference between the stator flux space vector angle and the electrical rotor position. As such, both stator flux estimation and an encoder are required. This stator flux estimator can be implemented by the integration of stator voltages. However, in a practical setting it is necessary to eliminate sensor offsets and take initial conditions into account.

Furthermore, since the DFIG stator frequency of operation is not rigid, there is a necessity to drive the stator flux to rotate at a constant frequency, ideally at 50 Hz [28]. The author proposes in [6] the definition of an orientation error angle, defined as the difference between the intended reference frame angle and the estimated stator flux space vector angle. It

also supports that this error propagates to the d-axis rotor current, therefore the use of a PI controller for the regulation of this current component can lead to the extinction of the orientation error and achieve null steady-state frequency error. All these angles are obtained by the integration of their respective frequencies, requiring the aid of an additional synchronization loop. This loop's gain is dependent on the q-axis rotor current i_{qR} making it behave inadequately at no load, calling for a different approach when torque approaches zero. The same author introduces in [19] the use of reference stator flux angle in frame transformations, instead of the estimated stator flux angle. This allows for the position of stator reference frame to be properly driven, even at no-load conditions.

In [30] a scheme for power control for the DFIG-dc was introduced. It advocates that acting on a fraction of the rotor flux linkage space vector regulates the delivered power to the dc-bus. Torque and dc power are regulated by adjusting the rotor current space vector amplitude, while its speed of reference dictates the stator frequency. It also defined a commutation inductance, as a fraction of the leakage inductance, and it can be used to minimize the DFIG de-rating due to the stator current distortion and phase shift.

To avoid the use of an encoder, a slip angle estimator for the DFIG-dc system has been developed in [31]. The authors define this angle as the difference between rotor current space vector positions, estimated both in rotor and field coordinates. The former angle is defined as a function of the rotor currents in a stationary frame, while the latter is determined through estimations of active power across the air-gap.

The need for a stator flux estimator can be avoided by the use of a PLL (Fig 2.5). It is characterized by a gain k_{pll}, time constant T_f and centre frequency ω_{ff}. It estimates frequency $\hat{\omega}_e$ and the error of this estimation is used for d-axis rotor current regulation. The

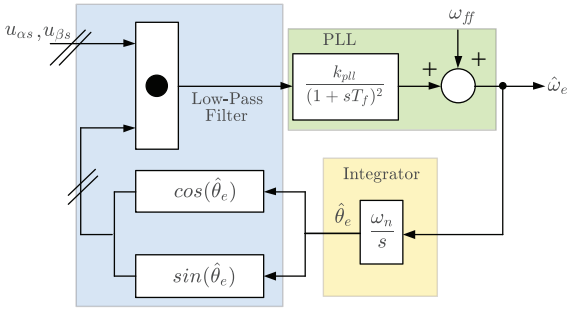

Fig. 2.5: PLL for stator frequency estimation [32]

absence of the stator flux estimator implies that the poorly damped oscillations of the stator

flux linkage are not reflected into the control chain [29,31,32]. However the rectifier imposes heavily distorted stator voltages, justifying the use of a low-pass filter in order to smooth the frequency estimation [33]. This filter calculates a dot product between the stator voltage and the sine and cosine of the estimated phase angle $\hat{\theta}_e$. The PLL can also track the frequency at no-load, simplifying the control algorithms at very low or zero torque [31]. It can also handle small frequency deviations, as long as it has a strict frequency set-point, however a broad variation in this parameter results in undesirable interaction with the current controllers. Therefore its use is inappropriate if combined with the field-weakening control method, brought by [34], where the frequency is changed in order to regulate the flux level at light load. This is adjusted in order to minimize losses by Joule effect in the stator windings.

The first sensorless control method for this system was described in [29] with an alternative to deal with loaded and no-load operation, using two PI controllers, one for each condition. The estimated slip position is obtained by integrating the estimation of slip frequency (provided by a third PI controller). For loaded conditions this PI controller acts on the error between the modulus of the stator current and the estimated q-axis rotor current. However, at no-load a constant d-axis rotor reference current is set, while the PI controller handles the frequency error. This sensorless control method was later on adapted to work in stand-alone systems in [32].

Torque ripple reduction is an issue that can be addressed by acting only on the rotor VSI. Due to the oscillations on the stator flux, at six times the stator frequency, both torque and the q-axis reference current contain a significant ripple at that frequency. If this harmonic component of rotor current can be properly tracked, then it is possible to suppress the corresponding ripple component from the electromagnetic torque. However, it's not possible to obtain better tracking of the sixth harmonic of rotor current using a PI controller, as it would require an impractical bandwidth [20].

A resonant current controller can be used in parallel with the other PI controllers used in the current loops, to keep track of the sixth harmonic component and remove it from the electromagnetic torque (Figure 2.6). Its purpose is to achieve an unitary gain and zero phase shift closed-loop transfer function at a frequency equal to the sixth harmonic $6\omega_b$ [16], and generate a corrected q-axis rotor current component capable of suppressing the unwanted ripple. The use of this type of controller preserves the low bandwidth of the current controllers, thereby avoiding the reduction of stator flux damping. However the

system is not robust against frequency deviations and tuning the resonant controllers can be a troublesome task [20]. Additionally, the use of the resonant controller deals only with one specific harmonic component, and as such, the controller complexity increases if the tracking and suppression of additional harmonic sequences is intended [35]. In spite of that, it still demonstrated the ability to accurately track the reference torque, even under distorted grid voltages [16]. Another alternative is the tuning of different current controllers implemented

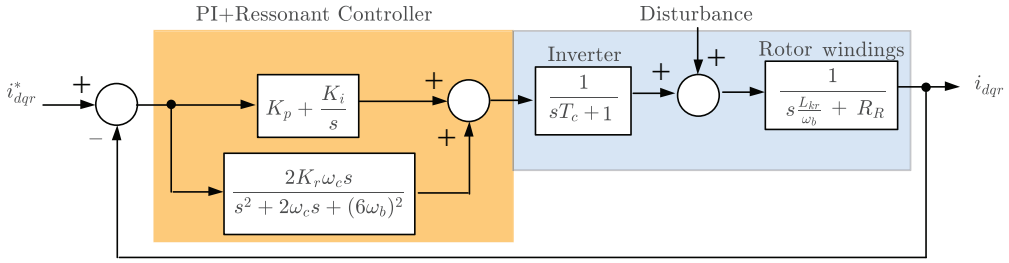

Fig. 2.6: Current loops with PI+Ressonant controller [20]

in multiple harmonic reference frames [21]. This works by decomposing the stator current into different and isolated harmonic components, which are tracked and forced to zero by additional PI controllers.

The use of these more complex controllers can be avoided, according to [17]. The author proposes an estimation of the reciprocal of the stator flux amplitude, and whose result is introduced in the torque expression, in order to obtain the reference q-axis rotor current. The prediction horizon used in the estimation must be equal to the time constant of the current control in order to take into consideration its control delay. A corrected q-axis reference current is generated to force torque ripple suppression, however, for it to work properly it needs disturbance compensation terms for transient rotor electromotive force. This method allows the system to retain the classical PI controllers used in the current loops. Although the title invokes predictive control, this method is not MPC-based because it does not determine the best applicable voltage vector based on the minimization of a cost function.

2.2.2 Model Predictive Control

MPC cover a range of non-linear control methods whose essence lies in the use of a model to predict the future behaviour of the system's controlled variables. MPC also has the convenience that it doesn't need a linearized model for it to work and non-linearities are easily included in the model. This avoids the need to linearize the model for a desired

operating point. It also means that this control method can be used in any reference frame, not just the synchronous frame [11]. This avoids the use of the cascaded control loop, and of an increasing number of PIs that need proper tuning, which characterizes the FOC, and whose inner bandwidth is responsible for limiting the system's dynamic response.

MPC can be widely categorized into continuous control set and finite control set MPC (FCS-MPC). In continuous time MPC, the future behaviour of each tracking errors is predicted using Taylor Series Expansion up to the relative degree with respect to the input [36]. It solves an open-loop receding horizon optimization problem at each sampling period and the converter voltage is applied using a PWM, and therefore the switching frequency can be considered fixed [37]. However, its application is more computational demanding and requires the use of a modulator.

On the other hand, FCS-MPC has the possibility to include the discrete nature of power converters, allowing the simplification of the optimization problem and its online implementation. The number of calculations is related to the number of phases and the number of converter legs. In the case of a three-phase two-level inverter, it results in eight possible switching states [11]. It evaluates each admissible actuation within the prediction horizon, and uses the gating signals of the power switches as control inputs. Therefore FCS-MPC controller can directly output a switching state to the converter, without the requirement of a modulation stage [38].

The model used to describe these predictions can be expressed as a discrete time state-space model:

$$\mathbf{x}[k+1] = \mathbf{A}_d\, \mathbf{x}[k] + \mathbf{B}_d\, \mathbf{u}[k] \tag{2.1}$$

$$\mathbf{y}[k] = \mathbf{C}\, \mathbf{x}[k] \tag{2.2}$$

$\mathbf{x}[k]$ and $\mathbf{x}[k+1]$ represent the state vector at instant $[k]$ and $[k+1]$,respectively. $\mathbf{u}[k]$ and $\mathbf{y}[k]$ stand for the input and output vectors, while $\mathbf{A}_d$, $\mathbf{B}_d$ and $\mathbf{C}$ represent the system, input and output matrices in discrete time. The controller then uses this predictions, and according to a optimization criterion, chooses the optimal actuation for the system. This is usually defined as a cost function g to represent the intended behaviour for the system within a predefined prediction horizon N [38]. This optimization problem is repeated using new measurements, resulting in new predictions to be evaluated by the cost function, at every iteration.

The cost function evaluates the tracking of the desired state variables, hence it has usually several terms that describe the difference between the reference values of a quantity x^* and the predicted values N samples ahead $x[k+N]$. This results in a sequence of optimal actuations, but the controller applies the one with the lowest value in the cost function

$$\begin{aligned} g &= x^* - x[k+N] \\ u[k] &= \arg\ \min(g) \end{aligned} \tag{2.3}$$

It is also simple to include restrictions, different control objectives and variable constraints. Additionally, if multi-variable control is intended, one can define a weighting factor for each term in the cost function to adjust its importance [11]. However to get a satisfactory trade-off between the control objectives, the choice of appropriate weighting factors is needed.

In each sampling time there is a switching state selection problem that must be solved based on the predictions for the controlled variables, therefore system modelling and accurate discrete-time models are of vital importance to achieve high performance dynamics. Through the use of a ZOH the input is updated at certain time instants and this value is held between sampling periods. This method gives an exact sampled-data model, in the sense that the continuous-time output is exactly recovered at the sampling instant [37].The use of Tustin's method or Matrix factorization to discretize time-varying systems can also be considered as exact. However, their calculation can be very time-consuming, owing to its heavy computational burden, and therefore approximate methods are employed.

In literature, Forward-Euler is the most used and simple approximation method [11]. However, when short-horizon MPC is used, it can suffer from performance deterioration [39]. The accuracy of the discrete-time model can be increased by the use of an alternative discretization technique, one that sufficiently describes the relations between the state variables. Based on [37, 39–42] the most promising approximate method appears to be the Taylor Expansion. This procedure leads to a discrete-time model where the effect of the input appears in all state variables after one sampling interval [37, 39].

The influence of one-step delay in practical digital implementations can result in aggravated torque or flux ripple. Since the necessary measured variables are sampled at the k^{th} instant, and the DSP cannot perform the required calculations instantaneously, the optimal voltage vector will not be applied until the $(k+1)^{\text{th}}$ instant. As a result the vector applied

at the $(k+1)^{\text{th}}$ instant is not necessarily the best one, resulting in the variables presenting more ripple [11]. A simple solution to compensate this delay is to take into account the calculation time and apply the selected switching state after the next sampling period T_s. The variables are predicted one-sample ahead $\hat{x}[k+1]$, based on present values $x[k]$ at instant k. The prediction of the same variables at time $(k+2)$ is made, considering every hypothesis of actuation and used for the minimization of the cost function. This dynamic of prediction is illustrated in Figure 2.7.

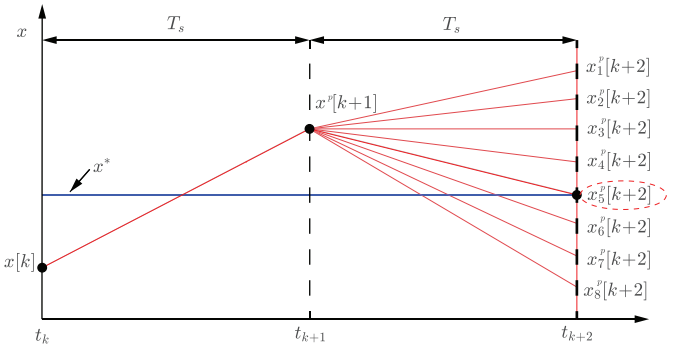

Fig. 2.7: Operation of FCS-MPC with delay compensation.

The most popular FCS-MPC methods applied to electrical drives are predictive current control and predictive torque control [43]. These methods are very close related, with the major difference being the term that is evaluated in the cost function. In the former method, the cost function evaluates the error between predicted and measured orthogonal components of rotor current, while the latter considers the error between predicted and estimated torque.

With only one predictive current control method described for the DFIG-dc system [14], the author does not address torque regulation, nor compensation of the aforementioned torque ripple that characterizes this particular topology. The control system was implemented in a synchronous frame, therefore the estimation of its angular position θ_e is required (Figure 2.8). It is made through the orthogonal components of stator current, in a stationary frame, $i_{\alpha\beta s}$. Then, a discrete-time derivative block (using forward Euler method) is applied to obtain the synchronous angular speed ω_e, and a PI controller is used to eliminate the error between actual and reference frequency f_e^*. Its output is used as a slip angular speed ω_{sl}, and a discrete-time integrator is used to obtain the slip angular position θ_{sl}. It also allows for the estimation of rotor frequency ω_r, thereby dismissing the encoder. This solution can be considered robust against generator parameter deviations, due to its independence from them. Additionally, in [14] only short-horizon MPC was considered, meaning that the delay

of the algorithm was not properly compensated.

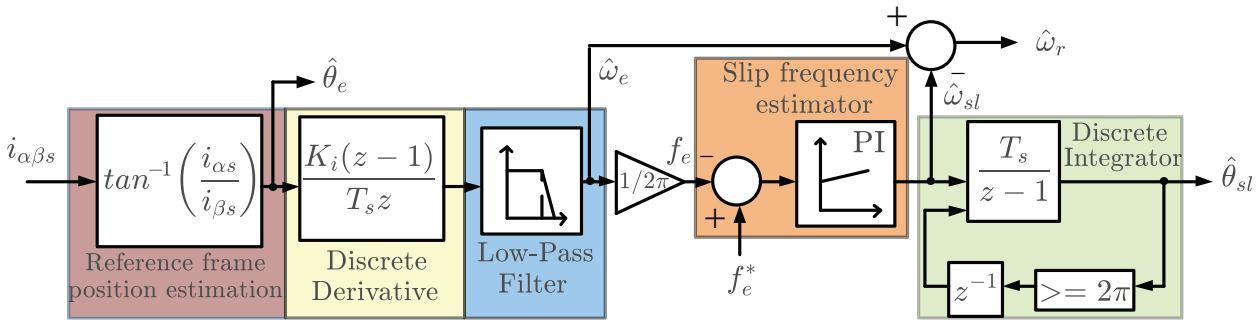

Fig. 2.8: Sensorless method for slip angle position estimation [14].

Chapter 3

Predictive Torque and Rotor Flux Control

3.1 Mathematical Model

The equivalent circuit of a DFIG, in the rotor reference frame and aligned with the rotor flux, is presented in Figure 3.1. All rotor quantities are referred to the stator windings of the machine. In this equivalent circuit, ω_r is the rotor electrical angular speed, R_s and $R_r^{'}$ represent the stator and rotor windings resistance, L_{ls} and $L_{lr}^{'}$ stand for the leakage inductances of the stator and rotor while L_m symbolizes the magnetizing inductance of the machine. $\underline{u}_s$, $\underline{u}_r^{'}$, $\underline{i}_s$, $\underline{i}_r$, $\underline{\psi}_s$, $\underline{\psi}_r$ denote the space vectors of stator and rotor voltage, current and flux, respectively.

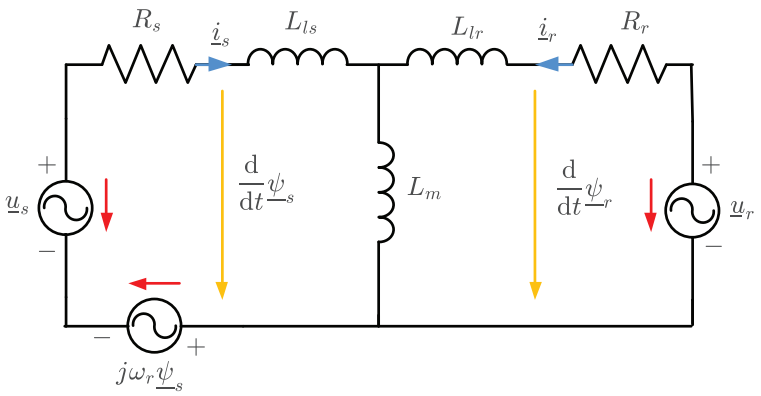

Fig. 3.1: Equivalent circuit of a DFIG in a rotor reference frame.

The voltage equations for both the stator and rotor are given by:

$$\underline{u}_s = R_s \, \underline{i}_s + \frac{\mathrm{d}\underline{\psi}_s}{\mathrm{d}t} + j\omega_r \underline{\psi}_s \tag{3.1}$$

$$\underline{u}_r^{'} = R_r^{'} \underline{i}_r + \frac{\mathrm{d}\underline{\psi}_r}{\mathrm{d}t}. \tag{3.2}$$

These equations are similar to the ones presented for the classical induction machine, however the rotor voltage is not zero in this case.

The stator and rotor fluxes are estimated using:

$$\underline{\psi}_s = L_s \underline{i}_s + L_m \underline{i}_r \tag{3.3}$$

$$\underline{\psi}_r = L_r \underline{i}_r + L_m \underline{i}_s, \tag{3.4}$$

where L_s and L_r represent the stator and rotor self-inductances, which are given by:

$$L_s = L_{ls} + L_m \tag{3.5}$$

$$L_r = L_{lr}^{'} + L_m. \tag{3.6}$$

After some manipulation of (3.3), the stator flux can be expressed as a function of the rotor current and rotor flux:

$$\underline{\psi}_s = \frac{L_s}{L_m}(\underline{\psi}_r - \sigma L_r \underline{i}_r), \tag{3.7}$$

with σ representing the total leakage factor of the machine, given by:

$$\sigma = 1 - \frac{L_m^2}{L_s L_r}. \tag{3.8}$$

By replacing (3.7) into (3.1), one obtains:

$$\frac{\mathrm{d}\underline{i}_r}{\mathrm{d}t} = \frac{R_s + j\omega_r L_s}{\sigma L_r L_s}\underline{\psi}_r - \frac{R_s L_r + R_r L_s + j\omega_r \sigma L_r L_s}{\sigma L_r L_s}\underline{i}_r + \frac{1}{\sigma L_r}\underline{u}_r - \frac{L_m}{\sigma L_r L_s}\underline{u}_s \tag{3.9}$$

The electromagnetic torque developed by the DFIG is given by the cross-product $\otimes$ between $\underline{i}_r$ and $\underline{\psi}_r$:

$$T_{em} = \frac{3}{2}p(\underline{i}_r \otimes \underline{\psi}_r) = \frac{3}{2}p(\psi_{qr} i_{dr} - \psi_{dr} i_{qr}) \tag{3.10}$$

where p stands for the number of pole pairs, i_{dr}, i_{qr}, ψ_{dr}, ψ_{qr} represent the direct and quadrature components for the rotor current and rotor flux space vectors, respectively.

The rotor speed ω_r, needed for these calculations is defined as the derivative of the rotor position θ_r

$$\frac{\mathrm{d}\theta_r}{\mathrm{d}t} = \omega_r \tag{3.11}$$

We have defined a set of differential equations that describe the model of the DFIG given by (3.12).

$$\frac{\mathrm{d}}{\mathrm{d}t}\begin{bmatrix}\underline{\psi}_r \\ \underline{i}_r \\ \theta_r\end{bmatrix} = \begin{bmatrix}-R_r\underline{i}_r + \underline{u}_r \\ \frac{R_s+j\omega_r L_s}{\sigma L_r L_s}\underline{\psi}_r - \frac{R_s L_r + R_r L_s + j\omega_r \sigma L_r L_s}{\sigma L_r L_s}\underline{i}_r + \frac{1}{\sigma L_r}\underline{u}_r - \frac{L_m}{\sigma L_r L_s}\underline{u}_s \\ \omega_r\end{bmatrix} \tag{3.12}$$

Since the predictive algorithm uses the future values for both rotor current and rotor flux to make predictions of torque, these can be considered as the state variables of the system $\mathbf{x} = [\underline{\psi}_r\ \underline{i}_r]^T$, while the control vector is built using both rotor and stator voltage $\mathbf{u} = [\underline{u}_r\ \underline{u}_s]^T$. The use of (3.2) and (3.9) results in the system represented in state-space form by (3.13)

$$\dot{x}(t) = \mathbf{A}\mathbf{x}(t) + \mathbf{B}\mathbf{u}(t) \tag{3.13}$$

where $\mathbf{A}$ and $\mathbf{B}$ represent the system matrix and the control matrix, respectively, and are given by:

$$\mathbf{A} = \begin{bmatrix}0 & -R'_r \\ \frac{R_s+j\omega_r L_s}{\sigma L_r L_s} & -\frac{(R'_r L_s + L_r R_s) + j\omega_r \sigma L_r L_s}{\sigma L_r L_s}\end{bmatrix} \tag{3.14}$$

$$\mathbf{B} = \begin{bmatrix}1 & 0 \\ \frac{1}{\sigma L_r} & \frac{-L_m}{\sigma L_r L_s}\end{bmatrix}, \tag{3.15}$$

The model of the DFIG needs to be discretized as the FCS-MPC algorithm needs a discrete time model to be implemented in a digital control platform. However, due to its high non-linear nature, a ZOH model can be impossible to obtain, which makes the use of numerical approximations a necessity [37].

3.2 Discretization Methods

Since it is assumed that the rotor position is being measured, the rotor speed $\hat{\omega_r}[k]$ can be estimated for instant k by:

$$\hat{\omega_r}[k] \approx \frac{\theta_r[k] - \theta_r[k-1]}{T_s} \tag{3.16}$$

where $\theta_r[k]$ and $\theta_r[k-1]$ represent the electrical rotor position for instants k and $k-1$, respectively. T_s is the sampling period used by the control algorithm.

In (3.3) and (3.4), the stator and rotor fluxes $\underline{\hat{\psi}}_s[k]$ and $\underline{\hat{\psi}}_r[k]$ can be estimated directly using a discrete version of the current model:

$$\underline{\hat{\psi}}_s[k] = L_s \underline{i}_s[k] + L_m \underline{i}_r[k] \tag{3.17}$$

$$\underline{\hat{\psi}}_r[k] = L_r \underline{i}_r[k] + L_m \underline{i}_s[k] \tag{3.18}$$

The RSC is a three-phase VSI modelled as six power switches and is illustrated in Figure 3.2. As each inverter leg can only have one switch turned on at the same time, the switches in each leg receive complementary signals. To represent which switch is turned on, each inverter leg is represented by a switching state $S_a[k]$, $S_b[k]$, $S_c[k]$, which assume the value of 1 or 0 depending if it is either the top or bottom switch of each leg that conducts, respectively.

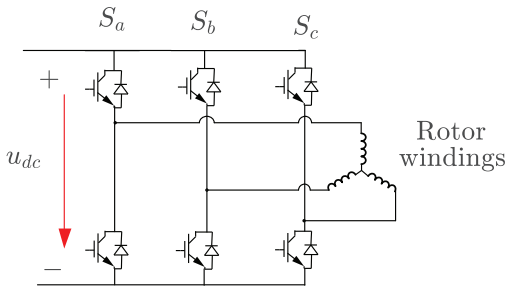

Fig. 3.2: RSC model.

Hence, the RSC can be represented by a switching state vector $\underline{S}[k]$ that comprises each inverter leg switching state:

$$\underline{S}[k] = \frac{2}{3}(S_a[k] + \underline{a} S_b[k] + \underline{a}^2 S_c[k]), \tag{3.19}$$

where $\underline{a} = e^{\frac{2\pi}{3}}$ is the unitary vector.

It is possible to calculate the rotor voltage $\underline{u}_r[k]$, using $\underline{S}[k]$ and the dc-bus voltage level $u_{dc}[k]$ by:

$$\underline{u}_r[k] = \underline{S}[k] u_{dc}[k] \tag{3.20}$$

3.2.1 Forward Euler

By using the Forward Euler discretization method, the time derivative of a quantity x is approximated by:

Therefore, the discrete version of (3.13), through the approximation of its derivative, can be used, resulting in:

$$\mathbf{x}[k+N] = \mathbf{A}_d\mathbf{x}[k+N-1] + \mathbf{B}_d\mathbf{u}[k+N-1] \tag{3.21}$$

with $\mathbf{x}[k+h] = [\underline{\psi}_r^p[k+h]\ \underline{i}_r^p[k+h]]$ being the state vector at instant $k+h$ of predicted rotor flux $\underline{\psi}_r^p[k+h]$ and rotor current $\underline{i}_r^p[k+h]$. $\mathbf{A}_d$ and $\mathbf{B}_d$ are the discrete versions of $\mathbf{A}$ and $\mathbf{B}$, given by:

$$\mathbf{A}_d = \mathbf{I} + T_s\mathbf{A} \tag{3.22}$$

$$\mathbf{B}_d = T_s\mathbf{B} \tag{3.23}$$

The use of the predicted values of both rotor flux and rotor current for instant $k+h$ allows the prediction of torque, h samples ahead $T_{em}^p[k+h]$.

$$T_{em}^p[k+h] = \frac{3}{2}p(i_{dr}^p[k+h]\psi_{qr}^p[k+h] - \psi_{dr}^p[k+h]i_{qr}^p[k+h]) \tag{3.24}$$

The predictions for rotor flux, rotor current and torque, at instant $k+1$, $\underline{i}_r^p[k+1]$, $\underline{\psi}_r^p[k+1]$, $T_{em}^p[k+1]$ are predicted using (3.21) and (3.24), while considering $h=1$. The voltage model used for rotor flux predictions can result in rotor flux drift, which is aggravated at speeds in the vicinity of the DFIG synchronous speed. The ohmic voltage drop in the rotor windings becomes relevant, due to the small voltage applied to the rotor at this speed, bringing large errors and instability in the prediction of the rotor flux. This problem is avoided by the combined use of (3.17) and (3.18) for flux estimation at instant k, while (3.21) is used only for predicting the rotor flux for future time instants.

To properly compensate the control computational delay, all quantities have to be predicted now for instant $k+2$. As we are dealing with a 2-level voltage source inverter, there is the possibility to apply 6 different active vectors and 2 zero vectors, thereby there is a set of 7 distinct predictions, one for each voltage vector. The rotor voltage at instant $k+1$ is predicted considering:

$$\underline{u}_{r_i}[k+1] = \underline{S}_i[k+1]\, u_{dc}[k+1]. \qquad i = 0, 1, 2...7 \tag{3.25}$$

with i representing the index of each possibility of actuation for the inverter. The possible switching states that the inverter can assume are presented in Table 3.1

The resulting predictions for rotor current and rotor flux at instant $k+2$ are given by (3.21) and (3.24), while considering $h=2$. It is assumed that from time instant k to

Table 3.1: Switching states of the inverter

S_a	S_b	S_c	Switching State $\underline{S}_i$
0	0	0	$\underline{S}_0 = 0$
1	0	0	$\underline{S}_1 = \frac{2}{3}$
1	1	0	$\underline{S}_2 = \frac{1}{3} + j\frac{\sqrt{3}}{3}$
0	1	0	$\underline{S}_3 = -\frac{1}{3} + j\frac{\sqrt{3}}{3}$
0	1	1	$\underline{S}_4 = -\frac{2}{3}$
0	0	1	$\underline{S}_5 = -\frac{1}{3} - j\frac{\sqrt{3}}{3}$
1	0	1	$\underline{S}_6 = \frac{1}{3} - j\frac{\sqrt{3}}{3}$
1	1	1	$\underline{S}_7 = 0$

time instant $k+1$ that both the dc-bus voltage and stator voltage are kept constant, *i.e.* $u_{dc}[k+1] = u_{dc}[k]$ and $\underline{u}_s[k+1] = \underline{u}_s[k]$. It is also assumed that the rotor speed does not change considerably over one sampling period, *i.e.* $\hat{\omega}_r[k+1] = \hat{\omega}_r[k]$. Similarly, the two-samples-ahead predictions for torque $T^p_{em_i}[k+2]$, to be evaluated by the cost function, is calculated using (3.24) while considering $h = 2$

3.2.2 Taylor Series Expansion

To approximate the discrete version of (3.13) given by a ZOH model, the Taylor series expansion is used and is given by:

$$x_{k+1} = x_k + \sum_{j=1}^{l} \frac{T_s^j}{j!} \frac{\mathrm{d}^j x}{\mathrm{d}t^{\,j}}\bigg|_{t=kT_s} \tag{3.26}$$

in which l and j are the order and index of the intended expansion, respectively. In the particular case where it is of the first order, *i.e.* $l = 1$, the following equations match the ones given by the forward Euler method. Following a second order expansion, *i.e.* by making $l = 2$, and applying to the continuous system (3.13), one obtains the discrete model of (3.21), but now with:

$$\mathbf{A}_d = \mathbf{I} + T_s\mathbf{A} + \frac{T_s^2}{2}\mathbf{A}^2 \tag{3.27}$$

$$\mathbf{B}_d = T_s\mathbf{B} + \frac{T_s^2}{2}\mathbf{A}\mathbf{B}, \tag{3.28}$$

Again, the predictions of rotor flux, rotor current and torque for instants $k+1$ and $k+2$ are calculated using (3.21) and (3.24), while considering $N = 1$ and $N = 2$, respectively. It is worth mentioning that independently of the chosen discretization method, the use

of a rotor reference frame avoids the determination of the rotor slip angle, and as so the stator frequency estimation is not required for the algorithm to work, contrary to the vector controlled systems used in [6, 19, 28–30, 32].

3.3 Cost Function Design

The predicted variables are compared with their reference values through the use of a cost function, which defines the intended behaviour for the controlled variables. This means that the switching state that minimizes the cost function is the one that guarantees the smallest divergence from the reference values.

The cost function g_i considers the prediction error for torque and rotor flux. The reference value of rotor flux indirectly regulates the frequency on the stator side, while the torque reference adjusts the flow of active power sent by the DFIG to the dc grid.

This function is defined as:

$$g_i = \left(\frac{T_{em}^* - T_{em_i}^p[k+2]}{T_n}\right)^2 + \lambda_\psi \left(\frac{|\underline{\psi}_r|^* - \underline{\psi}_{r_i}^p[k+2]}{\psi_{r_n}}\right)^2, \tag{3.29}$$

where λ_ψ represents a weighting factor that dictates the importance of flux regulation in comparison with torque regulation, and $|\underline{\psi}_r|^*$ is the reference value of the rotor flux space vector amplitude. Both torque and flux errors are normalized using the corresponding rated values, T_n and ψ_{r_n} so that the addition of terms with different units is possible.

This cost function is evaluated for every possible switching state of the inverter and the one that leads to a lower cost value, *i.e.* the control action that has the best reference tracking for the controlled variables, is selected and the corresponding firing pulses of the inverter generated.

$$\underline{S}[k+1] = \arg\min_{i=0\ldots7}(g_i) \tag{3.30}$$

3.4 Rotor Flux Level Optimization

When compared with a classical DFIG system with the stator connected to a fixed frequency ac network, the stator frequency in the DFIG-dc system provides an additional

degree of freedom, which can be exploited to optimize its operation.

To deduce the optimal magnetization current, which minimizes Joule losses in the DFIG, a simplified analytical approach has been used, based on [34]. In that work, the stator frequency is adjusted in order to increase the efficiency of the system at light load, and this change is brought by a proper choice of stator flux level. Neglecting iron losses, the optimal reference magnetizing current $i^*_{m_{pu}}$ in per unit notation can be expressed as a function of the reference q-axis rotor current $\left|i_{qR}\right|^*_{pu}$ (in the equivalent Γ circuit) and of a constant K_2. All quantities with the subscript R are referent to the Γ equivalent circuit, and the pu subscript refers to per-unit quantities.

$$i^*_{m_{pu}} = K_2 * \left|i_{qR}\right|^*_{pu} \tag{3.31}$$

$$K_2 = \sqrt{\frac{\tau + \lambda \left|i_R\right|_{pu}}{\tau + \left|i_R\right|_{pu}}} \tag{3.32}$$

With $\left|i_R\right|_{pu}$ being the rotor current, λ and τ the winding copper losses and semiconductor conduction losses operational parameters, respectively. The following relations apply:

$$i_{m_{pu}} = \frac{\psi_{s_{pu}}}{L_{s_{pu}}} \tag{3.33}$$

$$i_{s_{pu}} = i_{qR_{pu}} = \frac{\left|T_{em}\right|^*_{pu}}{\psi_{s_{pu}}} \tag{3.34}$$

$$\tau = \frac{P_{inv0_{pu}}}{2R_{R_{pu}}} \tag{3.35}$$

$$\lambda = \frac{R_{s_{pu}} + R_{R_{pu}}}{R_{R_{pu}}} \tag{3.36}$$

$$\left|i_R\right|_{pu} = \left|i_r\right|_{pu} \tag{3.37}$$

In (3.31) to (3.37) $\psi_{s_{pu}}$, $i_{s_{pu}}$, R_s and L_s represent the stator flux, stator current, stator resistance and stator self-inductance. R_R is the rotor resistance and P_{inv0} stands for the full-load inverter conduction losses. Elevating (3.31) to the power of 2 and under the assumptions of (3.33) to (3.37), one can define the optimal stator flux $\psi^{*opt}_{s_{pu}}$ as a function of the reference torque $\left|T_{em}\right|^*$ by:

$$\psi^{opt}_{s_{pu}} = K_1 \sqrt{L_{s_{pu}} \left|T_{em}\right|^*_{pu}} \tag{3.38}$$

$$K_1 = \sqrt[4]{\frac{\tau + \lambda \left|i_R\right|_{pu}}{\tau + \left|i_R\right|_{pu}}} \tag{3.39}$$

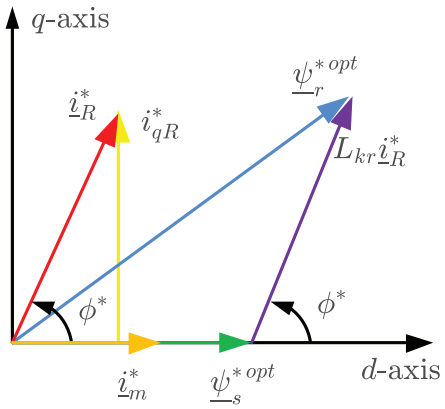

Fig. 3.3: Steady-State phasor diagram for optimized rotor flux determination.

However this value has to be converted into a optimum rotor flux level $\psi_{r_{pu}}^{*opt}$ so that it may be used by the predictive control algorithm used in the present work. Considering the steady-state phasor diagram of the DFIG (Figure 3.3) one obtains:

$$\psi_{r_{pu}}^{*opt} = \sqrt{(\psi_{s_{pu}}^{*opt})^2 + (L_{kr_{pu}}\underline{i}_{R_{pu}}^*)^2 + 2\psi_{s_{pu}}^{*opt} * L_{kr_{pu}} i_{R_{pu}}^* \; cos(\phi^*)} \tag{3.40}$$

L_{kr} in (3.40) is the rotor leakage inductance and ϕ is the angle that the stator flux lags the rotor current. The conversion of real measured values to per-unit value is done by dividing these values by their base values.

$$R_{R_{pu}} = \frac{R_R}{Z_B} = R_R \frac{I_B}{U_B} \tag{3.41}$$

$$\lambda = \frac{R_s + R_R}{R_R} \tag{3.42}$$

$$L_B = \frac{U_B}{I_B \omega_B} \tag{3.43}$$

$$T_B = \frac{S_B \; p}{\omega_B} = \frac{3 U_B I_B \; p}{2\omega_B} \tag{3.44}$$

$$\psi_B = \frac{U_B}{\omega_B} \tag{3.45}$$

$$P_{inv0_{pu}} = \frac{P_{inv0}}{\frac{3}{2} U_B I_B} \tag{3.46}$$

$$\tau = \frac{P_{inv0}}{3 U_B \; I_B \; r_R} = \frac{P_{inv0}}{3 R_r (\frac{L_s}{L_m})^2 I_B^2} \tag{3.47}$$

By replacing the per-unit quantities in (3.38), by their real values defined in (3.41) to (3.47) leads to an optimal stator flux level ψ_s^{opt}, expressed in real values, given by:

$$\psi_s^{opt} = K_1 \sqrt{L_s \, |T_{em}|^*} \sqrt{\frac{2}{3p}} \tag{3.48}$$

$$K_1 = \sqrt[4]{\frac{\frac{P_{inv0}}{3R_R I_B^2} + \lambda\frac{I_R}{I_B}}{\frac{P_{inv0}}{3R_R I_B^2} + \frac{I_R}{I_B}}} \tag{3.49}$$

This optimum stator flux level must be limited to a maximum value $\psi_{s_{max}}$ equal to the machine nominal value as to avoid the saturation of the magnetic circuit. On the other hand, for low-torque values, a minimum value for the stator flux $\psi_{s_{min}}$ must also be defined, as to restrict the maximum operating frequency of the machine $f_{s_{max}}$.

$$\psi_{s_{max}} = \frac{\sqrt{2}U_n}{\sqrt{3}2\pi f_n} \tag{3.50}$$

$$\psi_{s_{min}}^{opt} = \frac{2}{\pi}U_{dc}\frac{1}{2\pi f_{s_{max}}} \tag{3.51}$$

Considering these stator flux restrictions the stator flux value and considering that one can get the optimum value for $\left|i_{qR}\right|^*$, results in:

$$\left|i_{qR}^*\right| = \frac{|T_{em}^*|}{\frac{3}{2}p\psi_s^{*opt}} \tag{3.52}$$

$$i_m^* = K_2\left|i_{qR}^*\right| \tag{3.53}$$

$$\phi^* = atan\frac{\left|i_{qR}^*\right|}{i_m^*} \tag{3.54}$$

$$i_r^* = \sqrt{i_m^{*2} + i_{qR}^{*2}} \tag{3.55}$$

The optimum rotor flux level ψ_r^{*opt} is finally obtained in real values by replacing (3.52) into (3.40), thus obtaining:

$$\psi_r^{*opt} = \psi_{r_{pu}}^{*opt}\frac{L_m}{L_s} = \sqrt{\left(\frac{L_m}{L_s}\psi_s^{opt}\right)^2 + (\sigma L_r\left|i_r\right|)^2 + 2\sigma L_r\sqrt{\left(\psi_s^{opt}\left|i_r\right|\frac{L_m}{L_s}\right)^2 - \left(\frac{2T_{em}^*}{3p}\right)^2}} \tag{3.56}$$

3.5 Overcurrent protection

With the proposed cost function, the rotor currents are not directly controlled, which may lead to high rotor currents during transients. The typical solution to this problem [11] materializes as an extra term that appears in the cost function, assigning a very high value to the cost function to the predictions that exceed the rated current. However, this solution

just tries to discard the predictions that result in overcurrents, but fails in this function if all possibilities result in an overcurrent. Here, the rotor current will be limited by restraining the reference torque value, due to the proportional relationship between torque and rotor current. The algorithm is illustrated in Figure 3.4. The predicted rotor current space vector for instant k+1 is passed through a low-pass filter with a cut-off frequency of 5 Hz, and the the obtained value is subtracted to the maximum rotor current. The resulting error is multiplied by the machine rated torque T_n, and this correction term T_{em_corr} is added to the reference torque T_e^*. This corrected term is the torque reference T_{em}^*, which is used in the cost function.

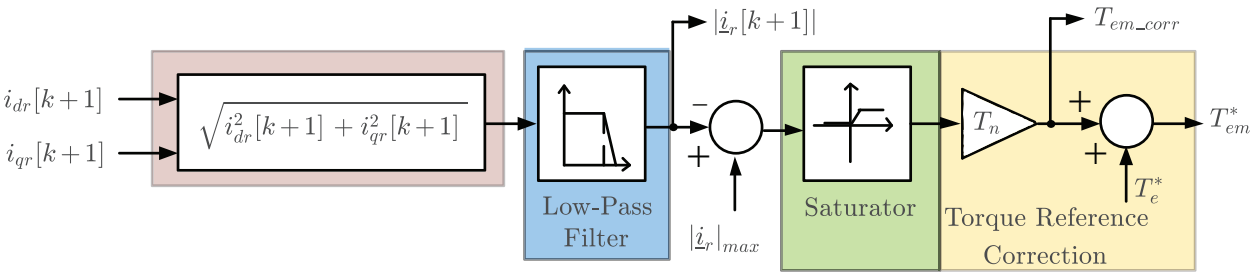

Fig. 3.4: Overcurrent protection algorithm.

Chapter 4

System Simulation

The control strategy presented in the previous chapter was firstly simulated in MATLAB/Simulink in order to evaluate the performance of the drive system and validate its results before the experimental procedure.

An evaluation of the steady-state performance of the DFIG-dc system is made, when it develops rated torque, and when running at 3 different rotor speeds. The tested speeds have to represent the predicted range of operating speeds of the DFIG, which is approximately 33% around its synchronous speed. The system will be evaluated at 1250 rpm, 1520 rpm and 1750 rpm, as these speeds are within this range, and because it also allows to test the operation of the DFIG at a sub-synchronous, synchronous and super-synchronous speed, respectively. The use of different sampling times will also be tested, due to the fact that the commonly used DSPs might not be able to run the algorithm in the pre-established sampling time. The dynamic performance of the drive is also tested when the DFIG is subjected to a torque step, torque ramp and to a speed ramp variation. Lastly, a sensitivity analysis to the rotor winding resistance value and leakage inductance value is made, in order to assess the controller robustness to machine parameters mismatch.

4.1 Simulation Model

The model used in the simulation and a brief description of the same are shown in Appendix A, while the machine parameters are presented in Appendix B (Table B.1), which also corresponds to the DFIG available in the laboratory.

Throughout the presentation of the simulation results, discrete models for both the inverter and the machine were used, and the sampling period was set as 50 μs. The value of the weighting factor λ_ψ for rotor flux regulation was set to 2, by a trial and error process. The varying magnetizing inductance and magnetic saturation of the machine were also considered in the control system (see Appendix A). Additionally, the full-load inverter conduction losses P_{inv0}, needed for optimum rotor flux generation, were assumed to be 100 W approximately, as it is difficult to discriminate switching and conduction losses.

4.2 Obtained Results

4.2.1 Steady-State Operation

For the steady-state operation analysis, a reference electromagnetic torque of T^*_{em}= -12.5 N.m was considered. The (-) sign is due to the fact that motor convention was used. The simulation results obtained in steady-state for the tested speeds are shown in Figs. 4.1, 4.3 and 4.5, respectively. The estimated torque $\hat{T}_{em}$, its reference value T^*_{em}, rotor and stator flux space vector amplitudes, $\hat{\psi}_r$ and $\hat{\psi}_s$, and rotor and stator currents in abc frame are shown. Additionally, the active power P_s and reactive power Q_s across the stator are presented, along with the dc-bus voltage u_{dc}.

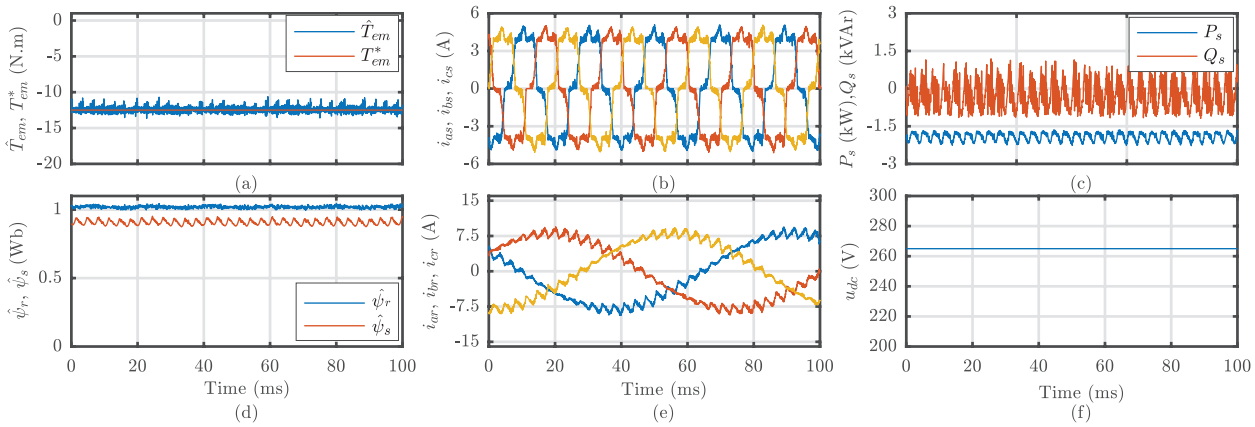

Fig. 4.1: Simulation results for the steady-state operation of the DFIG at 1250 rpm: (a) electromagnetic and reference torque; (b) stator currents; (c) stator active and reactive power; (d) rotor and stator flux; (e) rotor currents; (f) dc-bus voltage.

Figure 4.1 shows that, at 1250 rpm, the electromagnetic torque is able to follow closely its constant reference value. It does not appear to exhibit the torque oscillations described

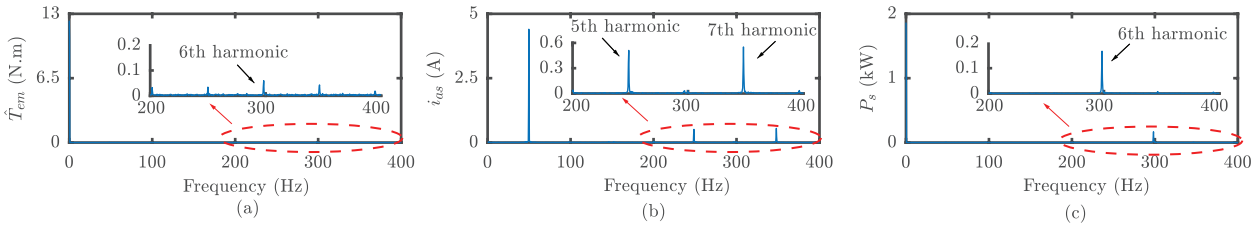

Fig. 4.2: Spectra of steady-state operation at 1250 rpm taken from : (a) electromagnetic torque; (b) stator current; (c) stator power.

in [5, 16, 17, 20], showing only a negligible high-frequency ripple. The rotor flux amplitude is kept constant, while the stator flux presents a pulsating nature, which is expected, due to the uncontrolled rectifier connected to the stator. The operation of the rectifier is also responsible for the visible distortions present in the stator current waveforms. Sinusoidal operation of rotor currents is achieved, with them only manifesting a small high-frequency ripple. As stator active power is delivered by the stator windings, to the rectifier, with an average value of approximately 2 kW. However both stator powers exhibit a pulsating nature, confirming the reports in [44] that constant torque and stator power can only be simultaneously achieved through the sinusoidal grid operation of the DFIG, which is not possible due to the presence of the diode rectifier. This can be attested in Figure 4.2, where it is visible the presence of the 6th harmonic of the stator active power. The diode operation can also be confirmed by the noticeable presence of the 5th and 7th stator current harmonics in its spectrum. However, the presence of the 6th harmonic component for torque confirms itself as practically null, being only visible in a very magnified version of its spectrum. This confirms that the system is operating without the low-frequency torque oscillations reported in [5, 16, 17, 20]

The simulated results for 1750 rpm are similar (Figure 4.3), even though both torque and rotor flux waveforms appear to present slightly less ripple. There are no noticeable changes, when comparing the other waveforms. Figure 4.4 reveals that the operation of the DFIG at a super-synchronous speed does not change the spectral content of torque, stator power and stator current.

Figure 4.5 shows that at synchronous speed much of the behaviour of the previously shown variables is similar, particularly for stator current and its active and reactive powers. Although torque is still maintained constant near its reference value, it appears more distorted than in the previous two cases. This can also be extended to both rotor and stator

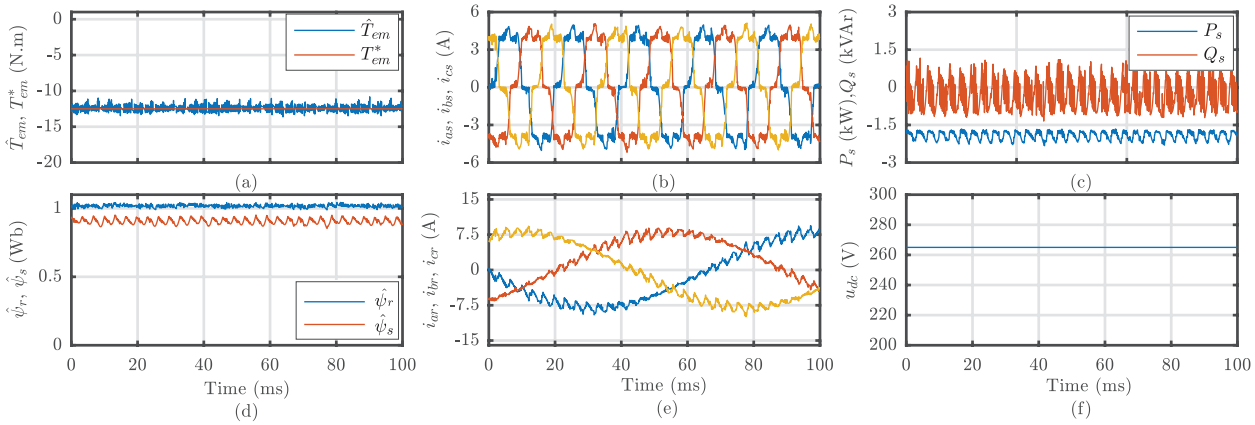

Fig. 4.3: Simulation results for the steady-state operation of the DFIG at 1750 rpm: (a) electromagnetic and reference torque; (b) stator currents; (c) stator active and reactive power; (d) rotor and stator flux; (e) rotor currents; (f) dc-bus voltage.

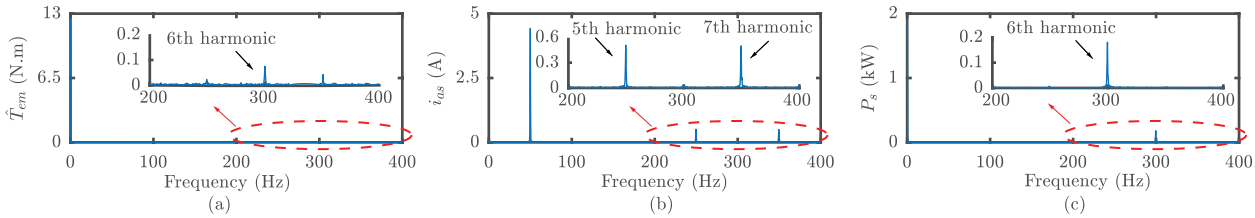

Fig. 4.4: Spectra of steady-state operation at 1750 rpm taken from : (a) electromagnetic torque; (b) stator current; (c) stator power.

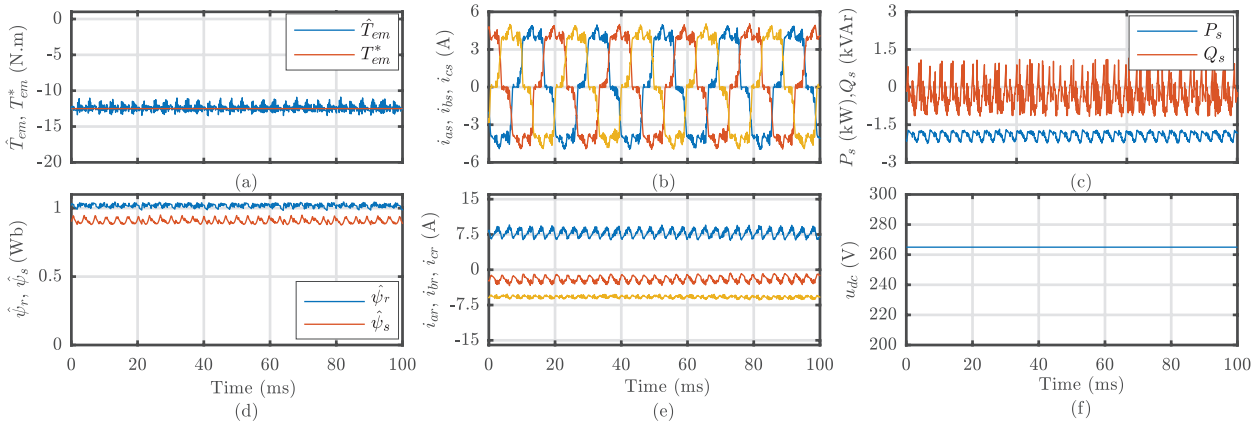

Fig. 4.5: Simulation results for the steady-state operation of the DFIG at 1520 rpm (synchronous speed): (a) electromagnetic and reference torque; (b) stator currents; (c) stator active and reactive power; (d) rotor and stator flux; (e) rotor currents; (f) dc-bus voltage.

flux. The most evident difference on operation of the DFIG is that the rotor currents become dc quantities at synchronous speed, due to the fact that they are proportional to the slip of the machine. It is also shown in Figure 4.6 that the speed of operation of the DFIG does not influence the amplitude of the 5th and 7th stator current harmonics, neither the amplitude

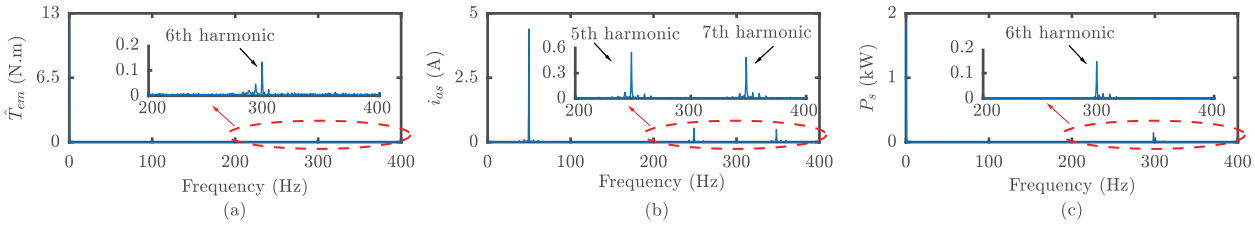

Fig. 4.6: Spectra of steady-state operation at 1520 rpm taken from : (a) electromagnetic torque; (b) stator current; (c) stator power.

of the 6th harmonic of stator power. However, the torque spectrum exhibits a 6th harmonic component with a larger expression than in the previous two cases, reaching almost twice its original amplitude.

The total waveform distortion (TWD) [45] is used as a metric to weight all the harmonic content of a wave, being defined as:

$$TWD_x(\%) = \frac{\sqrt{x_{rms}^2 - x_1^2}}{x_1} \times 100\% \tag{4.1}$$

with x_{rms} being the rms value for the evaluated variable x and x_1 its fundamental component amplitude. The errors of prediction of a variable E_x can be defined as the root mean square value of the difference between the predicted values two samples ahead ($x^p[k+2]$) and its real value. N_s represents the number of samples used in the calculations[1]:

$$E_x = \sqrt{\frac{1}{N_s}\sum_{k=0}^{N_s}(x^p[k+2] - x[k+2])^2} \tag{4.2}$$

In Table 4.1 the values of TWD for torque ($TWD_{T_{em}}$) and rotor flux (TWD_{ψ_r}) are shown. Also present are the prediction errors for these variables, given by $E_{T_{em}}$ and E_{ψ_r}, as well as the prediction error for rotor current E_{i_r}. The amplitude of the 6th harmonic for torque T_{em6} is also shown. Table 4.1 confirms the reported differences for the 3 operating speeds. Both torque and rotor flux present themselves with less distortion at high speeds, as evidenced by the values of $TWD_{T_{em}}$ and TWD_{ψ_r}. It also shows that the errors of prediction for rotor current and torque reach their lowest values at synchronous speed. However, it confirms that at this speed the 6th harmonic component for torque T_{em6} reaches its highest value, being this considered highly undesirable.

[1]For the calculations, 3 seconds of signals were considered, sampled at a rate of $\frac{1}{50\times10^{-6}}$ Hz, which corresponds to 60 000 samples.

Table 4.1: Total waveform distortion and prediction errors of the DFIG-dc system at the tested speeds and with a sampling time of 50 μs.

n_r (rpm)	$TWD_{T_{em}}$ (%)	T_{em6} (N.m)	$E_{T_{em}}$ (N.m)	TWD_{ψ_r} (%)	E_{ψ_r} (mWb)	E_{i_r} (A)
1250	0.99	0.06	0.33	1.07	0.89	0.27
1520	0.95	0.11	0.22	0.83	0.98	0.22
1750	0.83	0.05	0.29	0.51	0.98	0.28

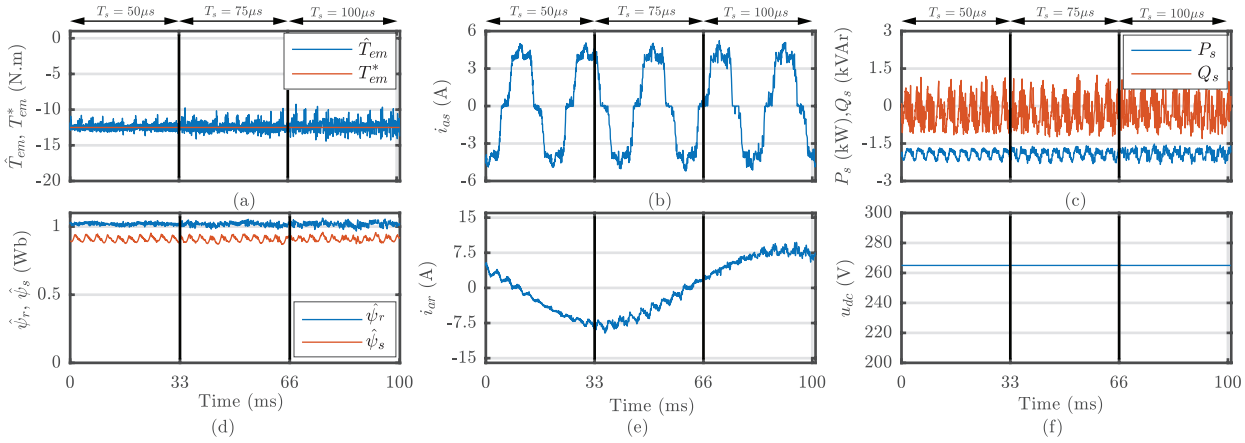

Fig. 4.7: Simulation results for the steady-state operation of the DFIG at 1250 rpm and sampling times of 50, 75 and 100 μs: (a) electromagnetic and reference torque; (b) stator currents; (c) stator active and reactive power; (d) rotor and stator flux; (e) rotor currents; (f) dc-bus voltage.

As the DSPs computational power is limited when compared to the used control platform, it may need longer sampling times so that the execution of the algorithm is possible. Additionally, the use of higher sampling time is related to fewer commutation losses for the inverter bridge, due to the fact that these commutations can only occur at times multiple of the sampling time T_s. As such, a comparison between the use of different sampling times is provided.

The DFIG is made to rotate at 1250 rpm, while developing constant torque of -12.5 N.m. Figure 4.7 shows its steady-state operation with sampling times of 50 μs, 75 μs and 100 μs in intervals of 33 ms. With the increase of the sampling time T_s, the system exhibits bigger distortions for all previously shown variables, this being particularly notorious for a sampling time of 100 μs. This increased distortion appears to affect particularly torque and the rotor flux waveforms, as each increment of 25 μs appears to contribute significantly to an increased ripple. It can be seen in Figure 4.8 that the switching frequency is variable and has a spread spectrum on the rotor voltage. However the use of larger sampling times contributes to make the spectrum more concentrated near the low-frequencies. It also proves that the

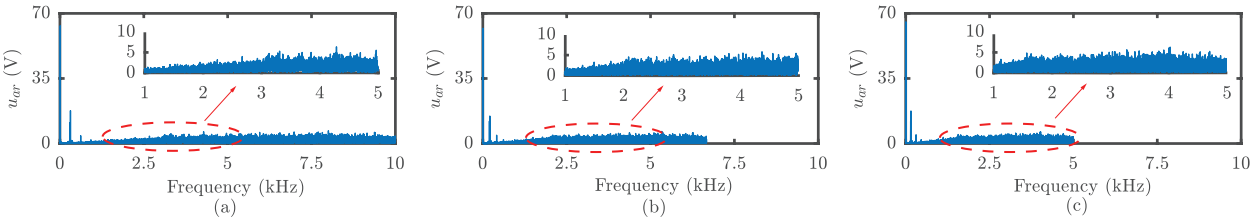

Fig. 4.8: Spectra of rotor voltage at 1250 rpm and at a sampling time of: (a) 50 μs; (b) 75 μs; (c) 100 μs.

maximum switching frequency of the inverter is limited to half the sampling frequency.

Table 4.2 proves that a larger sampling time, brings greater distortion for torque and rotor flux, resulting in bigger values for $TWD_{T_{em}}$ and TWD_{ψ_r}. The increase in $TWD_{T_{em}}$ is also related to a larger amplitude for the 6th harmonic component of torque T_{em6}. Notwithstanding, the system still demonstrates very low torque oscillations at this frequency. The accuracy of predictions decreases, evidenced by an increased error in $E_{T_{em}}$, E_{ψ_r} to over twice their original values. However the rotor current appears to be the least affected variable by the increased sampling time, having the smallest increase for its predictions error E_{i_r}.

Table 4.2: Total waveform distortion and prediction errors of the DFIG-dc system at 1250 rpm and with sampling rates of 50, 75 and 100 μs.

$T_s(\mu s)$	$TWD_{T_{em}}(\%)$	T_{em6}(N.m)	$E_{T_{em}}$(N.m)	$TWD_{\psi_r}(\%)$	E_{ψ_r} (mWb)	E_{i_r} (A)
50	0.99	0.06	0.33	1.07	0.89	0.27
75	1.64	0.12	0.53	1.18	1.40	0.40
100	2.13	0.17	0.75	2.07	2	0.53

4.2.2 Dynamic Operation

The dynamic operation of the drive was tested by three different means: at first the rotor speed was held constant at synchronism and the system was subjected to a torque ramp variation. Afterwards, the response of the DFIG was evaluated under a load torque step of -12.5 N.m. while running at a constant speed of 1250 rpm. Then it was subjected to a constant load torque of -12.5 N.m and the rotor of the DFIG was accelerated from 1250 rpm to 1750 rpm, in order to cover its operation in sub-synchronous and super-synchronous modes.

4.2.2.1 Torque Ramp Response

The system was subjected to a torque ramp variation spanning from -3 N.m to -12.5 N.m, while rotating at synchronous speed, to demonstrate it can operate correctly at different load levels. It is possible to see in Figure 4.9 that the flux level is lower for low torque levels while

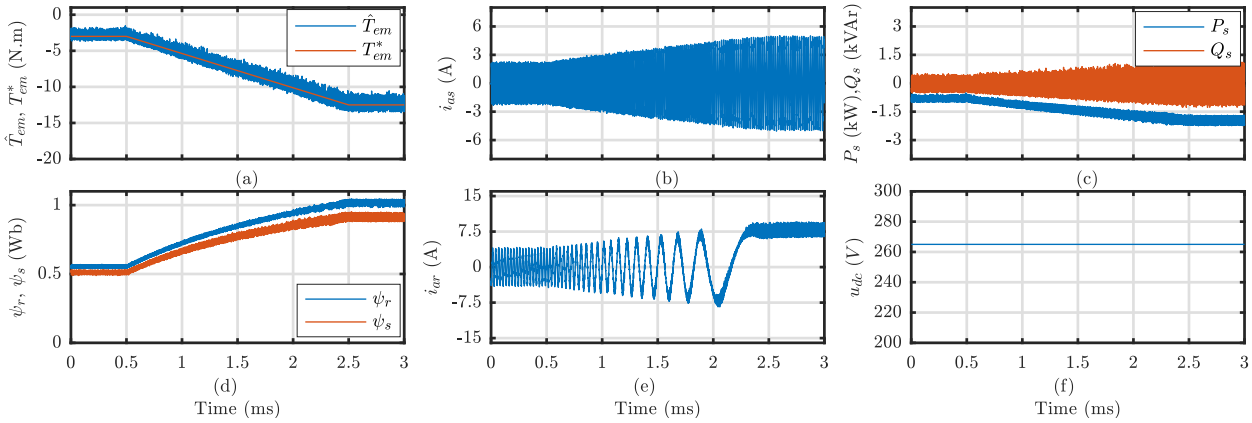

Fig. 4.9: Simulation results for the torque ramp response of the DFIG at 1520 rpm, : (a) electromagnetic and reference torque; (b) stator currents; (c) stator active and reactive power; (d) rotor and stator flux; (e) rotor current; (f) dc-bus voltage.

it increases up to the rated flux for higher load values. The stator frequency is also variable, being higher for low-load levels as the result of a low stator flux level and fixed dc-bus voltage, It also possible to confirm that the developed electromagnetic torque regulates the flow of active power delivered by the stator. With the increase of active power delivered by the stator, there is also an increase in the stator current amplitude. The system demonstrates the ability to operate in the full load torque range.

4.2.2.2 Torque Step Response

The DFIG, originally at no-load, was subjected to a torque step of $T^*_{em} = -12.5$ N.m while running at 1250 rpm. Figure 4.10 shows that the flux level defined for the no-load operation was set to 0.4 Wb. Since the magnetization of the machine is provided by the RSC, the rotor currents are not zero, even at this condition. Additionally, there is no active or reactive power across the stator windings, which can be attested to an also null stator current. As a consequence of the torque step, the control algorithm adjusts the amplitude of the rotor flux, in order to develop the required electromagnetic torque. The proposed FCS-MPC algorithm show a fast response under a torque step change, with the system developing

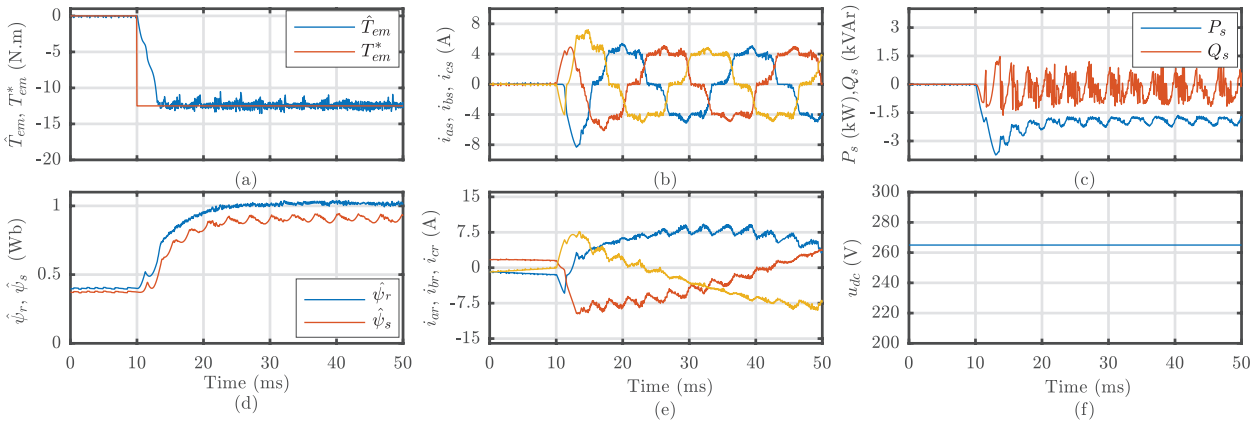

Fig. 4.10: Simulation results for the torque step response of the DFIG at 1250 rpm, : (a) electromagnetic and reference torque; (b) stator currents; (c) stator active and reactive power; (d) rotor and stator flux; (e) rotor currents; (f) dc-bus voltage.

the required torque in approximately 3 ms. As the DFIG starts developing torque, it also starts delivering active power across the stator, settling at 2 kW. Operation with sinusoidal rotor currents is also achieved, because the DFIG was not running at synchronous speed.

4.2.2.3 Speed Ramp Response

The system was subjected to a speed ramp with a slope of 250 rpm/s, and a constant reference torque of -12.5 N.m., as to ensure that the system is able to operate at all speeds. Its response is depicted in Figure 4.11. It shows that, as the machine approaches synchronous

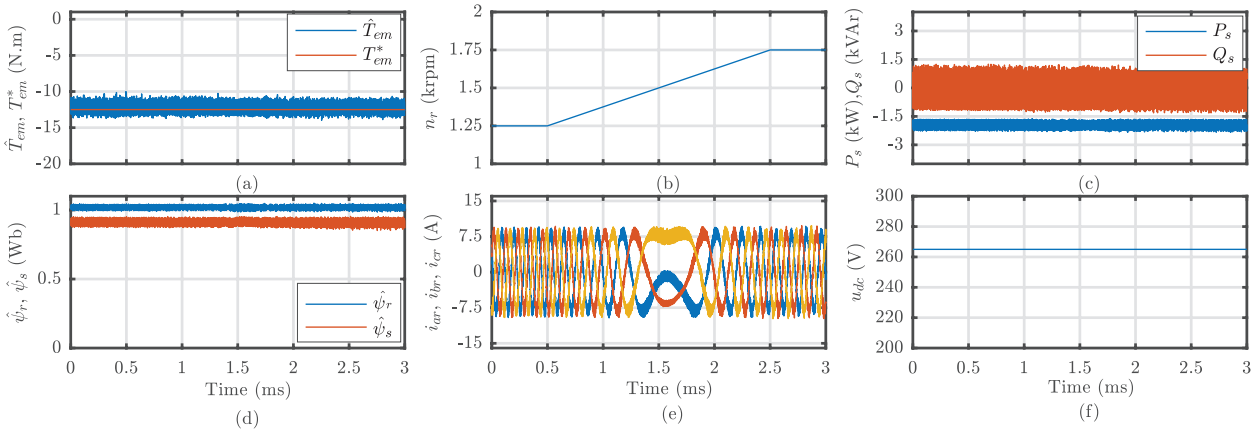

Fig. 4.11: Simulation results for the speed ramp response of the DFIG: (a) electromagnetic and reference torque; (b) rotor speed; (c) stator active and reactive power; (d) rotor and stator flux; (e) rotor currents; (f) dc-bus voltage

speed, the frequency of rotor currents decreases until it reaches zero. At this speed the applied

rotor voltage is minimum. However, as the machine is driven into a super-synchronous speed the rotor currents phase sequence is reversed and its frequency rises. It is also possible to confirm that the stator active and reactive powers are independent of rotor speed, as they also remain constant throughout the speed ramp.

4.2.3 Sensitivity Analysis

The actual values of the parameters used in the mathematical model normally are not known precisely, being prone to some uncertainty, and introduce error in the predictions made. The quantification of the effects of such errors, allows to assess the model of the DFIG range of validity. As such, a sensitivity analysis to the machine rotor parameters is made, where its values are known to change due to different operating conditions, frequency and temperature. The leakage inductance of the rotor L'_{lr} is normally assumed as constant, due to constant flux operation of the machine at steady-state. However, its estimation assumes an equal sharing of the short-circuit inductance between the stator and rotor leakage inductances, which can be susceptible to error. Similarly, the rotor winding resistance R'_r experiences variations due to windings temperature variation. All the results were taken at a rotor speed of 1250 rpm, and both the under-estimation and over-estimation of 30% of the evaluated parameters were considered, in intervals of 33ms.

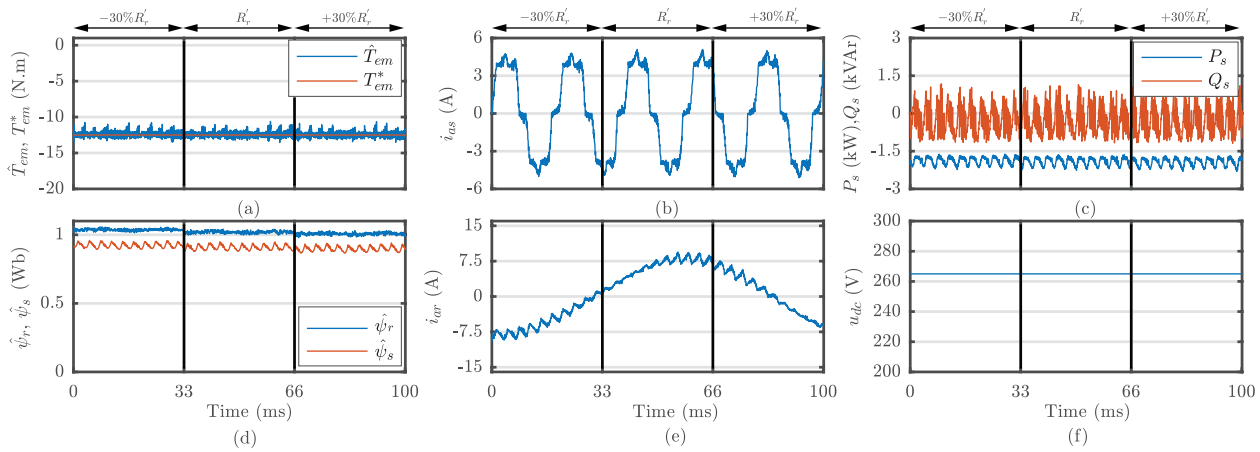

Fig. 4.12: Simulation results from the ±30 % rotor resistance variation in the control system: (a) electromagnetic and reference torque; (b) stator currents; (c) stator active and reactive power; (d) rotor and stator flux; (e) rotor current; (f) dc-bus voltage.

Figure 4.12 shows the system response when the controller was subjected to variation on the values of R'_r. The system presents itself as robust towards this parameter mismatch,

with only the rotor flux waveform exhibiting slightly more ripple. It also shows that the rotor flux, and consequently the stator flux, have decreasing amplitudes, with the increase of rotor resistance.

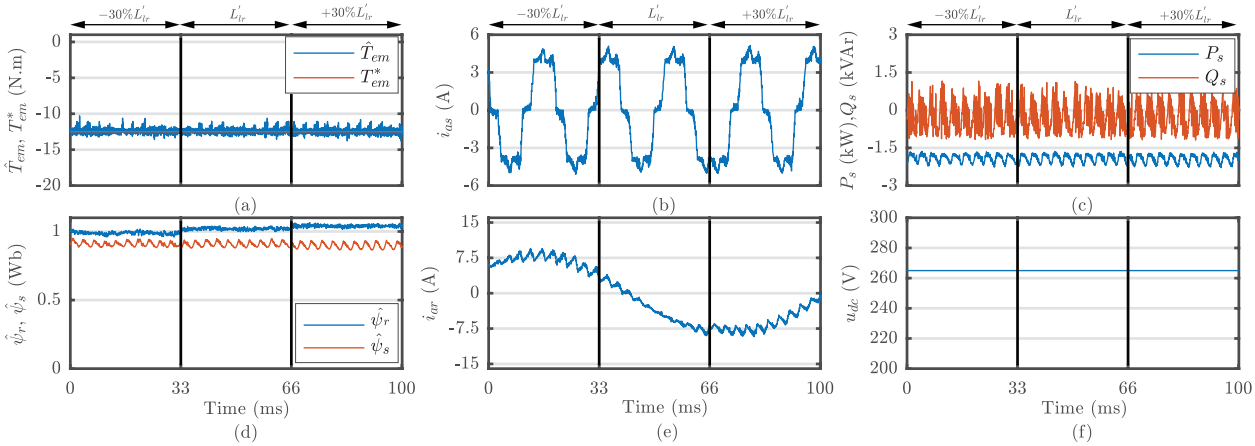

Fig. 4.13: Simulation results from the ±30 % rotor leakage inductance variation in the control system: (a) electromagnetic and reference torque; (b) stator currents; (c) stator active and reactive power; (d) rotor and stator flux; (e) rotor current; (f) dc-bus voltage.

Figure 4.13 shows the same variables, but when the system experiences a mismatch in L'_{lr}. The results are very similar when compared to the previous evaluation, with the only difference being in both rotor and stator flux amplitudes, which increase with the assignment of higher values for L'_{lr}.

It is shown in Table 4.3 that rotor parameter variations do not contribute significantly to an increased torque distortion, as evidenced by an almost constant $TWD_{T_{em}}$ for all tested variations. The amplitude of the 6th harmonic component also appears to be practically unaffected by rotor parameter variations, and the errors of prediction of this variable are confined to an increase of 10%, but only in case of L'_{lr} under-rating. Rotor flux appears to be particularly affected by variations in L'_{lr} with the system having two to three times more error for its predictions. However, the system only exhibits the highest TWD_{ψ_r} for this parameter under-value. The error of prediction for rotor current also appears to be robust against rotor parameter variations, with only the under-estimation of L'_{lr} affecting this error.

Table 4.3: Numeric results for simulated sensitivity analysis of the FCS-MPC algorithm

	$TWD_{T_{em}}(\%)$	T_{em6}(N.m)	$E_{T_{em}}$(N.m)	$TWD_{\psi_r}(\%)$	E_{ψ_r} (mWb)	E_{i_r} (A)
$R_r^{'}$ & $L_{lr}^{'}$	0.99	0.06	0.33	1.07	0.89	0.27
$-30\%R_r^{'}$	1.01	0.07	0.33	1.04	0.69	0.27
$+30\%R_r^{'}$	1.03	0.08	0.32	0.63	1.40	0.27
$-30\%L_{lr}^{'}$	0.97	0.08	0.36	1.30	2.00	0.41
$+30\%L_{lr}^{'}$	1.02	0.06	0.34	1.04	2.70	0.20

Chapter 5

Experimental Validation

The present chapter seeks to validate the simulation results in a laboratory test rig. The conducted tests are similar to the ones described in Chapter 4, but with the additional comparison if the steady-state and dynamic performance of the drive system, when both the forward Euler and Taylor series expansion discretization methods are used. The influence of different sampling times on the different discretization techniques is also analysed. Lastly, this comparison is extended to the sensitivity analysis made on the controller, allowing to prove if different discretization techniques can influence the robustness of the controller towards rotor parameters mismatch.

5.1 Test Rig

Figure 5.1 illustrates the test rig used in the experimental tests. The DFIG parameters are equal to the ones used in the previous chapter and listed in Appendix B (Table B.1) Since the stator and rotor windings of the DFIG have a different number of turns, a step-down autotransformer with a transformation ratio of $\sqrt{3}$ is connected between the stator windings and the three-phase diode rectifier. This diode bridge feeds both the 265 V dc bus and the two-level VSI used to control the DFIG. At the dc-bus there is also a capacitor bank C_{dc} with a capacitance of 3400 μF, and is also connected to a 35 Ω resistive load R_L, to dissipate the generated power. Between the inverter and the rotor windings, an inductive filter L_f was connected to mitigate the effects of high voltage variations on the rotor windings insulation system. The rotor speed of the DFIG is imposed by a 7.5 kW squirrel-cage induction motor

fed by an separate industrial VSD.

Through the use of voltage and current sensors, the measurement circuits measure the currents that flow through the rotor and stator windings, as well as the voltages applied to them. They also measure the dc-bus voltage level. The *dSPACE* control platform also receives a signal from a 1024 pulses incremental encoder, so it knows the rotor angular position.

The link between the control algorithm, built in MATLAB/Simulink, and the *dSPACE* platform is made through the *Real-Time Interface* Simulink toolbox. The model used was based on the one described in chapter 4.

Using *ControlDesk*, a control panel was built, enabling real time interaction between the user and the control system. In this panel, the user can define a reference torque, adjust current protection limits and change the weighting factor of the controlled variables. It also allows the visualization in real-time and/or capture of internal variables of the control software algorithm.

The torque sensor RWT321-EC-K from *TorqSens* was coupled between the DFIG and the auxiliary machine, in order to measure the developed mechanical torque and speed. This sensor was connected to the $dSPACE$ so that an estimation of the mechanical input power is possible. This will also allow to estimate the machine's efficiency of operation. Additionally the Yokogawa WT3000 power analyser was also connected for monitoring purposes.

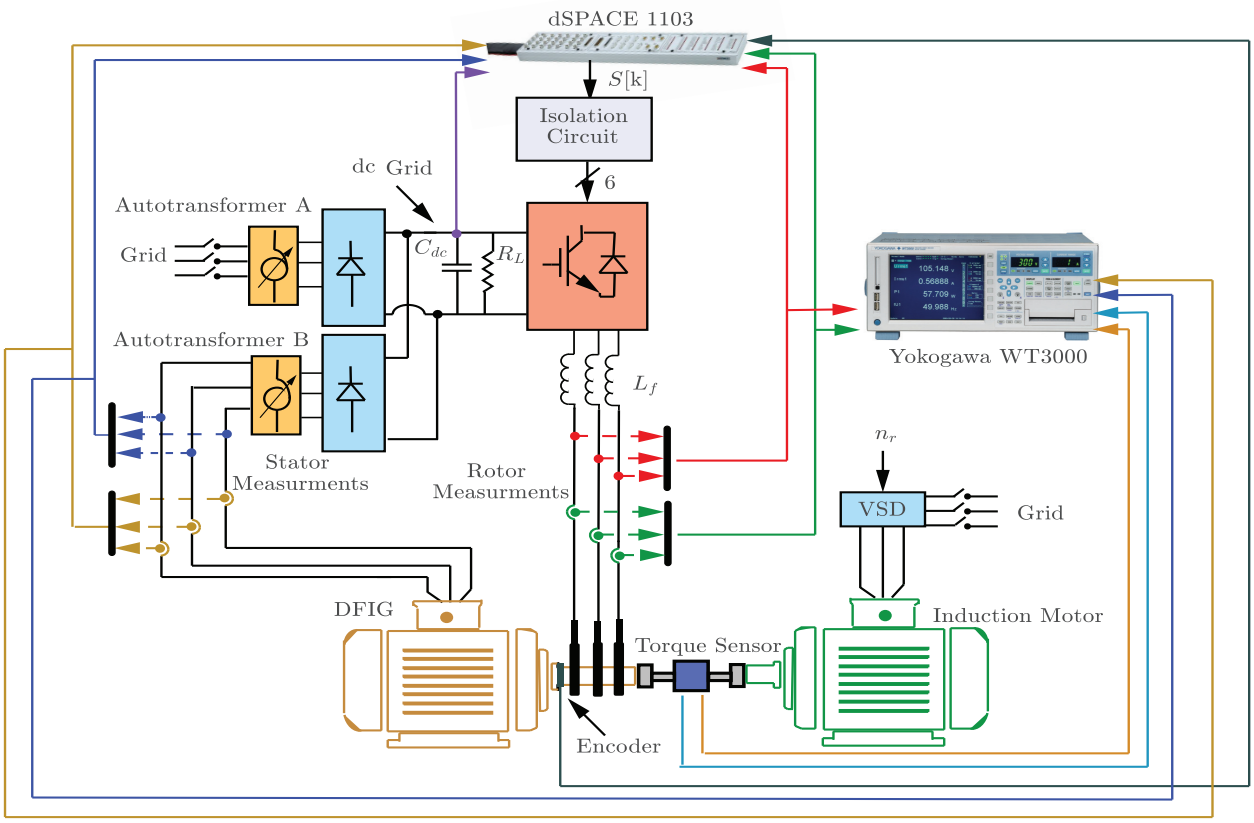

Fig. 5.1: Drive components illustration.

5.2 Experimental Results

5.2.1 Steady-State Operation

Similarly to the previous chapter, the steady-state performance of the DFIG was evaluated while developing a constant torque of -12.5 N.m, at speeds of 1250, 1550 and 1750 rpm. A comparison between the use of forward Euler (FE) and Taylor series expansion (TSE) discretization methods is provided.

Figure 5.2 shows the results for the steady-state operation of the DFIG at 1250 rpm. Both the use of FE and TSE discretization methods were evaluated in intervals of 50 ms. Represented are the estimated electromagnetic torque $\hat{T}_{em}$ and reference torque T^*_{em}, the estimated rotor and stator flux space vector amplitudes $\hat{\psi}_r$, $\hat{\psi}_s$, along with the respective currents (i_{abcr}, i_{abcs}) in the natural reference frame. Also depicted are the stator active and reactive powers P_s, Q_s as well as the dc-bus voltage level u_{dc}.

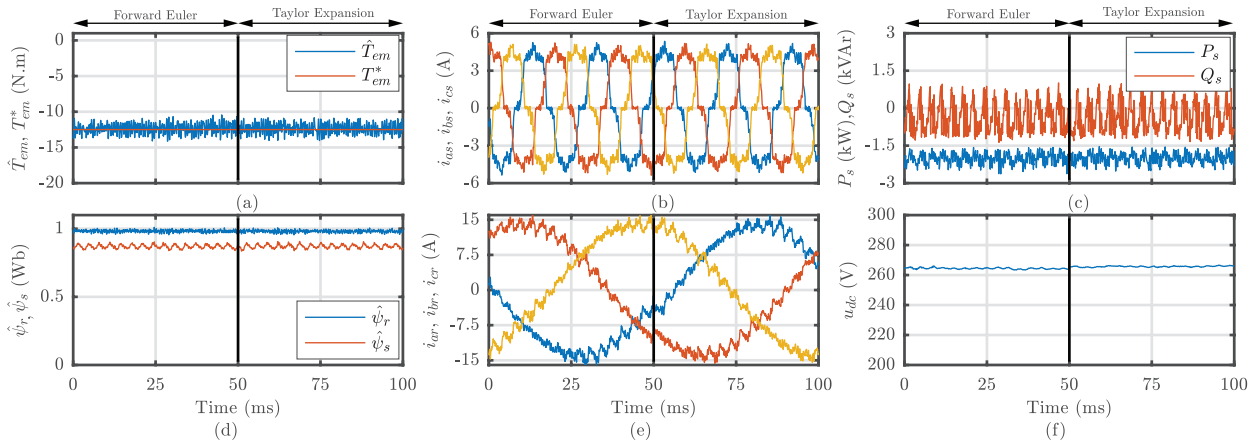

Fig. 5.2: Results for the steady-state operation of the DFIG at 1250 rpm: (a) electromagnetic and reference torque; (b) stator currents; (c) stator active and reactive power; (d) rotor and stator flux; (e) rotor currents; (f) dc-bus voltage.

As in the simulation, this system is able to follow the reference torque, appearing absent from the low-frequency oscillations that characterize most control systems applied to this drive system. The high-frequency ripple present in the torque waveform, although still negligible, is more pronounced than in the simulation, due to the open slots and asymmetries present in the machine. This also contributes to a more distorted rotor and stator flux waveforms, but nevertheless, the rotor flux amplitude is kept constant and the stator flux exhibits the expected pulsating nature. The distortion present in the stator current waveforms is justified by the operation of the diode rectifier. Although the DFIG is able to operate with sinusoidal rotor currents, the presence of low-frequency harmonic oscillations in the stator powers is evident, confirming that constant torque and constant stator power are not possible with this particular topology. It can also be seen that the average active power delivered by the stator windings is approximately 2 kW. Additionally, the use of different discretization methods brought no apparent change to the shown waveforms.

The spectrum of the electromagnetic torque waveform (Figure 5.3) confirms the practically non-existence of the low-frequency oscillations that characterize this system when under field orientation control. Although this harmonic component reaches a higher value than in the simulation, again it can only be seen in the magnified version of the torque spectrum. The oscillations in stator power are also confirmed by the presence of a larger 6th harmonic component in its spectrum. The distortion present in the stator current is again due to the larger amplitudes of the 5th and 7th harmonic components, brought by the operation of the diode rectifier. The use of different discretization methods does not change

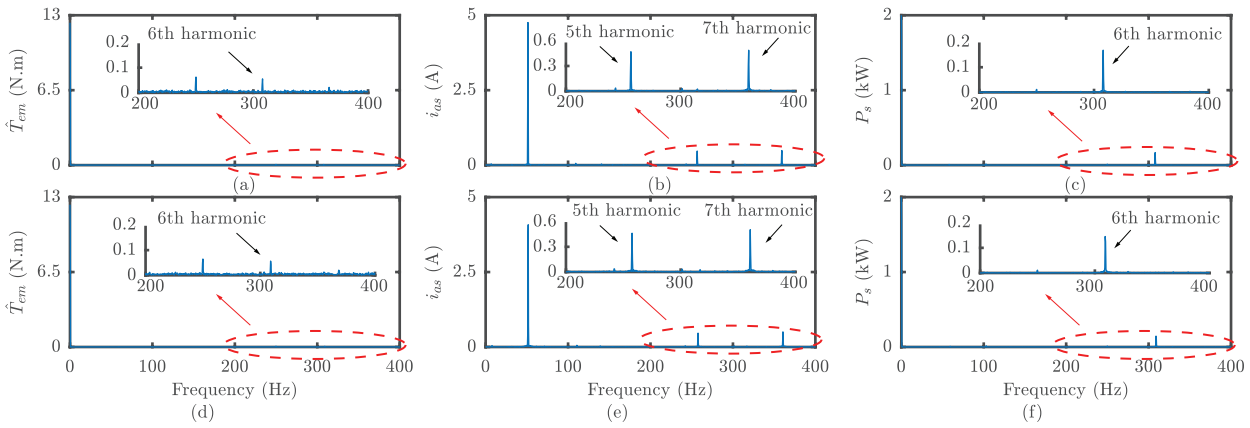

Fig. 5.3: Spectra for the steady-state operation at 1250 rpm taken from: (a) electromagnetic torque using FE; (b) stator current using FE; (c) stator active power using FE; (d) electromagnetic torque using TSE; (e) stator current using TSE; (c) stator active power using TSE.

the low-frequency spectral content of the electromagnetic torque, stator power and stator currents, while operating at sub-synchronous speeds.

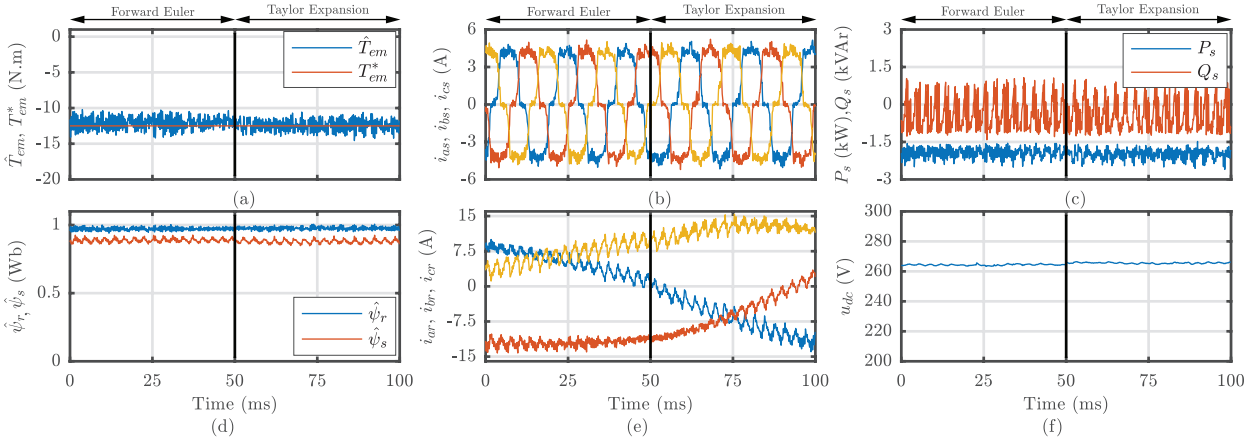

Fig. 5.4: Results for the steady-state operation of the DFIG at 1750 rpm : (a) electromagnetic and reference torque; (b) stator currents; (c) stator active and reactive power; (d) rotor and stator flux; (e) rotor currents; (f) dc-bus voltage.

The results taken at 1750 rpm (Figure 5.4) appear very similar to the previous case, with the major difference being in the rotor currents, which exhibit a lower frequency, implying that the machine is at a slightly different point of operation. Additionally, the estimated electromagnetic torque appears with more high-frequency ripple, than in the previous operating speed. The stator power waveform also appears more distorted than in the sub-synchronous operation of the DFIG. The depicted waveforms do not present any significant change when different discretization methods are used.

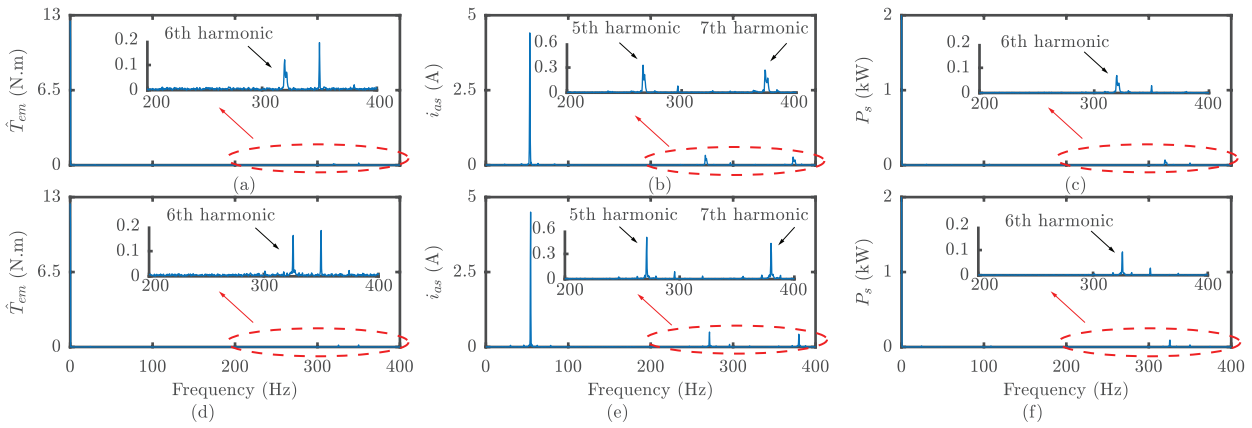

Fig. 5.5: Spectra for the steady-state operation at 1750 rpm taken from: (a) electromagnetic torque using FE; (b) stator current using FE; (c) stator active power using FE; (d) electromagnetic torque using TSE; (e) stator current using TSE; (c) stator active power using TSE.

The analysis of the spectra taken at 1750 rpm (Figure 5.5) indicates that the spectral content of torque increases with the operating speed of the DFIG, as it shows a larger 6th harmonic amplitude than in the previous case. Notwithstanding, it still achieves a low amplitude for this frequency component. There is also a decrease in the 6th harmonic for stator power, when compared with the previous case. The spectral content of stator currents remains unchanged at this operating speed. When comparing both discretization methods, the use of FE appears to lead to a lower spectral content for all shown waveforms.

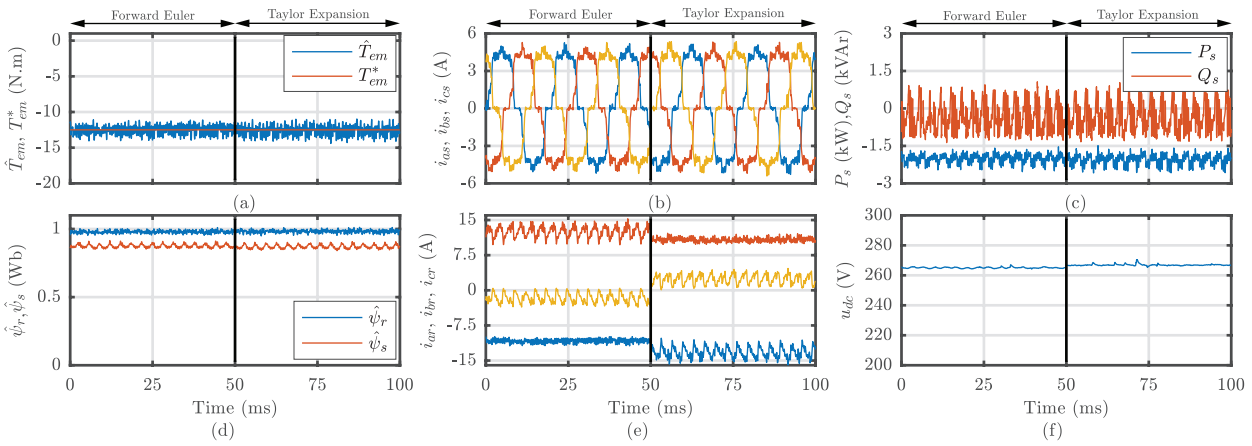

Fig. 5.6: Results for the steady-state operation of the DFIG at 1550 rpm: (a) electromagnetic and reference torque; (b) stator currents; (c) stator active and reactive power; (d) rotor and stator flux; (e) rotor currents; (f) dc-bus voltage.

At synchronous speed (Figure 5.6), the behaviour of the system is similar for all shown variables, except for the rotor currents that become dc quantities. There is also a visible increase in stator power waveform distortion at this speed. The only difference that the use

of the TSE brought was that the machine operates at a different point making the rotor currents appear with slightly different values.

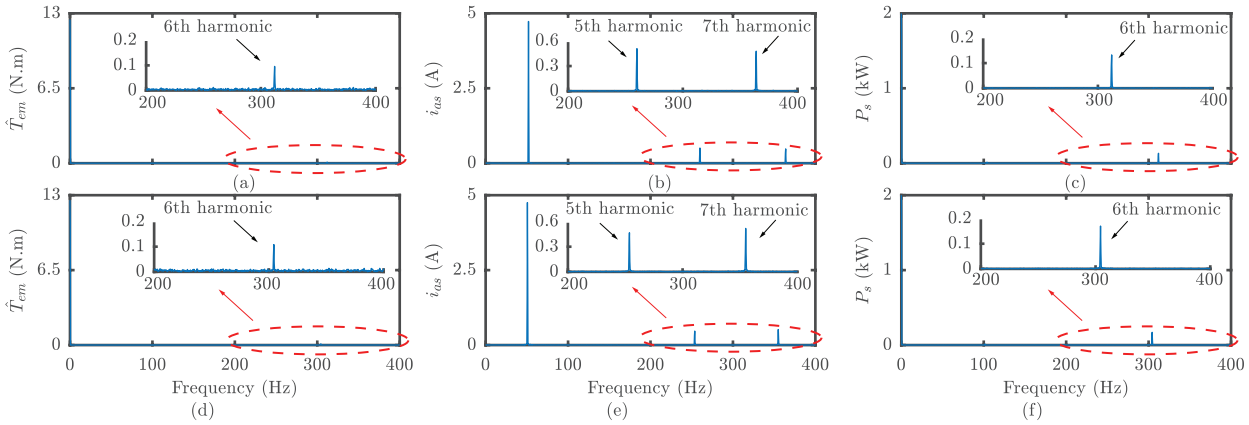

Fig. 5.7: Spectra for the steady-state operation at 1550 rpm taken from: (a) electromagnetic torque using FE; (b) stator current using FE; (c) stator active power using FE; (d) electromagnetic torque using TSE; (e) stator current using TSE; (c) stator active power using TSE

The spectra taken at synchronous speed (Figure 5.7) confirm that for this particular point of operation the low-frequency torque oscillations still retain a very low value, although with a slight increase. Also increased is the 6th harmonic component for stator power. However, the amplitude of the 5th and 7th harmonic components of the stator current, seems to be unaffected by the speed of operation of the DFIG. The use of the TSE at synchronous speed brings an increase of the 6th harmonic of stator power, but brings no change to the spectral content of torque and stator current waveforms.

Table 5.1: Total waveform distortion and prediction errors of the steady-state operation of the DFIG, using both discretization techniques

n_r(rpm)	Discretization	$TWD_{T_{em}}$ (%)	T_{em6} (N.m)	$E_{T_{em}}$ (N.m)	TWD_{ψ_r} (%)	E_{ψ_r} (mWb)	E_{i_r} (A)	η (%)
1250	Euler	1.68	0.06	0.62	1.06	6.10	0.33	73.03
	Taylor	1.78	0.06	0.63	0.66	6.00	0.32	73.05
1550	Euler	1.74	0.10	0.71	0.53	6.70	0.40	75.64
	Taylor	1.94	0.11	0.73	1.76	6.50	0.36	76.12
1750	Euler	1.62	0.12	0.74	0.37	7.60	0.46	76.92
	Taylor	1.63	0.16	0.75	0.26	7.90	0.49	77.08

In Table 5.1 the TWD for torque $TWD_{T_{em}}$ and rotor flux TWD_{ψ_r} are shown, using both FE and TSE discretization methods. It also presents the prediction errors for the same variables, $E_{T_{em}}$, E_{ψ_r}, E_{i_r} and the amplitude of the 6th harmonic component of electromagnetic torque T_{em6}. The efficiency of the machine η is also presented. It can be concluded that both torque and rotor flux, become less distorted with the increase of the operating speed, as

Table 5.2: Execution time at tested operating speeds using FE and TSE discretization methods

n_r (rpm)	Discretization	Execution time (μs)
1250	Euler	44.66
	Taylor	48.58
1550	Euler	45.12
	Taylor	49.36
1750	Euler	44.68
	Taylor	48.67

evidenced by the decreasing values of $TWD_{T_{em}}$ and TWD_{ψ_r}. It also confirms that the errors of prediction for all variables increase for higher rotor speeds, as well as T_{em6}. The increase in η with higher speeds can be attested to the rotor power, which being proportional to rotor slip, starts flowing to the dc-bus at super-synchronous speed. The use of TSE always seems to implicate a more distorted torque waveform, evidenced by the higher $TWD_{T_{em}}$ and T_{em6} for all tested speeds. It also seems to diminish the accuracy of predictions for this particular variable. The only apparent improvements that the use of TSE bring to this particular setup is a diminished errors of prediction E_{i_r} and E_{ψ_r}, and very slight increase in the efficiency of the machine at all tested speeds. Additionally, the use of the TSE, brings an increased algorithm execution time of approximately 4 μs (Table 5.2).

The performance of the controller is now evaluated by a comparison for different sampling times T_s. The DFIG develops a constant torque of -12.5 N.m while running at 1250 rpm. The sampling times of 50 μs, 75 μs, and 100 μs were tested, in intervals of 33 ms. The use of the proposed discretization methods is also considered, to see if it can have an impact on mitigating performance deterioration with higher sampling times.

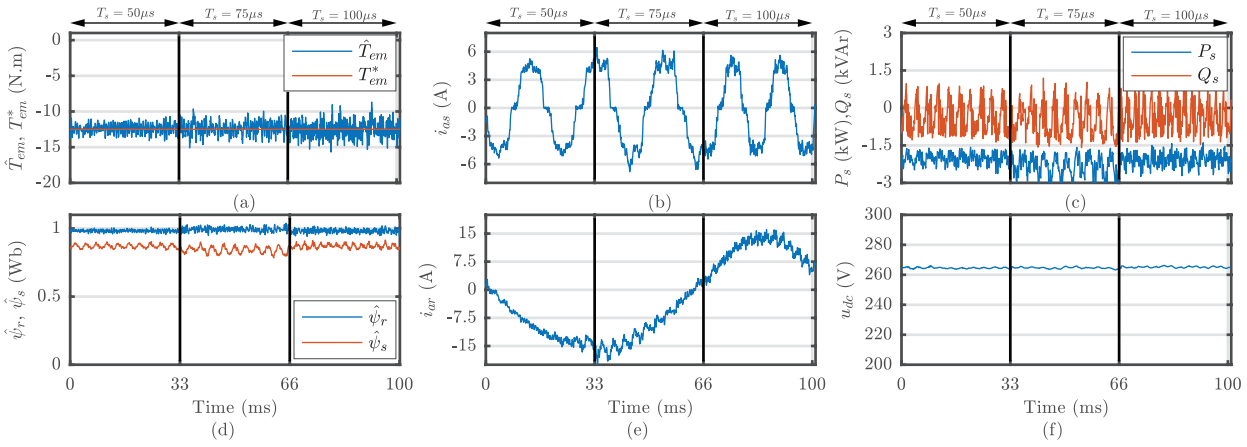

Fig. 5.8: Results for the DFIG steady-state operation at 1250 rpm, using FE and sampling times of 50, 75 and 100 μs: (a) electromagnetic and reference torque; (b) stator currents; (c) stator active and reactive power; (d) rotor and stator flux; (e) rotor currents; (f) dc-bus voltage

Figure 5.8 shows these results using the FE discretization method. With higher sampling times there is an increase in waveform distortion for all shown variables, with the most notorious case being for the stator power and torque, as well as for the stator and rotor fluxes. The increased distortion in the torque waveform is particularly visible for sampling times of 100 μs, as evidenced by the presence of more high-frequency ripple.

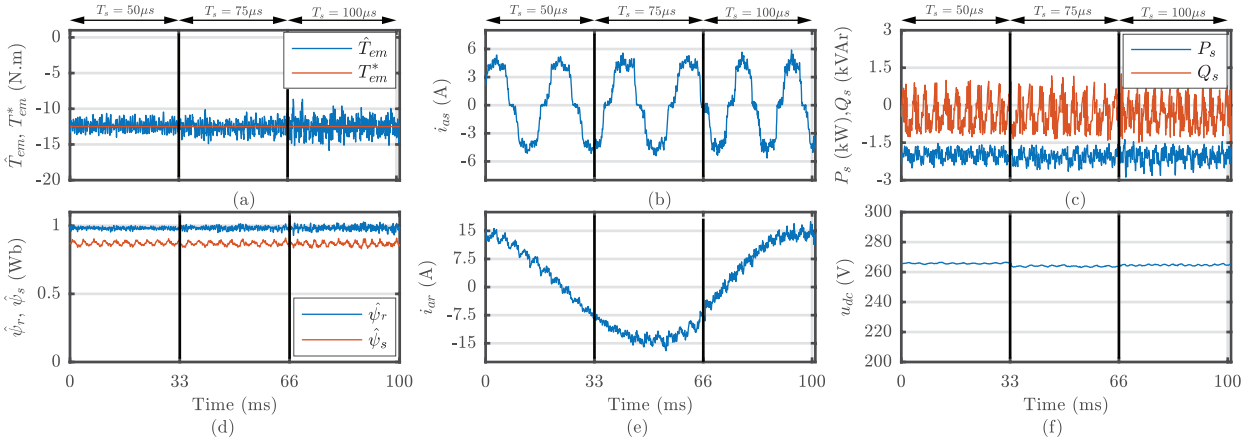

Fig. 5.9: Results for the DFIG steady-state operation at 1250 rpm, using TSE and sampling times of 50, 75 and 100 μs: (a) electromagnetic and reference torque; (b) stator currents; (c) stator active and reactive power; (d) rotor and stator flux; (e) rotor currents; (f) dc-bus voltage.

The results when using TSE discretization method (Figure 5.9) are very similar, although the stator power and both fluxes appear less affected in waveform distortion by the increase of the sampling time.

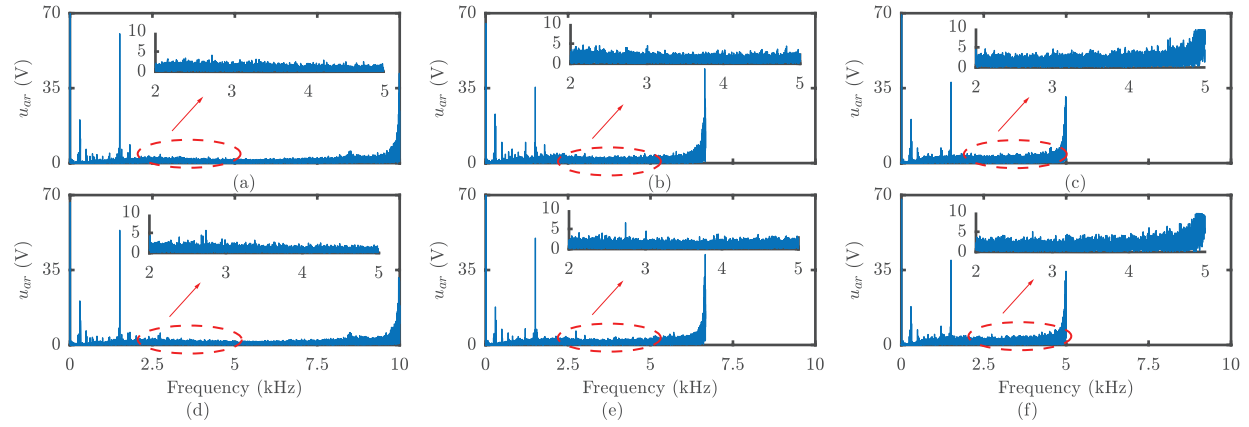

Fig. 5.10: Spectra of rotor voltage at 1250 rpm using different discretization techniques and sampling times: (a) FE and T_s=50μs; (b) FE and T_s=75μs; (c) FE and T_s=100μs; (d) TSE and T_s=50μs; (e) TSE and T_s=75μs; (f) TSE and T_s=100μs.

Figure 5.10 shows the high-frequency spectrum of rotor voltage for the 3 tested sampling times and while the DFIG was running at 1250 rpm. The decrease in the switching frequency

of the inverter, with the increase of the sampling time T_s, can be seen. The use of different discretization methods brought no apparent change to the high-frequency spectral content of the rotor voltage, although the use of FE method seems to indicate more low-frequency content.

Table 5.3 confirms the increase in distortion brought by larger sampling times, for both torque and rotor flux waveforms, as well as increased prediction errors for all variables. It shows, however that the performance of the system is less deteriorated with higher sampling times, if the more demanding TSE method is used. With this method, the system exhibits the lowest errors of predictions of all state variables E_{ψ_r}, E_{i_r}. It also shows that the use of TSE also brings a lower value for T_{em6}, for higher sampling times. Attending that the system can also achieve a lower value of $TWD_{T_{em}}$ for a sampling time of $100\mu s$, the use of more elaborate discretization methods can be justifiable if this parameter assumes a higher value. However, the use of different discretization techniques does not bring noticeable change to the efficiency of the system, even when operating with higher T_s.

Table 5.3: Total waveform distortion and prediction errors, at 1250 rpm, using the proposed discretization methods and sampling times of 50, 75 and 100 μs.

$T_s(\mu s)$	Discretization	$TWD_{T_{em}}$ (%)	T_{em6} (N.m)	$E_{T_{em}}$ (N.m)	TWD_{ψ_r} (%)	E_{ψ_r} (mWb)	E_{i_r} (A)	η(%)
50	Euler	1.68	0.06	0.62	1.06	6.10	0.33	73.03
	Taylor	1.78	0.06	0.63	0.66	6.00	0.32	73.05
75	Euler	2.18	0.24	1.01	1.38	8.80	0.57	76.25
	Taylor	2.23	0.10	0.90	1.11	7.80	0.48	76.63
100	Euler	2.89	0.23	1.12	1.40	8.80	0.65	78.85
	Taylor	2.63	0.18	1.15	1.45	8.80	0.61	78.68

5.2.2 Dynamic Operation

The DFIG was subjected to the same tests as in the previous chapter: a torque ramp variation to attest the operability of the system at a wide load torque range. In order to assess the response of the DFIG under load torque disturbances, a load torque step test was made. Additionally, the DFIG was subjected to a speed ramp variation, as to confirm that the system works properly in both sub-synchronous and super-synchronous modes of operation. In all previous situations a comparison is made between the responses of the system, when using the two different discretization techniques.

5.2.2.1 Torque Ramp Response

The system is subjected to a torque ramp covering the loads of −3 to −12.5 N.m in 2 seconds. Figure 5.11 illustrates the response of the system during this test and when the FE discretization method is used. At low torque, the system works with rotor flux level

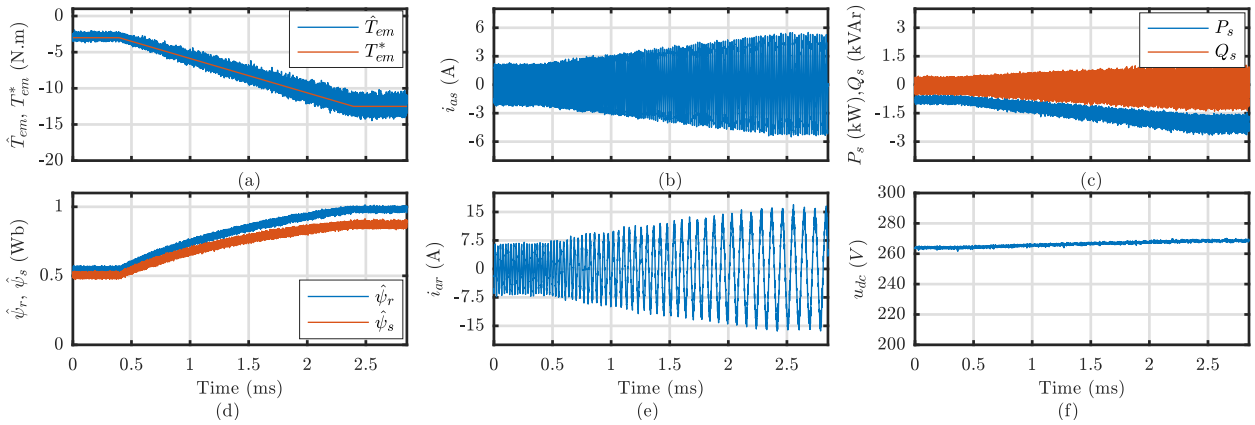

Fig. 5.11: Results for a torque ramp response at 1550 rpm using FE : (a) electromagnetic and reference torque; (b) stator currents; (c) stator active and reactive power; (d) rotor and stator flux; (e) rotor currents; (f) dc-bus voltage.

optimization, but at high torque levels this variable is saturated as it would exceed the rated value of 1 Wb. The increase of stator frequency for low-load levels is also confirmed. Also proved is the relation between the developed torque by the DFIG and the active power delivered by the stator windings. It can also be seen that the dc-bus voltage level increases slightly when the DFIG develops higher torque levels.

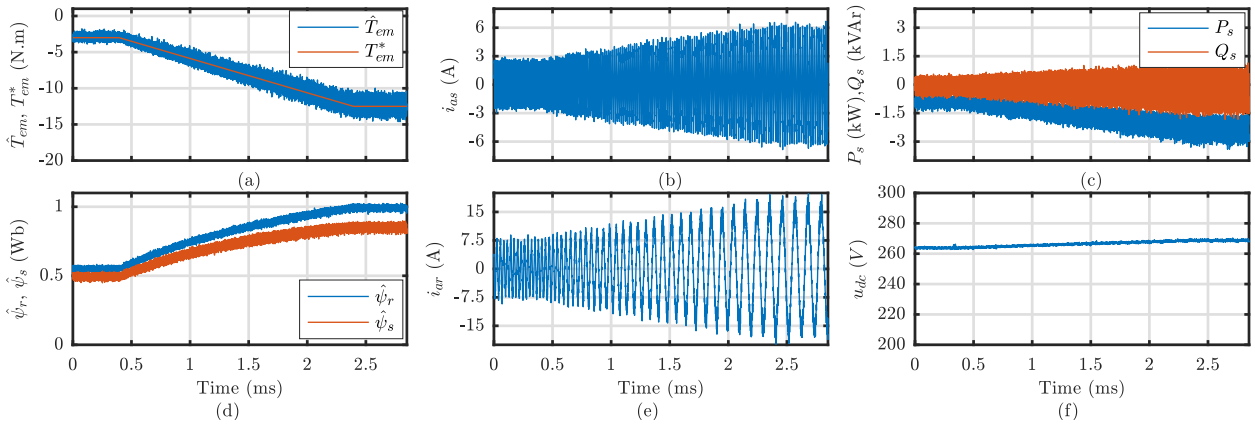

Fig. 5.12: Results for a torque step response at 1550 rpm using TSE : (a) electromagnetic and reference torque; (b) stator currents; (c) stator active and reactive power; (d) rotor and stator flux; (e) rotor currents; (f) dc-bus voltage.

The use of the TSE discretization technique brought no apparent improvement to the system, when applied during this test (Figure 5.12). It shows a notorious increase in waveform distortion for both stator powers. This is also visible in the stator flux waveform, but to a lesser extent. Additionally, both the electromagnetic torque and rotor flux presents a little more ripple.

5.2.2.2 Torque Step Response

The DFIG was subjected to a -12.5 N.m torque step at 10 ms, without initially developing any torque. The rotor speed was held constant at 1250 rpm.

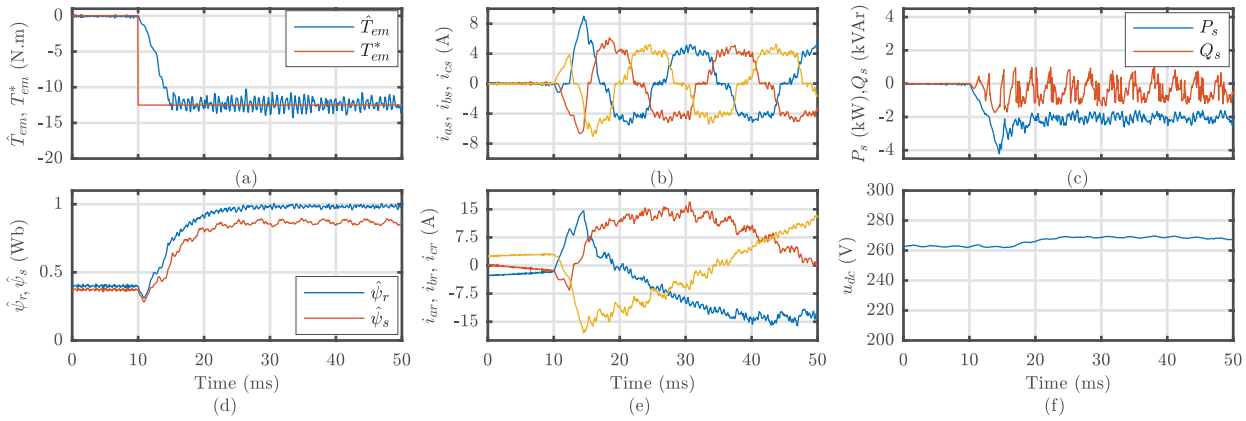

Fig. 5.13: Results of torque step response at 1250 rpm using FE : (a) electromagnetic and reference torque; (b) stator currents; (c) stator active and reactive power; (d) rotor and stator flux; (e) rotor currents; (f) dc-bus voltage.

It is shown in Figure 5.13 that the estimated torque can follow its intended reference in approximately 5 ms, proving its fast dynamic operation. The rotor flux is adjusted to the rated value, showing however a longer response time due to the low-pass filter used in the optimum rotor flux level generation module. After the torque step, the stator power surpasses the value of 4 kW, before settling at half that value in steady-state. The stator current also overshoots, with the current in all phases surpassing the steady-state amplitude of approximately 4 A. After the torque step there is also a slight increase in the dc-bus voltage.

The use of the TSE discretization method brought positive results for this particular test (Figure 5.14). It can be seen that the torque response is slightly faster than in previous case, now achieving the intended reference in 4 ms. It is also evident the lower overshoot for both

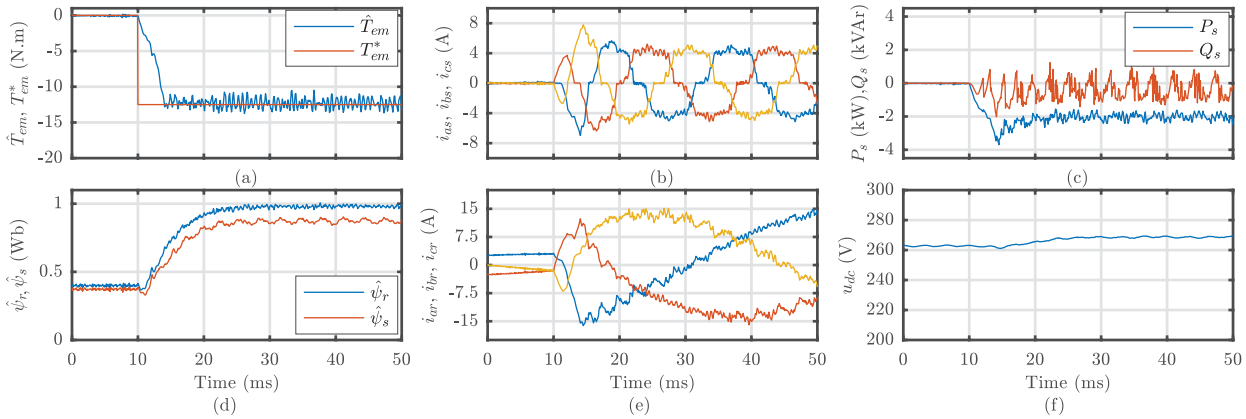

Fig. 5.14: Results of torque step response at 1250 rpm using Taylor Expansion : (a) electromagnetic and reference torque; (b) stator currents; (c) stator active and reactive power; (d) rotor and stator flux; (e) rotor currents; (f) dc-bus voltage.

stator power and currents. For all other variables, it does not exhibit any noticeable change when compared to the use of the FE method.

5.2.2.3 Speed Ramp Response

The DFIG was subjected to a speed ramp, spanning from 1250 to 1750 rpm while developing constant rated torque of -12.5 N.m. Its response is shown in Figure 5.15.

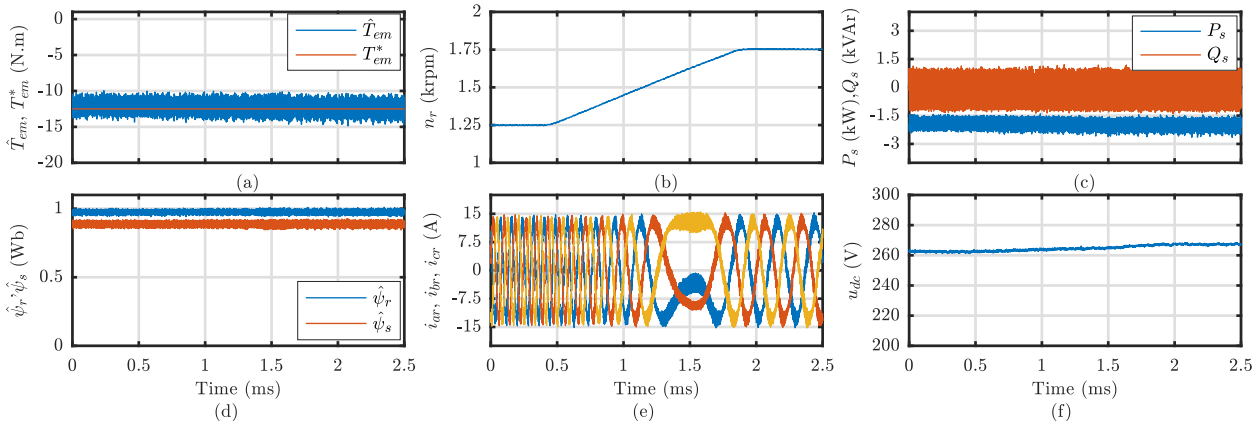

Fig. 5.15: Results for a speed ramp response using FE: (a) electromagnetic and reference torque; (b) rotor speed; (c) stator active and reactive power; (d) rotor and stator flux; (e) rotor currents; (f) dc-bus voltage.

It is possible to confirm that, the rotor frequency is proportional to slip, as it decreases as the DFIG reaches synchronous speed. At this speed the phase reversal of rotor currents is also visible. As the machine enters into super-synchronous speeds, the rotor starts delivering

power to the dc-bus, as evidenced by the slight increase in dc-bus voltage. The use of different

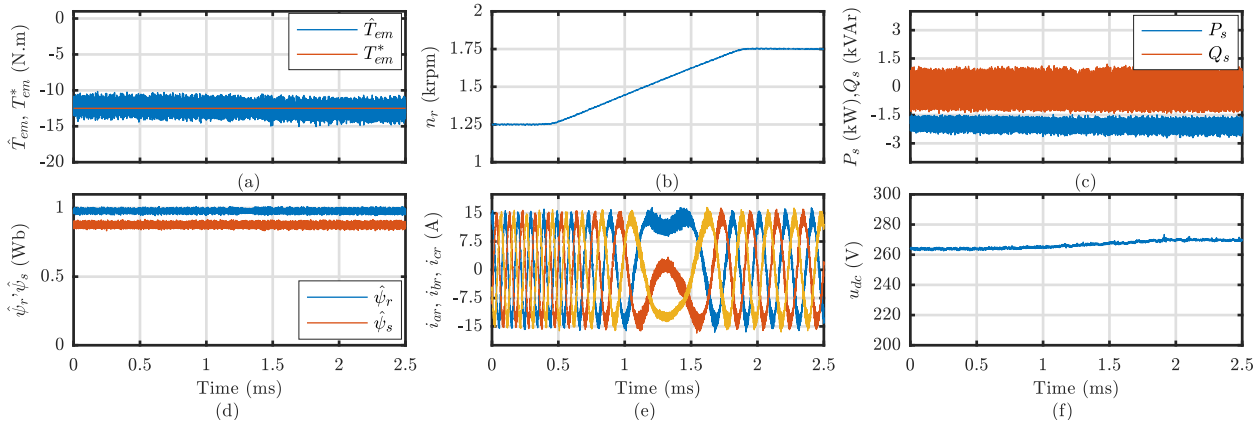

Fig. 5.16: Results for a speed ramp response using TSE: (a) electromagnetic and reference torque; (b) rotor speed; (c) stator active and reactive power; (d) rotor and stator flux; (e) rotor currents; (f) dc-bus voltage.

discretization techniques brought no apparent change to the system response, when exposed to a speed ramp (Figure 5.16).

5.2.3 Sensitivity Analysis

The effects of rotor parameters variation on the performance of the system are evaluated for steady-state operation at 1250 rpm. Apart from quantifying the uncertainty that arise during parameter estimation, it will also account for the error introduced by the numerical methods used to solve the differential equations that comprise this model. It will also allow to assess if the use of different discretization methods can make the system more robust towards parameter mismatch. The system is subjected to variations of 30% in the rotor windings resistance R_r' and leakage inductance L_{lr}' on the controller, in intervals of 33 ms.

Figure 5.17 shows that the control algorithm is robust against this parameter variation, as it can operate correctly with both R_r' under-rating and over-rating on the control level. This parameter variation does not bring any visible increased distortion or high-frequency ripple in all shown waveforms, except for stator currents, in the case of this parameter over-estimation. It also confirms that both stator and rotor fluxes have decreasing amplitudes, with the increase of R_r' on the controller.

The use of TSE brought no apparent change to the waveforms shown for this particular test, as can be seen in Figure 5.18.

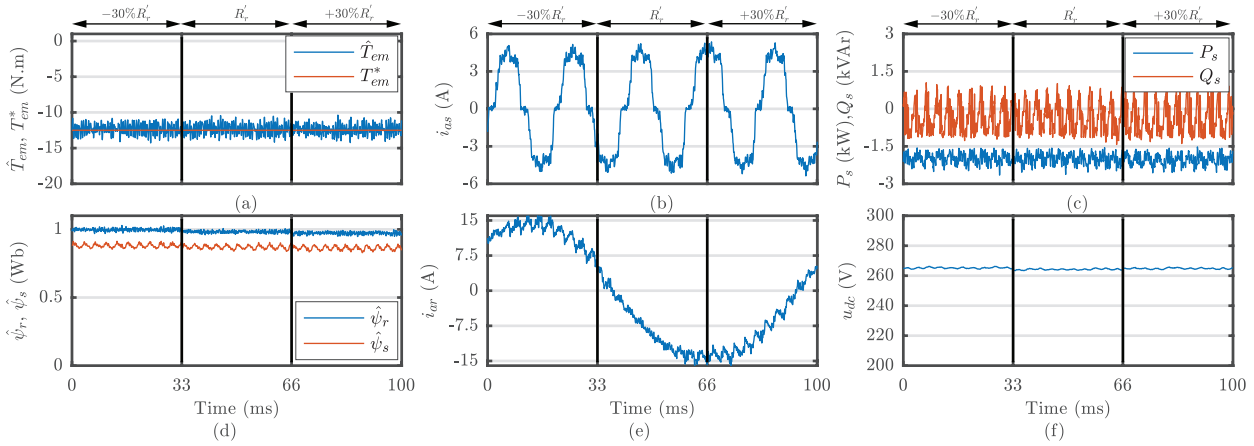

Fig. 5.17: Results for rotor resistance variation using FE: (a) electromagnetic and reference torque; (b) stator currents; (c) stator active and reactive power; (d) rotor and stator flux; (e) rotor currents; (f) dc-bus voltage.

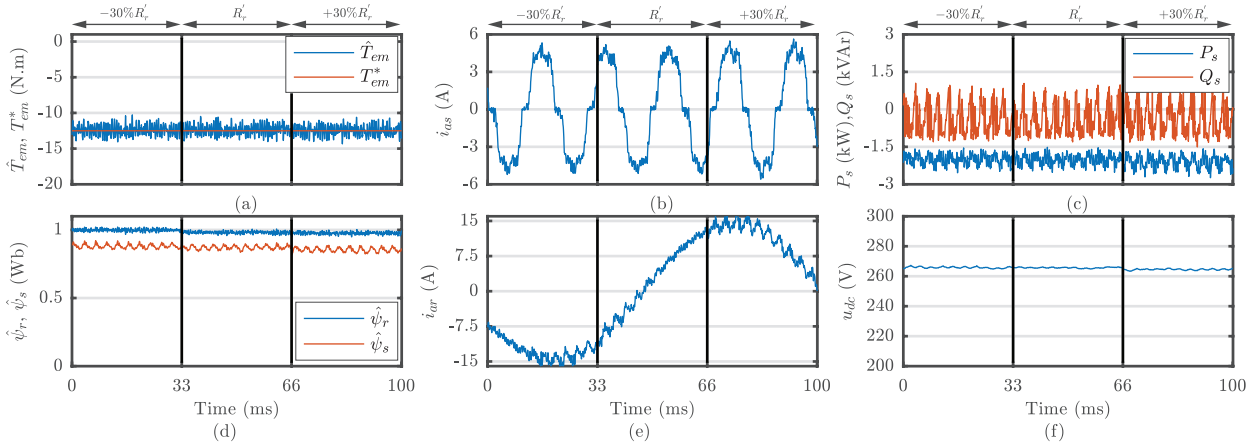

Fig. 5.18: Results for rotor resistance variation using TSE: (a) electromagnetic and reference torque; (b) stator currents; (c) stator active and reactive power; (d) rotor and stator flux; (e) rotor currents; (f) dc-bus voltage

When the system experiences a mismatch in rotor leakage inductance L'_{lr} it still exhibits the ability to operate correctly. However, it can now be seen in Figure 5.19 that the under-rating of this parameter particularly increases the high-frequency torque ripple. It also appears to increase the waveform distortion of the stator currents. Both the stator and the rotor fluxes not only present increased levels of distortion with both the under-value and over-value of this parameter, but varying amplitude as well. The presented fluxes show increasing amplitudes when larger values of L'_{lr} are considered.

Figure 5.20 shows that the use of the alternative TSE method brings no apparent change to the depicted waveforms.

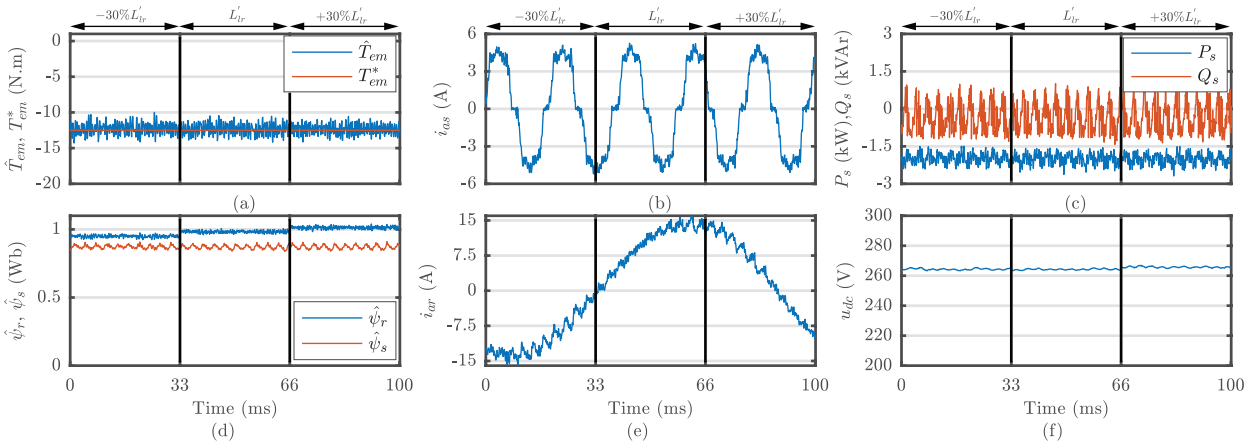

Fig. 5.19: Results for rotor leakage inductance variation using FE: (a) electromagnetic and reference torque; (b) stator currents; (c) stator active and reactive power; (d) rotor and stator flux; (e) rotor currents; (f) dc-bus voltage.

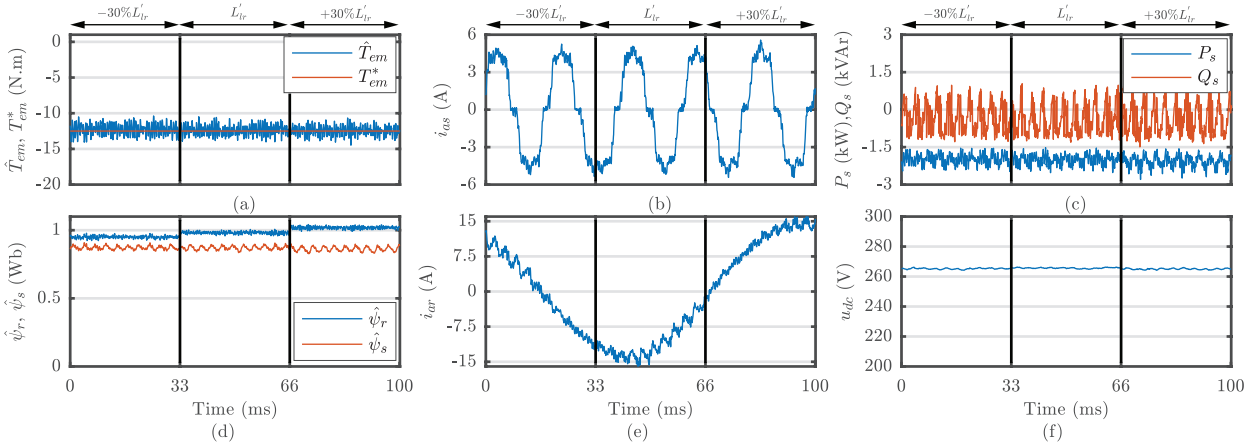

Fig. 5.20: Results for rotor leakage inductance variation using TSE: (a) electromagnetic and reference torque; (b) stator currents; (c) stator active and reactive power; (d) rotor and stator flux; (e) rotor currents; (f) dc-bus voltage.

It is shown in Table 5.4 that the rotor current prediction error E_{i_r} do not change significantly with rotor parameter variation, only showing an increase in error in the case of L'_{lr} under-estimation. In the case of E_{ψ_r}, it appears to be more sensitive to L'_{lr} over-values. The system has smaller prediction errors for these variables if the TSE is used. As they were defined as state variables of the system, it is confirmed that the use of enhanced discretization methods can make the system more robust towards parameter mismatch, at least for these variables. The errors of prediction for torque $E_{T_{em}}$ also achieve the highest value when L'_{lr} is under-rated, however, it is the use of Forward Euler that achieves better accuracy of predictions. The value of $TWD_{T_{em}}$ also assumes a lower value when the Forward Euler

discretization method is used, however this value seems more susceptible to change, for all tested conditions.

Table 5.4: Total waveform distortion and prediction errors for sensitivity analysis of the DFIG-dc system

	Discretization	$TWD_{T_{em}}$ (%)	T_{em6} (N.m)	$E_{T_{em}}$ (N.m)	TWD_{ψ_r} (%)	E_{ψ_r} (mWb)	E_{i_r} (A)	η(%)
$R_r^{'}\&L_{lr}^{'}$	Euler	1.68	0.06	0.62	1.06	6.10	0.33	73.03
	Taylor	1.78	0.06	0.63	0.66	6.00	0.32	73.05
$-30\%R_r^{'}$	Euler	1.77	0.03	0.64	0.67	6.10	0.33	72.95
	Taylor	1.78	0.06	0.65	1.07	6.00	0.32	70.35
$+30\%R_r^{'}$	Euler	1.62	0.05	0.61	0.83	6.30	0.32	73.31
	Taylor	1.78	0.05	0.66	0.77	6.00	0.31	72.85
$-30\%L_{lr}^{'}$	Euler	1.82	0.07	0.68	0.74	6.00	0.42	81.92
	Taylor	1.86	0.07	0.69	0.78	5.90	0.41	72.91
$+30\%L_{lr}^{'}$	Euler	1.54	0.04	0.57	1.11	6.50	0.28	73.36
	Taylor	1.70	0.03	0.61	1.01	6.50	0.27	81.92

Chapter 6

Conclusions and Future Work

Throughout this dissertation the use of a predictive control strategy applied to a DFIG connected to a dc-grid was studied.

FCS-MPC proved to be an excellent alternative to the commonly used FOC, due to its simplicity of configuration and to the good results shown, both in steady-state and dynamic operation. It does not rely on the use of PI controllers for achieving field orientation and frequency regulation, thereby avoiding the cascaded control loop [19, 28–31] and achieving minimal tuning effort. Since the control strategy was implemented on a rotor reference frame, it also did not require the knowledge of slip frequency nor stator frequency, required for reference frame transformations [31, 32]. The presence of the undesirable low-frequency oscillations in the electromagnetic torque are also minimal, without requiring the use resonant controllers nor different harmonic reference frames that were the commonly reported solution of [5, 16, 17, 20] and are of more difficult implementation.

The system demonstrated the ability to operate in steady-state in a wide torque and speed ranges, spanning the operation of the DFIG from sub-synchronous to super-synchronous modes. It also showed very fast dynamic response while subjected to a torque step, achieving the intended reference value in less than 5 ms. The DFIG was also able to operate correctly when subjected to a torque or speed ramp. The results also show the robustness of the system against rotor parameter mismatch, being able to operate correctly with 30% variation for both rotor windings resistance and leakage inductance. The most unfavourable condition appears to be the under-rating of the rotor leakage inductance, showing the highest torque waveform distortion and prediction errors for all variables.

Additionally, a comparison between different discretization methods was provided with the more simple and common FE being compared with a more elaborated and computational demanding TSE. The latter discretization technique has the ability to decrease system prediction errors, but only to the variables defined as state variables of the system, *i.e.* rotor flux and current. In spite of that the use of this discretization method always brought increased distortion and prediction errors for torque. This can also be extended to the waveform distortion present in the rotor flux. However, the differences brought by the use of TSE are minimal, allowing to conclude that in steady-state the use of the different discretization methods brings the same results. If larger sampling times are used, the control algorithm using the TSE method appears to achieve slightly superior steady-state performance, although the differences are still minimal. When the controller was subjected to rotor parameters variation, the system discretized by TSE still retained smaller errors of prediction for both rotor current and rotor flux, as well as higher levels of waveform distortion for torque. However, these differences can be considered negligible. The only visible difference that the use of TSE brought was a faster response to the torque step test, as well as less overshooting current and stator power. There was no difference in the response of this system when subjected to a speed ramp. As such it can be concluded that for the DFIG-dc system, the use of TSE discretization method does not bring any significant improvement to the performance of the system.

For future work, the following suggestions can be considered:

- Development of a control system with a reduced number of sensors on the stator side;
- Implementation of a control system without rotor-position sensor;
- Extension of the studied topology and control method to a stand-alone generator;

References

[1] M. Shahabi, M. R. Haghifam, M. Mohamadian, and S. A. Nabavi-Niaki. Microgrid dynamic performance improvement using a doubly fed induction wind generator. *IEEE Transactions on Energy Conversion*, 24(1):137–145, March 2009.

[2] S. Augustine, N. Lakshminarasamma, and M. K. Mishra. Control of photovoltaic-based low-voltage dc microgrid system for power sharing with modified droop algorithm. *IET Power Electronics*, 9(6):1132–1143, 2016.

[3] Venkata Yaramasu and Bin Wu. *Model Predictive Control of Wind Energy Conversion Systems*. 12 2016.

[4] R. Cardenas, R. Pena, S. Alepuz, and G. Asher. Overview of control systems for the operation of dfigs in wind energy applications. *IEEE Transactions on Industrial Electronics*, 60(7):2776–2798, July 2013.

[5] M. F. Iacchetti, G. D. Marques, and R. Perini. Operation and design issues of a doubly fed induction generator stator connected to a dc net by a diode rectifier. *IET Electric Power Applications*, 8(8):310–319, September 2014.

[6] G. D. Marques and M. F. Iacchetti. Inner control method and frequency regulation of a dfig connected to a dc link. *IEEE Transactions on Energy Conversion*, 29(2):435–444, June 2014.

[7] G. Abad, J. López, M. Rodríguez, L. Marroyo, and G. Iwanski. *Doubly Fed Induction Machine: Modeling and Control for Wind Energy Generation*. IEEE Press Series on Power Engineering. Wiley, 2011.

[8] M. E. Montilla-DJesus, D. Santos-Martin, S. Arnaltes, and E. D. Castronuovo. Optimal operation of offshore wind farms with line-commutated hvdc link connection. *IEEE Transactions on Energy Conversion*, 25(2):504–513, June 2010.

[9] J. Robinson, D. Jovcic, and G. Joos. Analysis and design of an offshore wind farm using a mv dc grid. *IEEE Transactions on Power Delivery*, 25(4):2164–2173, Oct 2010.

[10] M. Tsili and S. Papathanassiou. A review of grid code technical requirements for wind farms. *IET Renewable Power Generation*, 3(3):308–332, Sept 2009.

[11] J. Rodriguez and P. Cortes. *Predictive Control of Power Converters and Electrical Drives*. Wiley - IEEE. Wiley, 2012.

[12] H. Misra and A. K. Jain. Analysis of stand-alone dfig-dc system and dc voltage regulation with reduced sensors. *IEEE Transactions on Industrial Electronics*, 64(6):4402–4412, June 2017.

[13] A. Gundavarapu, H. Misra, and A. K. Jain. Direct torque control scheme for dc voltage regulation of the standalone dfig-dc system. *IEEE Transactions on Industrial Electronics*, 64(5):3502–3512, May 2017.

[14] S. Bayhan, H. Abu-Rub, and O. Ellabban. Sensorless model predictive control scheme of wind-driven doubly fed induction generator in dc microgrid. *IET Renewable Power Generation*, 10(4):514–521, 2016.

[15] H. Nian and X. Yi. Coordinated control strategy for doubly-fed induction generator with dc connection topology. *IET Renewable Power Generation*, 9(7):747–756, 2015.

[16] H. Nian, C. Wu, and P. Cheng. Direct resonant control strategy for torque ripple mitigation of dfig connected to dc link through diode rectifier on stator. *IEEE Transactions on Power Electronics*, 32(9):6936–6945, Sept 2017.

[17] G. D. Marques and M. F. Iacchetti. Minimization of torque ripple in the dfig-dc system via predictive delay compensation. *IEEE Transactions on Industrial Electronics*, 65(1):103–113, Jan 2018.

[18] H. Misra, A. Gundavarapu, and A. K. Jain. Control scheme for dc voltage regulation of stand-alone dfig-dc system. *IEEE Transactions on Industrial Electronics*, 64(4):2700–2708, April 2017.

[19] G. D. Marques and M. F. Iacchetti. Stator frequency regulation in a field-oriented controlled dfig connected to a dc link. *IEEE Transactions on Industrial Electronics*, 61(11):5930–5939, Nov 2014.

[20] M. F. Iacchetti, G. D. Marques, and R. Perini. Torque ripple reduction in a dfig-dc system by resonant current controllers. *IEEE Transactions on Power Electronics*, 30(8):4244–4254, Aug 2015.

[21] J. Li and K. Corzine. A sensorless flux oriented control scheme for a dfig connected to a dc link. In *2015 Clemson University Power Systems Conference (PSC)*, pages 1–5, March 2015.

[22] L. Fan, S. Yuvarajan, and R. Kavasseri. Harmonic analysis of a dfig for a wind energy conversion system. *IEEE Transactions on Energy Conversion*, 25(1):181–190, March 2010.

[23] N. Yu, H. Nian, and Y. Quan. A novel dc grid connected dfig system with active power filter based on predictive current control. In *2011 International Conference on Electrical Machines and Systems*, pages 1–5, Aug 2011.

[24] M. F. Iacchetti and G. D. Marques. Enhanced torque control in a dfig connected to a dc grid by a diode rectifier. In *2014 16th European Conference on Power Electronics and Applications*, pages 1–9, Aug 2014.

[25] G. Marques and M. Iacchetti. Overcurrent estimation in a doubly-fed induction generator-dc system during a voltage dip in the dc grid. *IET Renewable Power Generation*, 10(7):1024–1032, 2016.

[26] G. D. Marques and D. M. Sousa. Understanding the doubly fed induction generator during voltage dips. *IEEE Transactions on Energy Conversion*, 27(2):421–431, June 2012.

[27] M. F. Iacchetti and G. D. Marques. Voltage control in a dfig-dc system connected to a stand-alone dc load. In *2015 9th International Conference on Compatibility and Power Electronics (CPE)*, pages 323–328, June 2015.

[28] G. D. Marques and M. F. Iacchetti. Control method of the dfig connected to a dc link through a diode bridge. *Energy and Power Engineering*, 5(4B):102–108, July 2013.

[29] G. D. Marques and M. F. Iacchetti. A self-sensing stator-current-based control system of a dfig connected to a dc-link. *IEEE Transactions on Industrial Electronics*, 62(10):6140–6150, Oct 2015.

[30] M. F. Iacchetti, G. D. Marques, and R. Perini. A scheme for the power control in a dfig connected to a dc bus via a diode rectifier. *IEEE Transactions on Power Electronics*, 30(3):1286–1296, March 2015.

[31] G. D. Marques, D. M. Sousa, and M. F. Iacchetti. Air-gap power-based sensorless control in a dfig connected to a dc link. *IEEE Transactions on Energy Conversion*, 30(1):367–375, March 2015.

[32] G. D. Marques and M. F. Iacchetti. Sensorless frequency and voltage control in the stand-alone dfig-dc system. *IEEE Transactions on Industrial Electronics*, 64(3):1949–1957, March 2017.

[33] G. D. Marques, J. Santana, and M. F. Iacchetti. A new direct slip-position estimator mras self-sensing control method for application on the dfig connected to a dc network trough a diode rectifier on the stator circuits. In *2014 16th European Conference on Power Electronics and Applications*, pages 1–9, Aug 2014.

[34] G. D. Marques and M. F. Iacchetti. Field-weakening control for efficiency optimization in a dfig connected to a dc-link. *IEEE Transactions on Industrial Electronics*, 63(6):3409–3419, June 2016.

[35] H. Nian and Y. Song. Direct power control of doubly fed induction generator under distorted grid voltage. *IEEE Transactions on Power Electronics*, 29(2):894–905, Feb 2014.

[36] R. Errouissi, A. Al-Durra, S. M. Muyeen, S. Leng, and F. Blaabjerg. Offset-free direct power control of dfig under continuous-time model predictive control. *IEEE Transactions on Power Electronics*, 32(3):2265–2277, March 2017.

[37] C. A. Silva and J. I. Yuz. On sampled-data models for model predictive control. In *IECON 2010 - 36th Annual Conference on IEEE Industrial Electronics Society*, pages 2966–2971, Nov 2010.

[38] L. Wang, S. Chai, D. Yoo, L. Gan, and K. Ng. *PID and Predictive Control of Electrical Drives and Power Converters using MATLAB / Simulink*. IEEE Press Series on Power Engineering. Wiley, 2014.

[39] C. A. Rojas, J. I. Yuz, M. Aguirre, and J. Rodriguez. A comparison of discrete-time models for model predictive control of induction motor drives. In *2015 IEEE International Conference on Industrial Technology (ICIT)*, pages 568–573, March 2015.

[40] E. S. de Santana, E. Bim, and W. C. do Amaral. A predictive algorithm for controlling speed and rotor flux of induction motor. *IEEE Transactions on Industrial Electronics*, 55(12):4398–4407, Dec 2008.

[41] H. Miranda, P. Cortes, J. I. Yuz, and J. Rodriguez. Predictive torque control of induction machines based on state-space models. *IEEE Transactions on Industrial Electronics*, 56(6):1916–1924, June 2009.

[42] P. Vaclavek and P. Blaha. Enhanced discrete time model for ac induction machine model predictive control. In *IECON 2012 - 38th Annual Conference on IEEE Industrial Electronics Society*, pages 5043–5048, Oct 2012.

[43] F. Wang, S. Li, X. Mei, W. Xie, J. Rodríguez, and R. M. Kennel. Model-based predictive direct control strategies for electrical drives: An experimental evaluation of ptc and pcc methods. *IEEE Transactions on Industrial Informatics*, 11(3):671–681, June 2015.

[44] J. Hu, H. Nian, H. Xu, and Y. He. Dynamic modeling and improved control of dfig under distorted grid voltage conditions. *IEEE Transactions on Energy Conversion*, 26(1):163–175, March 2011.

[45] S. Anand, B. G. Fernandes, and J. Guerrero. Distributed control to ensure proportional load sharing and improve voltage regulation in low-voltage dc microgrids. *IEEE Transactions on Power Electronics*, 28(4):1900–1913, April 2013.

[46] Mohsen Bandar Abadi. *Fault diagnosis in AC drives and DFIG systems based on three-level NPC converters*. PhD thesis, University of Coimbra, 2017.

Appendix A

Simulation Model

A general overview of the simulation model built in MATLAB/Simulink environment used to assess the performance of the DFIG-dc system is shown in Figure A1. The machine used in the simulation was a wound-rotor induction machine, whose parameters are given in Table B.1. This motor receives as input the voltages applied to the rotor and the imposed speed of operation.

The 'Universal Bridge' block contains the model of an uncontrolled diode rectifier, and is feeds by the dc source, which simulates the dc grid. The inverter was modelled by six ideal IGBTs model with its respective free-wheeling diodes.

The 'Measurements' block measures all current and voltage signals, from both the rotor and stator, for future use in the controller. It transforms the line-to-line voltages applied to the motor into phase voltages to be used by the control system. It also handles the mechanical displacement of the rotor signal and its estimated speed. All these signals are outputs coming from the machine model.

The 'Predictive Torque and Rotor Flux Control' block is composed by 4 different stages. In the first stage the flux estimation for instant $[k]$ is made. The magnetizing inductance to be used in each sampling time is also estimated here through a look-up table. It is followed by 2 stages of prediction, one for instant $[k+1]$ and another for two-samples ahead predictions. The final stage is the cost function evaluation, where the choice of the applied voltage vector is made, based on the minimization of this function.

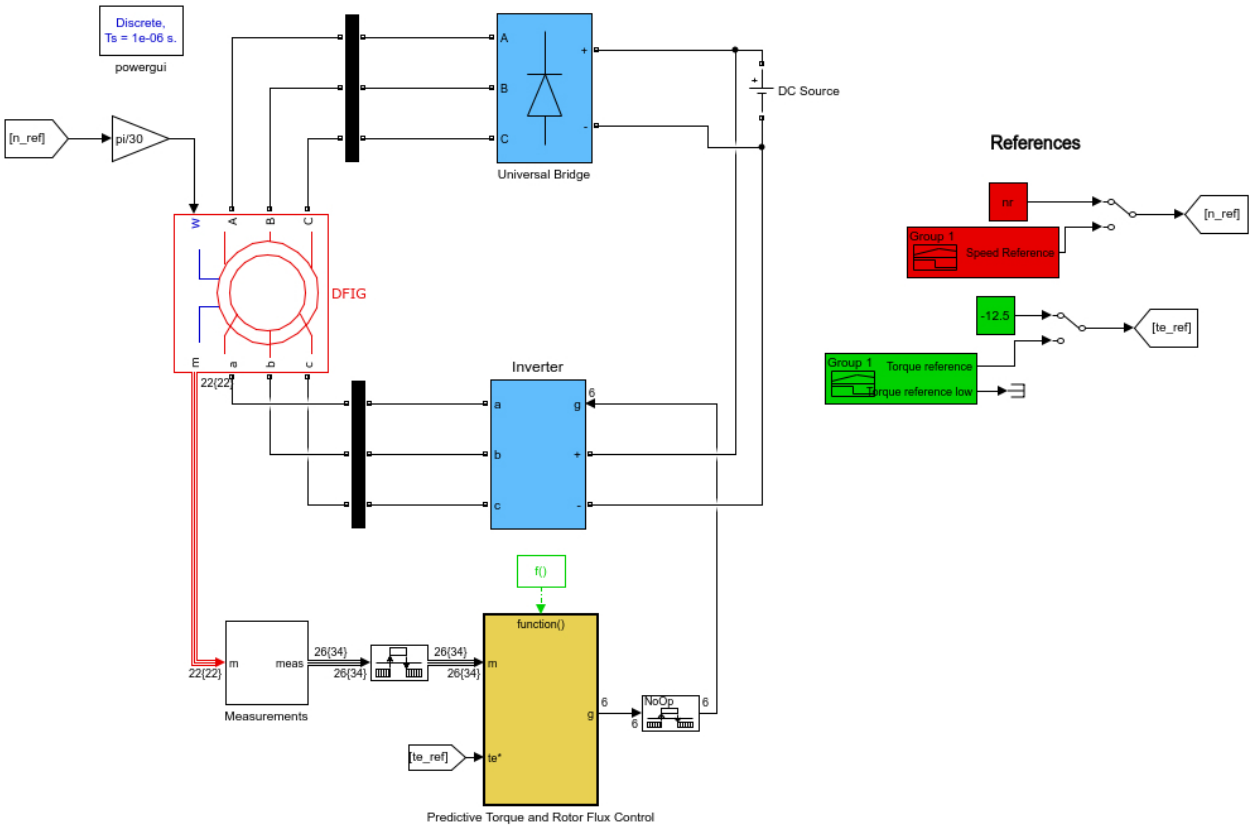

Fig. A1: Simulation model of the FCS-MPC control strategy applied to the DFIG-dc system

Appendix B

System Parameters

The parameters of the DFIG used in the simulations and in the experimental work are given in Table B.1. U_s, U_r, I_s and I_r represent the stator and rotor voltages and currents, in RMS values, respectively. n_r, f_n, P_n stand for the DFIG nominal speed, frequency and active power.

Table B.1: DFIG and rotor filter parameters

Doubly-Fed Induction Generator				Rotor-Side filter	
Nameplate Information		Measured Parameters		Nameplate Information	
U_s	400 V	R_s	1.29 Ω	U_n	400 V
I_s	9.4 A	$R_r^{'}$	1.344 Ω	I_n	11.5 A
U_r	240 V	L_{ls}	7.922 mH	L_f	2.6 mH
I_r	11.5 A	$L_{lr}^{'}$	7.922 mH	R_f	0.13 Ω
n_r	1420 rpm	a	1.7		
f_n	50 Hz	p	2		
P_n	4 kW				

The measurement of a dc voltage and current across the wye-connected windings, as suggested in [7], allowed for the values of R_s and R_r to be found.

The value of the magnetizing inductance L_m is susceptible to change, depending on the amplitude and frequency of the current that flows through it. The estimation of this parameter was performed in [46], with a no-load test, and its values and corresponding magnetizing current I_m are shown in Figure B.1(a). These values were then loaded into a look-up table and introduced in the control system, forcing the value of L_m (and of L_r and L_s) to be updated at every iteration, based on the measured values of stator and rotor

currents (Figure B.1(b)). The estimation of the values for the stator and rotor leakage inductances L_{ls}, L_{lr}, and transformation ratio a, were also performed in [46].

The nameplate information of the inductive filter connected between the inverter and the rotor windings is also given in Table B.1. L_f and R_f indicate its value of inductance and series resistance, respectively.

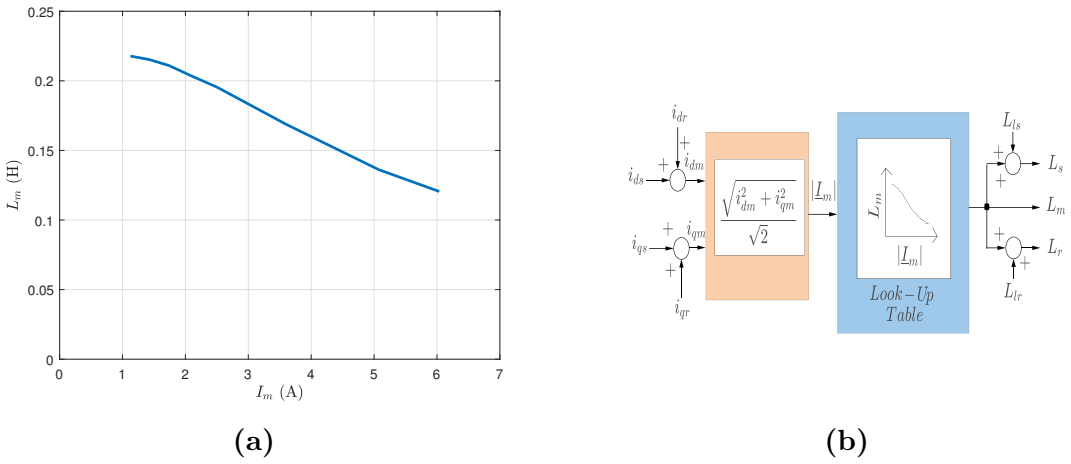

(a) **(b)**

Fig. B.1: Magnetizing inductance estimation: a) magnetization curve; b) look-up Table generation

Appendix C

Experimental Setup

A System Components

In the following figures all the components used throughout the experimental set-up of this work are depicted.

The DFIG coupled to the SCIM are shown in Figure C.1, represented by the letters (a) and (c), respectively. Between these machines there is the torque sensor RWT-321-EC-K from TORQSENS, capable of estimating torque and speed up to 30 N.m and 12000 rpm. The torque sensor is represented by the letter (b)

The inverter bridge used to control the DFIG is presented in Figure C.2 (a). Its the SKiiP132GD120-3DUL from SEMIKRON, with nominal values for voltage and current of 1200 V and 150 A. The inductive filter connected between the inverter and rotor windings is in Figure C.2 (b)

For the stator side converter, the VUO82-12NO7 three-phase diode rectifier from IXYS was used (Figure C.3 (a)). The autotransformer that ensures that the stator and rotor of the DFIG can be connected to the same dc-bus is shown in Figure C.3 (b)

At the dc-bus, where both the diode bridge and inverter are connected, there is also a 3400 μF capacitor-bank (Figure C.4 (a)) and a 35Ω resistive load (Figure C.4 (b)).

The variable speed drive used to feed the primary machine and impose the DFIG's rotation is the CFW11 from WEG (Figure C.5 (a)). Its remote controller (Figure C.5 (b)) is used to impose the primary machine's speed of rotation, or define the speed and torque

Fig. C.1: Experimental set-up of the DFIG-dc: (a) doubly-fed induction generator; (b) torque sensor; (c) squirrel-cage induction motor controlled by the VSD

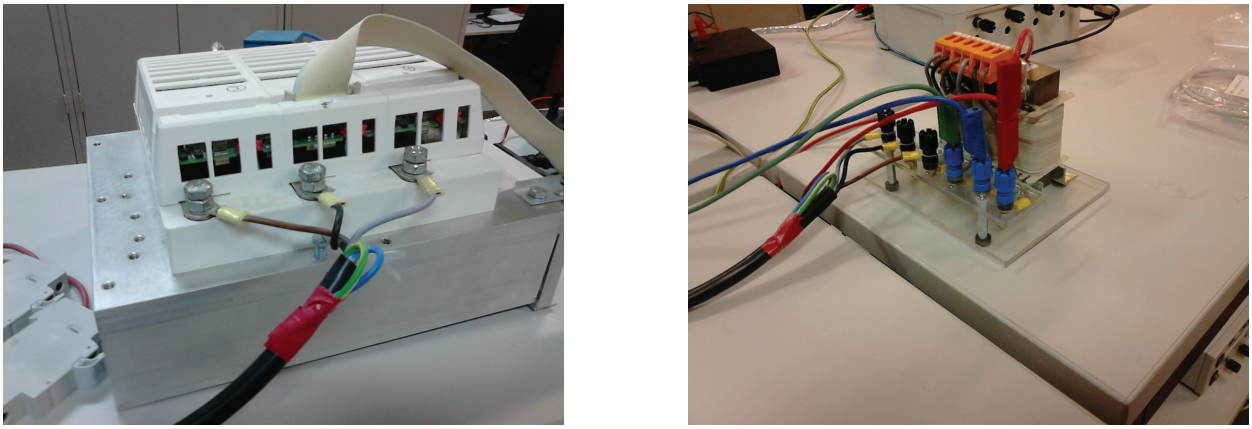

(a) **(b)**

Fig. C.2: Rotor connected elements: (a) inverter bridge; (b) inductive filter

ramps tested.

The measuring and conditioning circuits that convert the signals to be handled by the control platform are also shown (Figure C.6).

The control platform dSPACE DS 1103, in which the measuring circuit is connected to, and that uses the measured signals is also shown Figure C.7.

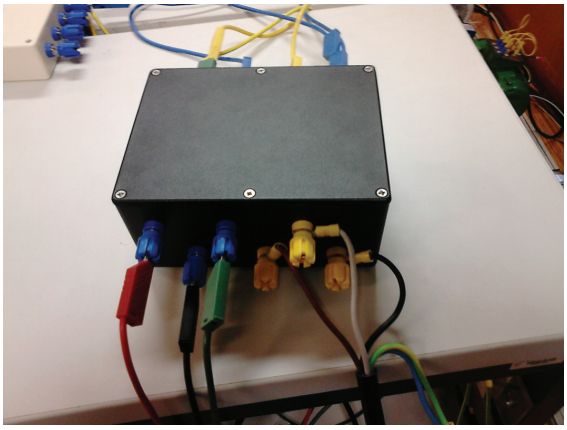

(a)

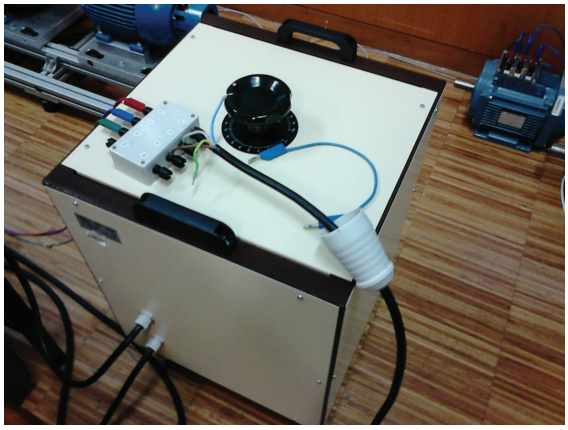

(b)

Fig. C.3: Stator connected elements: (a) diode bridge; (b) autotransformer

(a)

(b)

Fig. C.4: System's dc-link: (a) capacitor-bank; (b) resistive load

The control panel, built in *ControlDesk*, that allows the interaction between the user and the control panel can be seen in Figure C.8 (a). It allows the control, visualization and capture of all variables of interest in the system. Signalled by (b) is the Yokogawa WT3000 Power Spectre Analyser, which was used to calculate the machine's electrical and mechanical power, as well as its efficiency.

B dSPACE Model

The 'Measurements' block makes readings of the current and voltage signals coming from the rotor and stator of the machine. It also measures the dc bus voltage. However all of these

(a) **(b)**

Fig. C.5: VSD used for primary machine control: (a) VSD; (b) VSD's remote controller

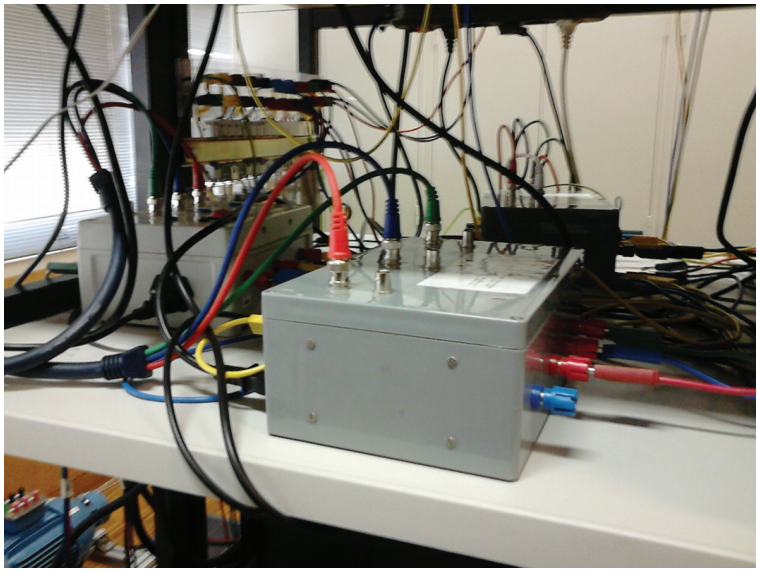

Fig. C.6: Measurement circuit

signals had to be multiplied by appropriate gains, so that the attenuation brought by the sensors and BNC cables could be compensated. It turns the line-to-line voltages applied to the motor in phase voltages to be used by the control system. It also converts the encoder's pulses to a mechanical position signal.

The 'Speed(rpm)' block estimates the rotor speed based on the rotor position signal, given by the encoder. This block works at a rate different from the main program, being twenty times slower. The 'Rate Transition' blocks guarantee the correct synchronization of this block and the main program. The pulses to be applied at the IGBT's gates are generated here, and the automatic protections to stop sending these signals in case of over-current are

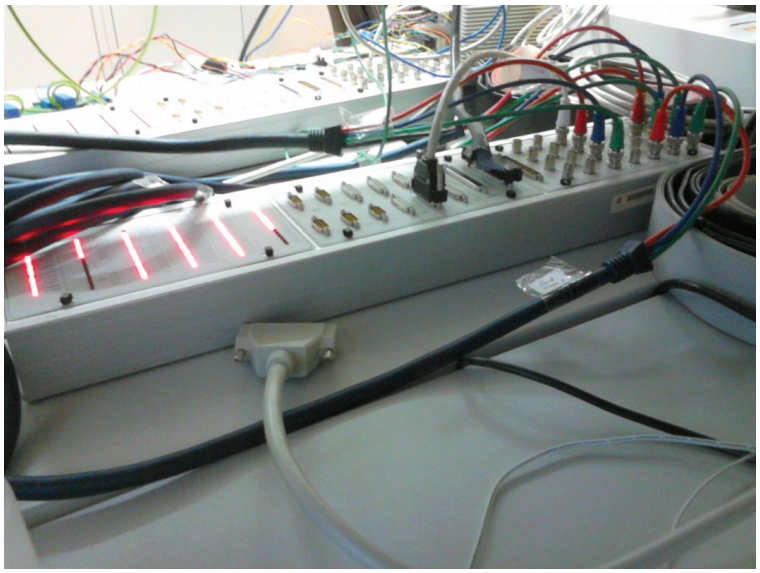

Fig. C.7: Control platform dSPACE 1103

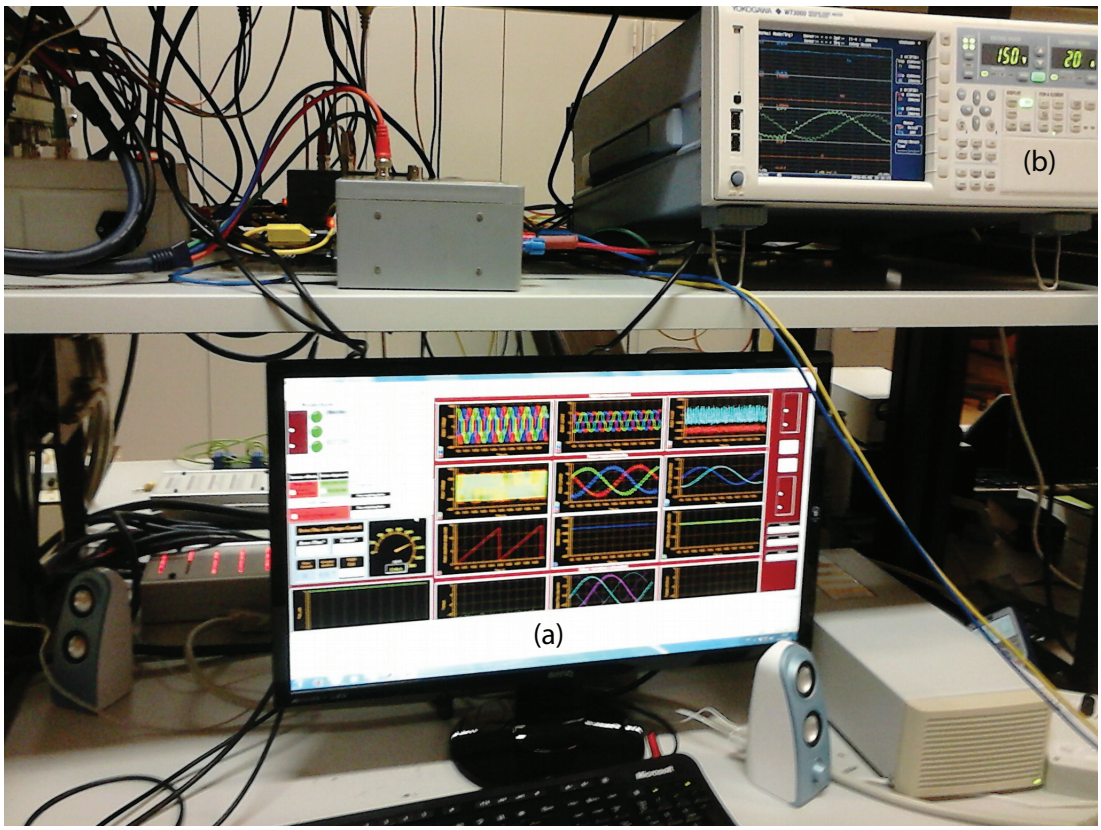

Fig. C.8: Control panel: (a) ControlDesk panel; (b) Yokogawa WT3000

also located here.

The 'Mux' block just gather all the measurements defined in the 2 blocks previously described, so that they can be sent to the 'Predictive Torque and Rotor Flux Control' block.

The 'Predictive Torque and Rotor Flux Control' block is similar to the one used in the

simulation.

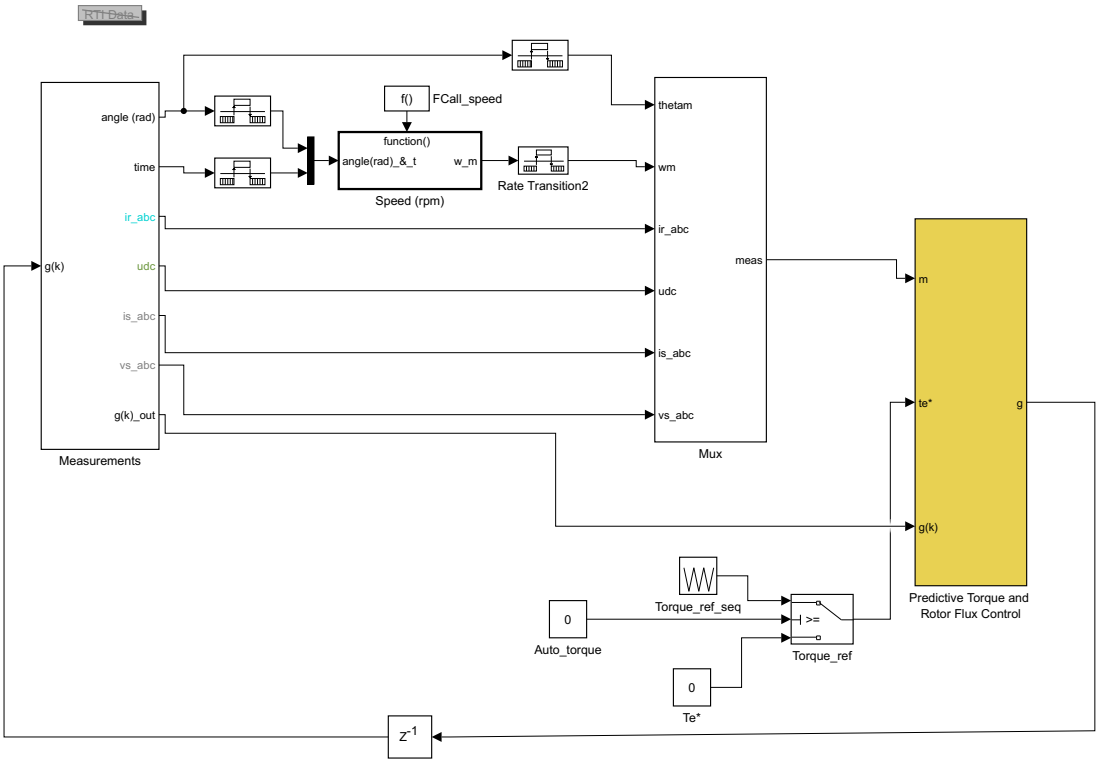

Fig. C.9: Controller model of the MPC control strategy applied to the DFIG